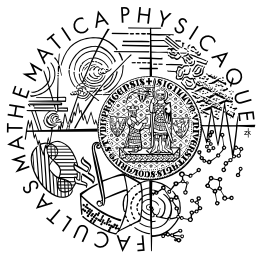

FACULTY
OF MATHEMATICS
AND PHYSICS
Charles University

DOCTORAL THESIS

Cinthia Antunes Corrêa

Structure analysis of some transition metal silicides using X-ray diffraction and dynamical refinement against electron diffraction data

Physics of Materials

Supervisor of the doctoral thesis:	prof. RNDr. Miloš Janeček, CSc.
Study programme:	Physics
Study branch:	Physics of Condensed Matter and Materials Research

Prague 2017

I declare that I carried out this doctoral thesis independently, and only with the cited sources, literature and other professional sources.

I understand that my work relates to the rights and obligations under the Act No. 121/2000 Sb., the Copyright Act, as amended, in particular the fact that the Charles University has the right to conclude a license agreement on the use of this work as a school work pursuant to Section 60 subsection 1 of the Copyright Act.

In ..... date ..... signature of the author

Title: Structure analysis of some transition metal silicides using X-ray diffraction and dynamical refinement against electron diffraction data

Author: Cinthia Antunes Corrêa

Department: Physics of Materials

Supervisor: prof. RNDr. Miloš Janeček, CSc., Department of Physics of Materials

Abstract: This thesis presents the crystal structure analysis of several transition metal silicides. The crystal structures were studied primarily by precession electron diffraction tomography (PEDT) employing the dynamical refinement, a method recently developed for accurate crystal structure refinement of electron diffraction data. The optimal values of the parameters of the method were proposed based on the comparison between the dynamical refinement of PEDT data and a high-quality reference structure. We present the results of the comparison using a Ni_2Si nanowire with the diameter of 15 nm. The average atomic distance between the model obtained by the dynamical refinement on PEDT data and the one by single crystal X-ray diffraction was 0.006 Å. Knowing the accuracy and limitations of the method, the crystal structure of Ni_3Si_2 was redetermined on a nanowire with 35 nm of diameter. The model obtained had an average error in the atomic positions of 0.006 Å. These results show that the accuracy achieved by the dynamical refinement on PEDT data is significantly superior to that of the refinement using the kinematical approximation. With the method validated, the elucidation of the phases of the system $Cu_{3+x}Si$ were pursued. Due to the complex incommensurate modulated structures observed during our PEDT measurements, the dynamical refinement could not be used and a combination of single crystal and powder X-ray diffraction was used. Temperature dependent powder X-ray diffraction revealed a complex Cu-Si phase diagram, where six distinct phases were observed, instead of the three phases reported so far in the $Cu_{3+x}Si$ phase-field. In order of increasing temperature, the phases observed were η''', η'', η', η_3, η_2 and η_1. At least four of the six phases observed are incommensurately modulated. The crystal structures of η''' and η'' were elucidated by single crystal X-ray diffraction, while the phases η_2 and η_1 were indexed on the powder diffraction data. η' is known, and we could index only the main structure of η_3. η''' and η'' are very similar and both have a (3+2)-dimensional incommensurately modulated structure. Given the complexity of their modulation the refinement in the superspace could not be performed, and the models were described in a supercell approximation.

Keywords: Precession electron diffraction tomography, dynamical refinement, nickel and copper silicides, (3+2)D incommensurately modulated structures.

Název práce: Strukturní analýza vybraných silicidů přechodných kovů pomocí rentgenové difrakce a dynamického upřesňování dat z elektronové difrakce

Autor: Cinthia Antunes Corrêa

Katedra: Katedra fyziky materiálů

Vedoucí doktorské práce: prof. RNDr. Miloš Janeček, CSc., Katedra fyziky materiálů

Abstrakt: Tato disertační práce se zabývá krystalovou strukturní analýzou několika silicidů přechodných kovů. Krystalové struktury byly studovány především precesní elektronovou difrakční tomografií (PEDT) za použití metody dynamického upřesňování - nedávno vyvinuté metody, která umožňuje správnější upřesňování krystalové struktury z PEDT dat. Optimální hodnoty parametrů metody byly zvoleny na základě provnání dynamického upřesnění z PEDT dat s kvalitně upřesněhou referenční strukturou. V práci je ukázáno porovnání pro nano-drát Ni_2Si s poloměrem 15 nm. Průměrná odchylka poloh atomů struktury získané dynamickým upřesňováním dat z PEDT od poloh atomů ve struktuře upřesněné z monokrystalových rentgenových dat byla 0,006 Å. S vědomím přesnosti a limitů metody byla správně vyřešena a upřesněna krystalová struktura Ni_3Si_2 na datech získaných z nano-drátu o průměru 35 nm. Získaný model měl průměrnou odchylku atomů 0,006 Å. Tyto výsledky ukazují, že správnost dosažená metodou dynamického přesňování dat z PEDT je jasně vyšší než správnost upřesnění pomocí kinematické aproximace. Po ověření správnosti výsledků dosažených touto metodou bylo přikročeno k analýze fází systému $Cu_{3+x}Si$. Kvůli extrémně komplexním a nesouměřitelným strukturám pozorovaným při měřeních elektronové difrakce nebylo možné použít metodu dynamického upřesňování. Místo ní byla pro strukturní analýzu použita kombinace monokrystalové a práškové rentgenové difrakce. Proměření teplotní závislosti pomocí práškové rentgenové difrakce odhalilo koplexní fázový diagram Cu-Si, ve kterém bylo rozpoznáno šest různých fází v oblasti $Cu_{3+x}Si$ namísto třech doposud publikovaných. V pořadí se vzrůstající teplotou to byly fáze η', η'', η''', η_3, η_2 a η_1. Nejméně čtyři tyto fáze jsou nesouměřitelně modulované. Krystalové struktury η'' a η''' byly vyřešeny pomocí monokrystalové rentgenové difrakce, zatímco fáze η_2 a η_1 byly pouze oindexovány z práškových dat. Fáze η' je již známá a u fáze η_3 bylo možné oindexovat pouze průměrnou strukturu. Fáze η'', η''' jsou si velice blízké a obě mají (3+2)D nesouměřitelně modulovanou strukturu. Kvůli komplexitě jejich modulací nebylo možné tyto struktury v superprostoru upřesnit a proto byly jejich strukturní modely popsány pomocí aproximace superbuňkou.

Klíčová slova: Precesní elektronová difrakční tomografie, dynamické upřesňování, silicidy niklu a mědi, (3+2)D nesouměřitelně modulované struktury.

To my family, Olinda, Hermes and Kathia.

Acknowledgment

I would like to express my gratitude to my supervisor prof. RNDr. Miloš Janeček, CSc., for the valuable and permanent advise. I would like to thank my advisor Dr. rer. nat. Lukáš Palatinus, for constantly teaching and sharing his extensive knowledge and scientific thinking during the whole development of my Ph.D. study. I am grateful to all my colleagues from the Institute of Physics of the Czech Academy of Sciences, specially to Morgane Poupon, Karel Jurek, Mariana Klementová, Petr Brázda, Monika Kučeraková, Margarida Henriques and Karel Vyborný, for creating a good scientific environment. I am also grateful to Thiago Martins Amaral, for the friendship and support for so many years. Last, but not least, I am in huge debt with my family, whose unconditional love, support, patience, and care enabled me to complete my Ph.D. Esse doutorado não existiria sem o apoio de vocês, Olinda e Kathia.

This thesis was financially supported by the Czech Science Foundation, projects 13-25747S and 15-08842J using instruments of the ASTRA lab established within the Operation program Prague Competitiveness, project CZ.2.16/3.1.00/24510; and by the Grant Agency of Charles University in Prague, project 366216/2016.

Contents

Introduction

The most commonly used technique to obtain crystal structure is single crystal X-ray diffraction (SCXRD), which requires crystals larger than $5 \times 5 \times 5\,\mu m^3$. For cases where the sample is composed of crystals from hundreds of nanometers up to $5\,\mu m$, powder X-ray diffraction (PXRD) is the method of choice. If the sample is polyphasic, or if reflection overlap occurs either due to a large unit cell or the presence of pseudosymmetry, the interpretation and structure solution from PXRD data may be very difficult, if not impossible. If single crystals cannot be obtained in suitable size neither for SCXRD nor for PXRD, or if the properties of the nanocrystal differs from the bulk sample, it is crucial to obtain an accurate crystal structure of nanocrystals. In this sense, electron diffraction (ED) is of great importance because it can be used in the structure analysis of nanocrystals as small as few tens of nanometers.

Electrons interact strongly with matter, what allows one to observe much smaller crystals, but this same stronger interaction generates multiple scatterings. Multiple scatterings hamper the data analysis, and therefore the crystal structure obtained from electron diffraction data was not considered to be sufficiently accurate. In 1994 Vicent and Midgley developed the precession electron diffraction (PED), which results in intensities with less influence of multiple scatterings. In spite of PED allowing to collect intensities with kinematical-like character, multiple scattering is still observed in PED data. There were several attempts to take the multiple scatterings into account for ED data. The dynamical theory of diffraction, which takes into account multiple scatterings, was used during the development of software for the refinement of crystal structure parameters. What all these software have in common is that they use oriented patterns for the structure analysis. Oriented patterns do not give detailed three-dimensional information of the reciprocal space of the sample, and the lack of information might hamper the structure solution and refinement or even preclude it.

In 2007 Kolb *et al.* developed the electron diffraction tomography (EDT), which gives a more detailed sampling of the reciprocal space of a nanocrystal. PED and EDT (PEDT) were combined in 2009 by Mugnaioli *et al.*, thereby providing complete data sets with kinematical-like intensities. Approaches using this combination have been used since then and several crystal structures were determined, but still with high figures of merit. The only way to achieve accurate crystal structure parameters of nanocrystals is to use the dynamical theory of diffraction for a complete electron diffraction data. A routine using the dynamical theory of diffraction for electron diffraction data acquired either with or without precession was developed in our laboratory. This routine was named dynamical refinement and has been available since 2015 implemented in the crystallographic software

Jana2006.

The first objective of this thesis was to verify the behavior of the parameters used within the dynamical refinement in order to validate the method. The validation was done by comparing the results of known crystal structures obtained by the dynamical refinement with the ones obtained by the standard SCXRD. The second objective was to use the dynamical refinement for the determination of an unknown crystal structure.

Samples used for the dynamical refinement were chosen within transition metal silicides, given their potential use in nanotechnology. Especially silicide nanowires (NWs) are of great interest for diverse application in nanoscale electronics, photonic, sensor and photovoltaic devices. Within the transition metal silicides, nickel and copper silicides stand as a suitable option for nanoscale electronics due to their enhanced electrical properties.

One of the samples used for the verification of the behavior of the parameters used in the dynamical refinement was a nanowire of Ni_2Si with the diameter of 15 nm. Knowing the accuracy and the limitations of the dynamical refinement based on the tests, the crystal structure of Ni_3Si_2 was redetermined.

The unknown structure was pursued for the copper silicide $Cu_{3+x}Si$, which is known to go through phase transitions with increasing temperature. In order to elucidate the crystal structures of the phases and to better understand the structural modifications during the heating, temperature dependent precession electron diffraction data was acquired (TD-PEDT). Two incommensurately modulated structures were found. Since the modulation observed is very complex and it was not possible to refine the structure using the superspace approach for TD-PEDT, a hybrid approach was used, combing single crystal and powder X-ray diffraction.

This thesis is divided into four chapters. The first one gives the literature review and background on the dynamical theory of diffraction, which is the base for the dynamical refinement. The second chapter discusses two particular topics used in electron diffraction and in the dynamical refinement: the crystal potential and geometric approximation of crystal shapes. The experimental methodology used for the PEDT data and for the dynamical refinement are presented, followed by the tests on the dynamical refinement performed for the known structure of Ni_2Si and the redetermination of the crystal structure of Ni_3Si_2. Chapter three presents the experimental procedure and results on the two incommensurately modulated structures of the silicide $Cu_{3+x}Si$ and the newly observed phase transitions of this alloy. The last chapter concludes the work, summarizes the main results and presents future work.

1. Literature overview and theoretical background

1.1 The first uses of electron diffraction

The discovery of the X-ray diffraction by crystals in 1912, proposed by Laue and performed with Friedrich and Knipping, proved the wave-like nature of rays, as well as the periodic character of crystals. This discovery was the basis for the actual X-ray crystallography. In 1924 de Broglie proposed the wave-like nature of electrons, what allowed for the possibility of even shorter wavelengths compared to X-rays. This possibility was proved in 1927 with the first electron diffraction (ED) experiment, which was achieved at the laboratory of Davisson [1] and Thomson [2], resulting in their Nobel Prize in 1937. In 1931, Ruska and Knoll succeeded to develop the first electron microscope [3]. Further effort on the development of the electron diffraction technique and on electron diffraction cameras lead Pinsker and Vainshtein to achieve the first crystal structure solved from electron diffraction data in 1949 [4, p. 305]. Since then several crystal structures were elucidated using electron diffraction [5, 6, 7], but the method used to obtain the calculated intensities was based on the kinematical approximation.

The kinematical approximation is based on the assumption that the incident electron beam interacts weakly with the crystal potential, there is only a single scattering and the magnitude of the scattered wave is weak compared to the incident one. This single scattering would result in each diffraction being independent of the other ones (Fig. 1.1(a)).

In the kinematical approximation, the diffracted intensity related to a scattering vector $\mathbf{g}$ is proportional to the square of the amplitude of its structure factor ($I_{\mathbf{g}} \propto |F_{\mathbf{g}}|^2$). However, in 1914 Darwin noticed that this approximation violates the conservation of energy, since it considers only the wave diffracted by the first crystal plane [8, p. 68]. Indeed, if the incident wave satisfies the Bragg condition on the first crystal plane, it is partially reflected and transmitted at each of the next lattice planes as well, and the transmitted component becomes a primary wave for generating a new set of reflected and transmitted waves when it goes through the next crystal planes (Fig. 1.1(b)). Hence, multiple scatterings hold even for very thin crystals and how many times the interaction can occur depend on the sample thickness, on the crystallinity of the sample, on the orientation of the crystal, and on the strength of the scattering [9, 10].

In electron diffraction the electrostatic potential as seen by the electron beam includes the nuclear and the electronic contributions and thus electrons from the

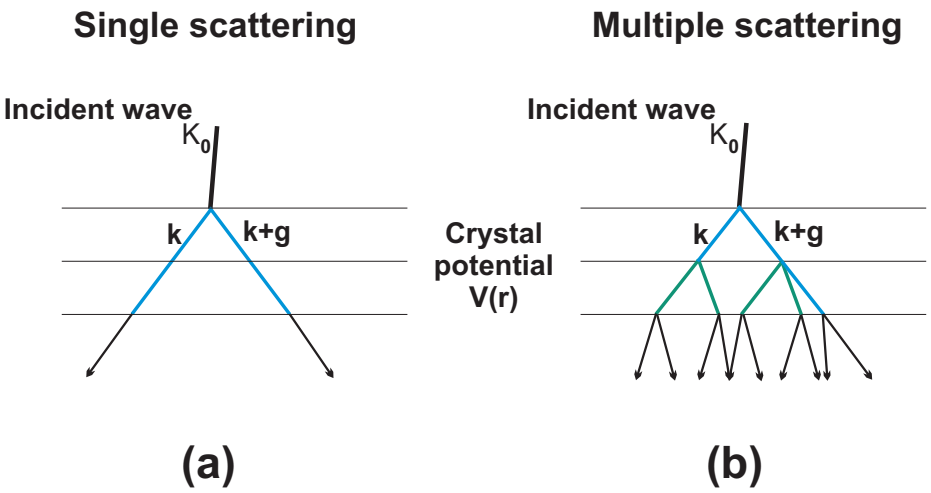

Figure 1.1: (a) Kinematical approximation: Single scattering of the incident beam when crossing the crystal potential. (b) Dynamical scattering: The incident beam is diffracted, becoming a primary beam which is scattered multiple times while crossing the crystal potential.

incident beam are scattered with the intensity of about 10^6 times stronger for high energy electron diffraction (HEED) (voltage of the source about 20 keV or higher) than for X-rays. This stronger interaction allows one to obtain crystal information from samples with a few cubic-nanometers in size, but also generates multiple scatterings, or dynamical scatterings. Therefore, the validity of the kinematical approximation is limited for electron diffraction. In spite of providing a reliable qualitative interpretation of the diffraction patterns of the crystal, the resulting refined structure parameters are not accurate, and the figures of merit are known to be high [11].

One of the approaches used for minimizing the effects of the dynamical scattering is to integrate several orientations of the incident beam for each crystal position using precession electron diffraction (PED) [12].

1.2 Precession electron diffraction (PED)

In 1994, Vicent and Midgley developed the precession electron diffraction [12], which consists in deflecting the incident beam away from the optical axis with a precession angle φ of a few degrees (usually less than 3°). The incident beam precesses around the optical axis and makes a cone surface with vertex on the surface of the sample. The coils after the specimen descan the beam, so that the reflections are spots, as can be seen in Fig. 1.2(a). The result is a diffraction

pattern that has intensities integrated from diffraction conditions over a range of angles α: $I_g^{exp} \propto \int_0^{2\pi} I_g(\alpha) d\alpha$ [12, 13]. Since these intensities are integrated for slightly different orientations, they are less sensitive to small crystal imperfections and a lower number of multiple scattering occurs, resulting in intensities with a pseudo-kinematical character. For data without PED only a cross section of each reflection with the Ewald sphere is considered. Fig. 1.2(b) shows the range of angles α used for the integration of the reflection, and the Ewald sphere cutting the reflection when the precession is not used.

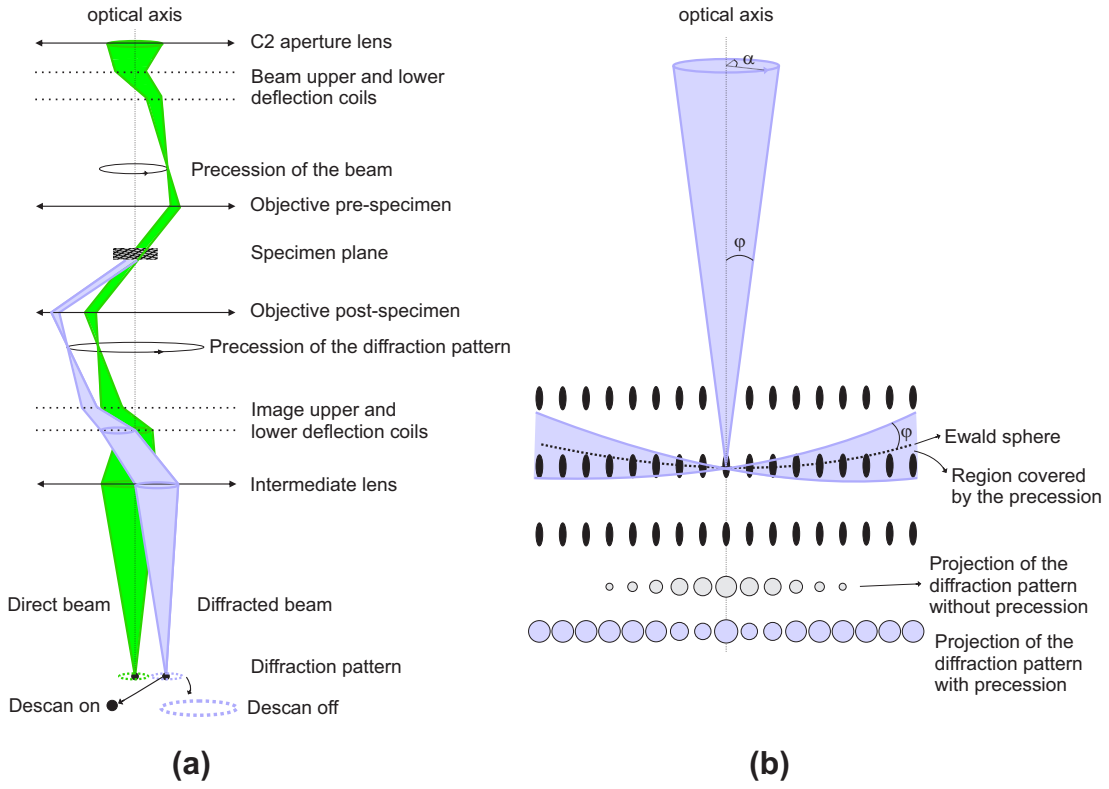

Figure 1.2: Scheme of the precession of the beam. (a) The direct beam and one diffracted beam are represented. The direct beam is deflected by the beam coils above the specimen, forming a cone surface with vertex at the sample surface. The coils below the specimen descan the beam, resulting in diffracted spots. (b) The Ewald sphere sweeps the rods of reflections because of the precession, covering an angle α during the precession circuit. The projection of the diffraction pattern is represented with and without precession.

PED gives kinematical-like intensities, but dynamical scattering is unavoidable. The solution to the dynamical scattering is to use the dynamical theory of diffraction during the calculation of the diffracted intensities of ED.

1.3 Evolution of the dynamical refinement

The dynamical theory has been known for decades (see section 1.4). In spite of that, its use only took place in the nineties, when the dynamical theory of diffraction was used for the first time to refine structure parameters using oriented patterns of convergent-beam electron diffraction (CBED) [14]. In 1998 Jansen *et al.* [15] developed the Multislice Least-Squares (MSLS), which uses a combination of the multislice method with a least-squares algorithm. The multislice method considers the crystal as a stack of slices of equal and very small thickness to calculate dynamical scatterings. The n beams dynamical theory was used for the refinement of crystal structure parameters using oriented patterns of CBED in the software called Many-Beam Dynamical Calculations and Least-squares Fitting (MBFIT) in 1999[16]. The next software developed using the dynamical theory of diffraction was ASTRA [17], which was developed by Dudka *et al.* and uses two approaches: The first one performs structure parameters refinement using the two-beam approximation of the dynamical theory of diffraction and considers the overlap of reflections from data collected on polycrystalline films. In the second approach, the refinement of crystal structure using electron diffraction data on single crystals uses the many beams dynamical theory of diffraction in the Bloch wave formalism. In 2011 the software eSlice was developed and implemented in eMap [18]. eSlice allows one to refine crystal structures from oriented patterns and considers the multislice approach to calculate dynamical scattering, similarly to MSLS, developed by Jansen *et al.* [15].

This late use of the dynamical theory of diffraction might be due to the high demand for computational power to perform the calculations, since the calculation time was an issue mentioned by most of these authors [14, 16, 17, 18, 19].

These approaches have in common the fact that they use oriented diffraction patterns. The limitation of oriented patterns is the lack of a complete data set, since only special orientations of the crystal are used during the data acquisition. The problem of incomplete data set can be solved either by three-dimensional electron diffraction tomography (EDT) [20, 21] or by rotation electron diffraction (RED) [22, 23]. In the three-dimensional EDT the crystal is rotated around an arbitrary axis in small steps and diffraction patterns are collected at each step for the same crystal. Since the angles between the diffraction patterns are known, the reciprocal space can be reconstructed giving additional information about the electron diffraction [20, 21, 24]. In the rotation electron diffraction the tilt of the goniometer is combined with the beam tilt and diffraction patterns are collected at each position. These patterns are processed, also giving three-dimensional information of the reciprocal space [23].

PED and EDT (PEDT) were combined in 2009 by Mugnaioli *et al.*, what enabled one to obtain complete data sets and less multiple scatterings. This com-

bination has been used to determine several crystal structures [25, 26, 27], but still with high figures of merit and unreliable accuracy of the structure parameters [11] because the kinematical approximation was still used.

Although PEDT allows solving structures *ab initio* and the dynamical theory of diffraction has been known for decades, the lack of a general routine to analyze the structures using the n beams dynamical theory for a complete 3-dimensional data set prevented the wide use of the technique for some time.

The first step for the routine using the n beams dynamical theory of diffraction to refine a complete ED data set was performed in our laboratory by Palatinus *et al.* in 2013 [27], when it was shown that using the dynamical diffraction theory to oriented patterns obtained by PEDT gives results with better figures of merit and more accurate structure parameters than the ones obtained using the kinematical approximation. The complete dynamical refinement, using n beams on a 3-dimensional data set collected by EDT without especial orientation (called dynamical refinement hereinafter), followed in 2015 by Palatinus *et al.* [28]. The dynamical refinement can be applied to data collected either with or without precession, and it is implemented in the crystallographic software Jana2006 [29, 30]. Since then the dynamical refinement became freely available. Palatinus *et al.* [28] describes the implementation of the dynamical theory of diffraction for the full-matrix least-squares refinement, and the parameters of the method in detail. An overview of the basic calculations used during the dynamical refinement is given in the following sections.

1.4 The dynamical theory of diffraction

The dynamical theory of diffraction using the Bloch wave approach is well covered in several sources [10, 31, 32, 33, 34] and an overview will be given here.

In electron diffraction, the interaction of the incident electron beam with the crystal is given by the interaction of a plane wave with the time-independent, periodic potential field of the atoms within the crystal. The amplitudes of the diffracted beams are obtained from the solution of the Schrödinger equation, which gives the wave function of an electron propagating in a periodic medium [35, 36]:

$$\frac{-h^2}{8\pi^2 m}\nabla^2\psi(\mathbf{r}) + eV(\mathbf{r})\psi(\mathbf{r}) = eE\psi(\mathbf{r}), \tag{1.1}$$

where h is the Planck constant, m is the electron mass, ψ is the wave function, e is the electronic charge, E is the accelerating potential producing the incident beam, and $V(\mathbf{r})$ is the electrostatic potential of the crystal. $V(\mathbf{r})$ is maximum at the atomic positions $\mathbf{r}$.

It was shown by Fujiwara [37] and Ferwerda *et al.* [38] that the solution of the Dirac equation, considering spins and using high-energy approximation, gives the same equation as the non-relativistic Schrödinger equation (Eq. 1.1) using the relativistic electron mass and wavelength. Hence, the time-independent non-relativistic solution of the Schrödinger equation can be used to describe the elastic scattering of the electrons by the crystal [39, 33], given that the motion of the electron is constant and that the relativistic electron mass and wavelength are used for HEED. The solution of the Schrödinger equation for the periodic potential is given by a linear combination of degenerate Bloch waves:

$$\psi(\mathbf{r}) = \sum_{\mathbf{j=1}}^{n} \epsilon^j \psi^j(\mathbf{r}). \tag{1.2}$$

Here ϵ^j are the Bloch excitation coefficients. The Bloch wave in the degenerate state is given by

$$\psi^j(\mathbf{r}) = \sum_{\mathbf{g}} C^j_{\mathbf{g}} \exp\left(2\pi i(\mathbf{k}^j + \mathbf{g}).\mathbf{r}\right), \tag{1.3}$$

where $\mathbf{k}^j$ is the wave vector excited in the crystal, $\mathbf{g}$ is the reciprocal lattice vector, and $C^j_{\mathbf{g}}$ are the wave amplitudes. In order to find $C^j_{\mathbf{g}}$ it is necessary to determine which wave vectors $\mathbf{k}^j$ will be excited in a crystal for given crystal orientation. The total number of possible excited waves will depend on the total energy of the electron beam, while the boundary conditions such as crystal orientation and crystal shape determine the Bloch waves which can be excited and the Bloch wave excitation coefficients ϵ^j. Hence, ϵ^j are different for equivalent reflecting positions of the crystal, yielding different intensities for symmetrically equivalent reflections.

The electrostatic potential $V(\mathbf{r})$ of the crystal is a periodic function with periodicity depending on the atomic positions. Hence, it can be expanded in Fourier series

$$V(\mathbf{r}) = \sum_{\mathbf{g}} V_{\mathbf{g}} \exp(-2\pi i \mathbf{g}.\mathbf{r}), \tag{1.4}$$

where $V_{\mathbf{g}}$ is the Fourier coefficient of the crystal potential given by the Fourier transform of the lattice potential

$$V_{\mathbf{g}} = \frac{1}{\Omega} \int V(\mathbf{r}) \exp(-2\pi i \mathbf{g}.\mathbf{r}) d\mathbf{r}, \tag{1.5}$$

given in units of volts. Ω is the unit cell volume. For an infinite crystal this Fourier transform consists of discrete peaks positioned exactly at the reciprocal

lattice nodes. However, for a finite crystal the diffracted intensities have a relrod shape and the Ewald sphere will be a plane cutting the intensity relrods. The distance from the reciprocal lattice point to the Ewald sphere along the normal of the crystal surface is called excitation error $S_{\mathbf{g}}$.

The Fourier transform of the potential gives the atomic scattering factors, which expresses how much a single atom scatters an incident electron, or the amplitude probability of the incident electron with wave vector $\mathbf{K}_0$ to be scattered in the direction $\mathbf{K}'$ by the interaction with an isolated atom. The atomic scattering factor is

$$f^e(\mathbf{g}) = \int V(\mathbf{r}) \exp(2\pi i \mathbf{g}.\mathbf{r}) d\mathbf{r} \ . \tag{1.6}$$

It is analogous to the atomic scattering factor of X-rays, which is given in function of the atomic electron density. The unit of the atomic scattering factor in electron diffraction was derived from nuclear physics and it is given in V·Å^3, while the atomic scattering factors of X-ray are given in units of electrons. It is important to note that f^e does not depend on any experimental parameter, since $\mathbf{g}$ depends on the Bragg condition which only depends on the interatomic distances within the crystal structure. The summation of the atomic scattering factors gives the structure factor $F_{\mathbf{g}}$ ($F_{\mathbf{g}} \propto V_{\mathbf{g}}$) for an unit cell.

Now, using the Bloch wave approach (Eq. 1.3) developed by H. Bethe [31] and the potential expanded in Fourier series (Eq. 1.4) in the Schrödinger equation (Eq. 1.1), the dispersion for HEED is obtained:

$$[\mathbf{K}^2 - (\mathbf{k}^j + \mathbf{g})^2] C^j_{\mathbf{g}} + \sum_{\mathbf{h}} \mathbf{U}_{\mathbf{g}-\mathbf{h}} C^j_{\mathbf{h}} = 0 \tag{1.7}$$

where $\mathrm{U}_{\mathbf{g}}$ is the dynamical structure factor for a given reciprocal lattice vector $\mathbf{g}$ and the relation $U_{\mathbf{g}} = \frac{2me}{h^2} V_{\mathbf{g}}$ was used. $\mathrm{U}_{\mathbf{g}}$ is a complex number and it can be shown that the complex part describes the effect of inelastic scattering [40, p. 327]. Here we will consider only the elastic scattering, thus the real term of the potential.

Restrictions on the total energy will determine the vectors $\mathbf{k}^j$ which can be excited in the crystal and their associated amplitudes, according to the energy relation $E(K) = \frac{K^2 h^2}{2me}$. $\mathbf{K}$ is the wave vector of the incident beam corrected for the crystal inner potential $K^2 = (K_0^2 + U_0)$. Since the potential from the beam is some orders of magnitude higher than the lattice potential ($\frac{-h^2}{2me} >> U_0$), the HEED approximation is valid, which means that the back scattered waves can be neglected.

Following from Eq. 1.7 if n beams are considered to be excited [32], the set of n linear homogeneous equations can be conveniently written as a $n \times n$ square matrix. Note that the kinematical approximation is achieved by using a single scattering in

the dynamical approach. Neglecting back-scattered waves, the square matrix can be transformed in an eigenvalue eigenvector equation which can be diagonalized, arriving at the structure matrix $\mathbf{A}$ with components a_{ij}:

$$a_{ij} = \begin{cases} \frac{U_{\mathbf{g}_i - \mathbf{g}_j}}{(1+g_{n,i}/K_n)^{1/2}(1+g_{n,j}/K_n)^{1/2}}, & i,j = 1,n; i \neq j \\ \\ \frac{|\mathbf{K}|^2 - |\mathbf{K}+\mathbf{g}_i|^2}{(1+g_{n,i}/K_n)^{1/2}}, & i = 1,n; i = j, \end{cases} \tag{1.8}$$

where g_n and K_n are the projections of the vectors $\mathbf{g}$ and $\mathbf{K}$ along the normal to the crystal surface [10, p. 38].

Defining a diagonal matrix $\mathbf{M}$ as

$$m_{ii} = \frac{1}{(1 + g_{n,i}/K_n)^{1/2}}, \tag{1.9}$$

the incident waves are related to the scattered ones through the scattering matrix $\mathbf{S}$

$$\mathbf{S} = \mathbf{M} \exp\left(\frac{2\pi i t}{2K_n}\mathbf{A}\right)\mathbf{M}^{-1}, \tag{1.10}$$

which is given by the exponential of the structure matrix $\mathbf{A}$, and the thickness t of the crystal slab. If absorption is neglected and there is only one incident plane wave $\mathbf{K}$, the diffracted intensities are given by the square of the amplitude of one column of the scattering matrix

$$I_{\mathbf{g}i} = |\psi|^2 = |S_{i1}|^2 \tag{1.11}$$

As seen from Eq. 1.8, the diffracted intensities (Eq. 1.11) are affected by the crystal orientation through the components of the structure matrix a_{ij} (Eq. 1.8) and by crystal thickness t inside the scattering matrix $\mathbf{S}$ (Eq. 1.10). Therefore, assuming the crystal to be a slab is a limitation for the method. On the other hand, the positions of the reflections in the ED pattern are not substantially altered by a small modification on the orientation of the crystal.

2. The dynamical refinement implemented in Jana2006

2.1 Crystal potential

During the structure analysis, the difference of electron density is observed on the Fourier maps for X-ray diffraction. With the intention to define an equivalent to the difference electron density of X-ray for electron diffraction, an analogous to difference potential was pursued.

The electrostatic potential of an atom scatters the electron beam during electron diffraction (ED) similarly to the scattering of X-ray by the electron density during X-ray diffraction. The Fourier expansion of the electrostatic potential (Eq. 1.4) is

$$V(\mathbf{r}) = \sum_{\mathbf{g}} V_{\mathbf{g}}(\mathbf{g}) \exp(-2\pi i \mathbf{g}.\mathbf{r}) = \sum_{\mathbf{g}} V_{\mathbf{g}}(\mathbf{s}) \exp(-4\pi i \mathbf{s}.\mathbf{r}) \ ,$$

where $2\mathbf{s} = \mathbf{K_0'} - \mathbf{K_0} = \mathbf{g}$ is the difference between the incident and the scattered wave vectors. The Fourier coefficient $V_{\mathbf{g}}$ of the crystal potential can be written as a function of the summed electron scattering factors $f^B(\mathbf{s})$ for the whole unit cell volume Ω using the structure factor $F^B = \sum_i f^B(\mathbf{s}) \exp(4\pi \mathbf{s}.\mathbf{r}_i)$

$$V_{\mathbf{g}}(\mathbf{s}) = \frac{h^2}{2\pi m|e|} \frac{F^B}{\Omega} \ , \tag{2.1}$$

given in volts in the International System of Units (SI) or in statvolts, using the Gaussian units (G)

$$V_{\mathbf{g}}(\mathbf{s}) = \frac{h^2}{8\pi^2 \epsilon_0 m|e|} \frac{F^B}{\Omega} \ . \tag{2.2}$$

However, this equation is given as $V_{\mathbf{g}}(\mathbf{s}) = \dfrac{h^2}{8\pi\epsilon_0 m|e|} \dfrac{F^B}{\Omega}$ in several books on Crystallography [10, 41, 42, 36].

In order to verify $V_{\mathbf{g}}$, we start from the atomic scattering, which is an atomic property independent on the scattering process or the theoretical approximation used for the description. As given by Eq. 1.6 for electrons and using $2\mathbf{s} = \mathbf{g}$, the atomic scattering factor is defined as

$$f^e(\mathbf{s}) = \int V(\mathbf{r}) \exp(4\pi i \mathbf{s}.\mathbf{r}) d\mathbf{r} \ ,$$

given in units of V·Å^3. Integrating $f^e(\mathbf{s})$ by parts and using the Poisson's relation $\nabla^2 V(\mathbf{r}) = \frac{-|e|}{\epsilon_0}(\rho_n - \rho_e)$, where ρ_n is the charge density of the nuclei and ρ_e is the charge density of electrons, the relation between the electron scattering factor and the X-ray scattering is given by

$$f^e(\mathbf{s}) = -\frac{1}{16\pi^2 s^2}\int V(\mathbf{r})\nabla^2 \exp(4\pi i \mathbf{s}\cdot\mathbf{r})d\mathbf{r} = \frac{|e|}{16\pi^2\epsilon_0 s^2}[Z - f^X(\mathbf{s})]\ . \tag{2.3}$$

According to the Mott-Bethe relationship

$$f^B = \frac{me^2}{8\pi\epsilon_0 h^2}\frac{Z - f^X(\mathbf{s})}{s^2}.$$

Substituting f^e (Eq. 2.3) in f^B

$$f^B = \frac{2\pi m|e|}{h^2}f^e = \frac{\sigma}{\lambda}f^e,$$

where σ is the interaction constant and λ is the electron wavelength. The atomic scattering factor f^B for electrons is the quantity measured and it is given in units of Å, with values given in the International Table volume C [36]. Ångströn might be a counter-intuitive unit, but the reason why this is used is given by historical accident as the term appearing in the first order of the Born approximation, which was derived from the scattering theory and considers the atomic scattering factors f^B as a function of the scattering vector (given in units of Å) [35].

Now, $V_\mathbf{g}$ is given according to Eq. 2.1

$$V_\mathbf{g}(\mathbf{s}) = \frac{h^2}{2\pi m|e|}\frac{F^B}{\Omega} = \frac{1}{\Omega}\frac{\lambda}{\sigma}F^B,$$

and the structure factor is

$$F^B = \frac{V_\mathbf{g}(\mathbf{s}).\Omega 2\pi m|e|}{h^2}\ , \tag{2.4}$$

given in Å.

The difference between the amplitude of the experimental structure factor and the one from the model gives the difference Fourier map for electron diffraction

$$\Delta|F^B| = |F^B_{exp} - |F^B_{model}||\ . \tag{2.5}$$

A more intuitive quantity measured during ED might be the potential in units of electrons per Ångström instead of volts, which would gives an idea of a potential

density. This might be obtained by transforming the potential $V(\mathbf{r})$ from the Gaussian (G) to the International System of Units (SI). Knowing that

$$V(\mathbf{r}) = \int \frac{\rho(\mathbf{r}')}{|\mathbf{r} - \mathbf{r}'|} d^3\mathbf{r}' \text{ (G)} \tag{2.6}$$

in Gaussian units and

$$V(\mathbf{r}) = \frac{1}{4\pi\epsilon_0} \int \frac{\rho(\mathbf{r}')}{|\mathbf{r} - \mathbf{r}'|} d^3\mathbf{r}' \text{ (SI)}, \tag{2.7}$$

then the potential is given as

$$V(\mathbf{r})[\frac{e}{\text{Å}}] = V[\text{V}] \times \frac{4\pi\epsilon_0}{e} = V[\text{V}] \times 0.06942 \ , \tag{2.8}$$

in units of electron per Ångström and a more intuitive result is obtained.

2.2 Calculated intensities

The method used in Jana2006 to calculate the intensities considering the dynamical interaction is the Bloch-wave method, explained in detail in [28] and in section 1.4.

The calculated intensities are commonly based on the assumption that the crystal is an infinite uniform slab with planar parallel surfaces. In this case, it was shown in section 1.4 that the diffracted wave function would depend on the thickness and on the orientation of the crystal. However, real crystals very often are not perfect slabs and the diffracted intensities are influenced by the shape of the crystal. As a consequence equivalent diffracted beams might have different intensities caused by multiple interactions taking place at different positions at the non-planar crystal. For instance, Metherell [33, p. 487] showed that for a wedge shaped crystal, thickness fringes in the diffracted pattern appear due to the interference between non-parallel direct and diffracted waves. Since it would be difficult to calculate the diffracted intensities for a crystal with irregular shape, one possible approximation is to consider the crystal as a group of parallel slabs or columns of different thickness. This approximation is valid if the crystal is not very irregular. In this case the intensities can be calculated using the probability density distribution of the thickness across the crystal as

$$I_{\mathbf{g}} = \int_{t_{min}}^{t_{max}} I_{\mathbf{g}}(t) f(t) dt. \tag{2.9}$$

Geometric approximations were used to analytically obtain the thickness probability density [28], which can be used during the calculation of the intensities used in the dynamical refinement.

2.2.1 Crystal shapes

Since the shape of the crystal measured has an influence on the diffracted intensities, the aim here was to take it into account during the dynamical refinement through the use of geometric approximations of different crystal shapes.

The cumulative distribution function (CDF) was calculated for four fundamental crystal shapes, which are available to be used during the dynamical refinement: wedge, cylinder, ribbon with the intersection like a lens, and a convex lens.

Let $F(t)$ be the CDF corresponding to the thickness probability distribution function $f(t)$. We then define the following quantities:

- t is the thickness along the beam direction, assuming the beam vertically incident on the crystal;
- D and t_m are the maximum lateral length and thickness of the crystal, respectively;
- $f = \frac{t_m}{D}$ is the flatness parameter;
- $\tau = \frac{t}{t_m}$ is the reduced thickness of the crystal;
- x is the lateral distance from the origin of the coordinate system.

Wedge

The length and the thickness of a wedge are linearly related by $t = \frac{xt_m}{D}$. The probability $F(t)$ of the incident beam hitting a thickness smaller then t is the position x corresponding to t divided by the maximum length D

$$F(t) = \frac{x}{D} = \frac{t}{t_m}. \tag{2.10}$$

Hence,

$$F(\tau) = \tau, \tag{2.11}$$

represented by the shaded area on Fig. 2.1(a).

Cylinder

The cylinder model represents either a needle-shaped crystal or a nanowire. Considering the cylinder lying perpendicular to the beam, with the beam parallel to the vertical axis of Fig. 2.1(b), $F(t)$ will be that of a circle. The thickness depends on the coordinate x, where the origin was chosen to be in the center of the

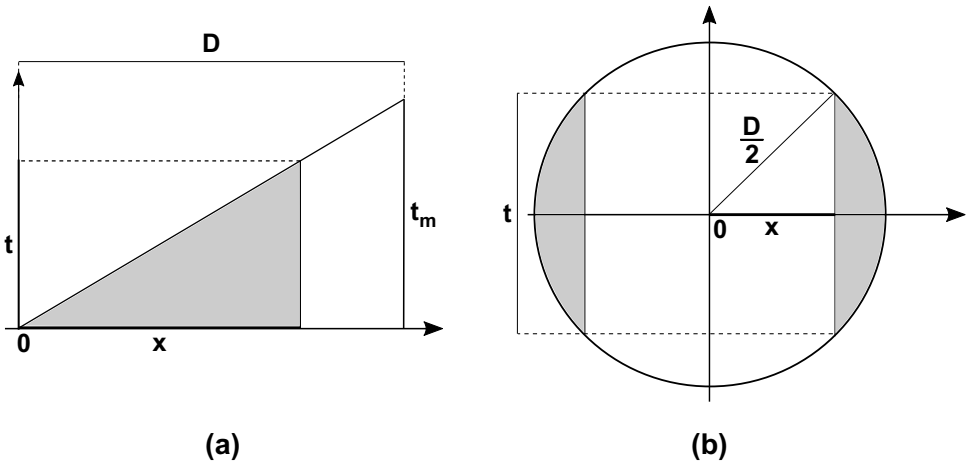

Figure 2.1: Sketch of (a) a wedge-shaped crystal, and (b) a cylindrical crystal. Shaded area highlights the part of the crystal thinner than t.

circumference (Fig. 2.1 (b)), with maximum thickness equal to the diameter D. $F(t)$ of a thickness t is the length $(D-2x)$ (the length in the horizontal axis from the shaded area on Fig. 2.1(b)) divided by the total length D of the crystal

$$F(x) = \frac{D-2x}{D} = 1 - \frac{2x}{D}, \tag{2.12}$$

where $2x = 2\sqrt{\left(\frac{D}{2}\right)^2 - \left(\frac{t}{2}\right)^2}$.

Hence, $F(t) = 1 - \frac{2\sqrt{(\frac{D}{2})^2-(\frac{t}{2})^2}}{D} = 1 - \sqrt{1-(\frac{t}{t_m})^2}$ or, in function of the reduced thickness,

$$F(\tau) = 1 - \sqrt{1-\tau^2}. \tag{2.13}$$

Ribbon with lens-shaped cross-section

A two-dimensional lens can be represented as the intersection of two disks of equal radius displaced from each other in the vertical direction $\frac{t_m}{2}$ (Fig. 2.2(a)), where the thickness t is defined in the vertical direction. Since the difference between the ribbon and the cylinder is that $t_m < \frac{D}{2}$ for the ribbon, $F(x)$ is the same as for the cylinder $F(x) = 1 - \frac{2x}{D}$, but the position in function of the thickness is given by

$$x = \sqrt{\left(\frac{\left(\frac{D}{2}\right)^2 + \left(\frac{t_m}{2}\right)^2}{t_m}\right)^2 - \left(\frac{t}{2} + \frac{\left(\frac{D}{2}\right)^2 - \left(\frac{t_m}{2}\right)^2}{t_m}\right)^2}. \tag{2.14}$$

Using the reduced thickness and the flatness parameter to simplify,

$$x = \frac{D}{2}\sqrt{1 - \tau^2 f^2 - \tau(1 - f^2)}, \tag{2.15}$$

the cumulative distribution function is

$$F(\tau) = 1 - \sqrt{1 - \tau^2 f^2 - \tau(1 - f^2)}. \tag{2.16}$$

$F(\tau)$ of the ribbon converges to that of the cylinder for $t_m = D$.

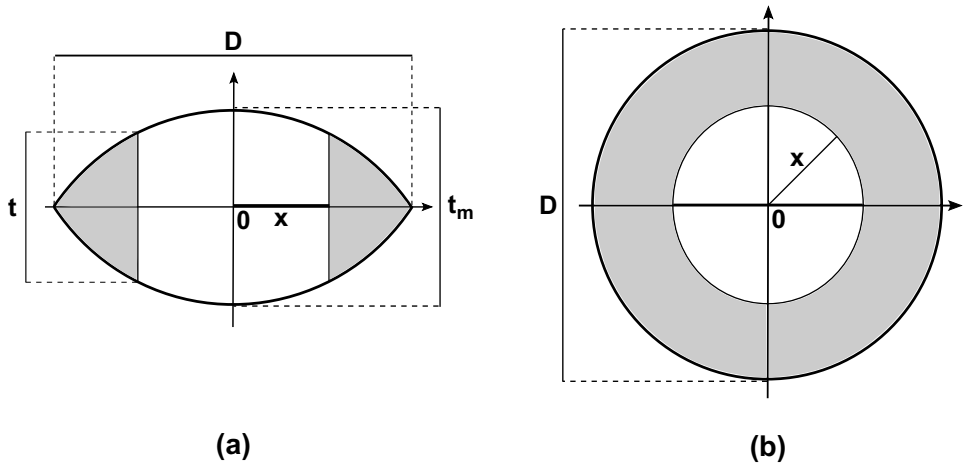

Figure 2.2: (a) Lens in two dimensions formed by the intersection of two disks with the same radius displaced to each other in the vertical direction. (b) Disk with shaded area representing the part of the convex lens with thickness smaller than t.

Convex lens

The convex lens is generated by rotating the two-dimensional lens around the vertical axis (Fig. 2.2(b)). $F(t)$ is the ratio between the area with thickness smaller than t (shaded ring of the Fig. 2.2(b)) and the total area of the disk

$$F(x) = \frac{\pi(\frac{D}{2}^2 - x^2)}{\pi\frac{D}{2}^2} = 1 - \left(\frac{2x}{D}\right)^2. \tag{2.17}$$

Since x is the same as for the ribbon, $x = \frac{D}{2}\sqrt{1 - \tau^2 f^2 - \tau(1 - f^2)}$,

$$F(t) = \tau^2 f^2 + \tau(1 - f^2). \tag{2.18}$$

Some other shapes can be deduced from these previous cases.

If $t_m = D$ for the convex lens, $f = 1$, and the lens becomes a sphere with $F(t) = \tau^2$. On the other hand, if $D \longrightarrow \infty$, $f \longrightarrow 0$ and the cumulative distribution function $F(\tau)$ will be that of a wedge. The cumulative distribution functions of the shapes considered here are plotted on Fig. 2.3 in function of the reduced thickness.

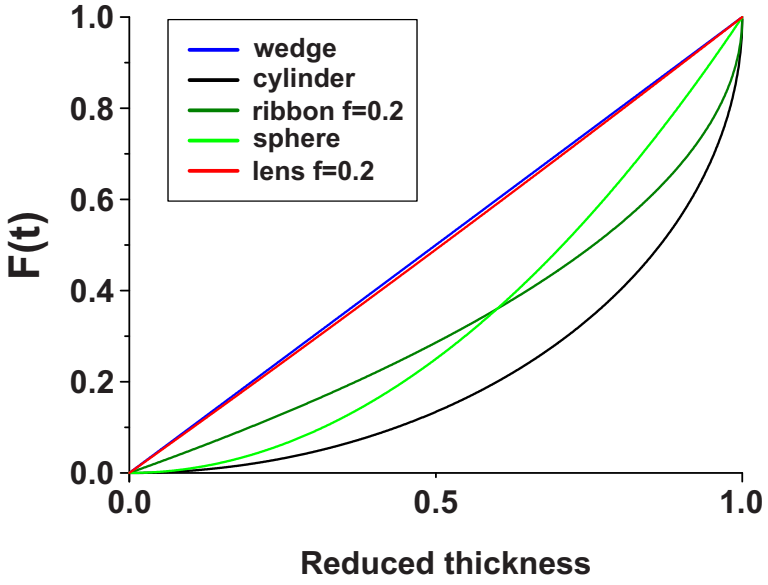

Figure 2.3: Cumulative density function as a function of the reduced thickness plotted for wedge, cylinder, ribbon (2D lens), sphere and convex lens.

As can be seen in the plot (Fig. 2.3), the $CDF(t)$ of the regular 3D lens evolves from the sphere ($D = t_m$) to an approximately linear behavior for the lens with proportion $D : t_m = 1 : 5$. The situation when the lens has both length and thickness equal is equivalent to an isotropic crystalline nanoparticle.

2.3 Dynamical refinement of PEDT data

During the development of this thesis the dynamical refinement was tested in order to identify the behavior of the parameters of the method [43]. For each sample a reference structure was available, which could be compared to the results obtained by the dynamical refinement of PEDT data. The comparison between the two models evidenced the accuracy which might be achieved by the method, as well as the limitations. One of the samples tested was Ni_2Si, which is presented in section 2.4.2.

The methodology used during the verification of the parameters of the dynamical refinement follows below, where we describe the data collection and the refinement of the structure parameters until the final comparison with results from single crystal X-ray diffraction (SCXRD).

2.3.1 Data collection

After finding a suitable crystal giving intense diffraction pattern, the precession angle is aligned, the goniometer is tilted to the minimum angle, and the automated process of data collection starts. Electron diffraction tomography was performed using the in-house module RATS (Record Automated Tilt Series), which reduces the exposure time of the sample under the beam and optimizes the total measurement time, since almost no intervention of the user is necessary. In the semi-automated mode used here, the user defines the minimum angle where to begin the data acquisition. RATS tilts the sample to the minimum angle of the goniometer, takes and saves the diffraction pattern at this position, tilts the sample by a small angle determined by the user, and let the user check the position of the crystal. If necessary, the crystal is manually moved back to stay under the beam and another diffraction pattern is taken and recorded by RATS.

2.3.2 Data processing and structure solution

Intensities obtained by EDT must be extracted from ED patterns to be used in the structure solution, which was done using PETS (Process Electron Tilt Series) [44]. The procedure is very similar to the standard processing of X-ray diffraction data. Diffracted intensities are searched on the frames, the positions are recalculated to the 3D coordinates in reciprocal space, and a difference vector space is calculated from the obtained vectors [44], in a process similar to the procedure described in [20, 21].

The list of reflection and positions is imported to Jana2006 and the graphical interface for indexing is used for finding the lattice parameters and the orientation matrix of the crystal. This matrix is imported to PETS, which uses this matrix to integrate the reflection intensities. Two types of integration are possible. The first one is useful for the structure solution and for the kinematical refinement, where intensities belonging to the same reflection on adjacent frames are integrated together. This kinematical integration results in a list of intensities containing one entry per each hkl triplet. The second integration type, used for the dynamical refinement, integrates the intensities independently on every frame. In this case, different frames might have entries for the same hkl triplet, and in the output each entry is identified both by the number of the frame on which it was observed and by the hkl triplet.

The output file with the list of integrated intensities in the kinematical approach can be imported to a standard crystallographic software for structure solution. Here it was imported to Jana2006, which uses Superflip [45] to solve the structure. This model can be refined using the kinematical approximation. The output using the dynamical approach can be imported to Jana2006 for the dynamical refinement.

2.3.3 Structure refinement

Least-squares refinement is the method of choice to refine crystal structure parameters. It is well established and frequently used for X-ray and for neutron single-crystal data. The standard full-matrix least-squares refinement is also used in the dynamical refinement performed in Jana2006. During the dynamical refinement it is necessary to select which reflections should be considered in the least-squares refinement. The selection is performed using two kinds of parameters that are specific to the dynamical refinement: Parameters related to data selection, which are used to decide which reflections of the diffraction pattern can be considered during the refinement, and parameters that select which beams will be considered in the structure matrix. The parameters used during the data selection are specific to the dynamical refinement and have no equivalent in X-ray diffraction procedure.

The selection of the reflections from each diffraction pattern, or frame, is done using two parameters. The first one is the excitation error $S_{\mathbf{g}}$(refine)

$$S_{\mathbf{g}} = \frac{|\mathbf{K}|^2 - |\mathbf{K}+\mathbf{g}|^2}{2\mathbf{K}}, \tag{2.19}$$

which is used to select reflections according to their distance to the Bragg condition. The excitation error is a distance in the reciprocal space and it is given in units of reciprocal Ångström. If a high $S_{\mathbf{g}}$(refine) is used, a large number of reflections is included in the refinement, but reflections which are further from the Bragg condition might be weaker.

The second parameter is $R_{S_{\mathbf{g}}}$. This parameter is defined as the ratio between the excitation error without precession and the maximum excitation error change reached by the precession circuit

$$R_{S_{\mathbf{g}}} = \frac{|S^0_{\mathbf{g}}|}{|\mathbf{g}|\varphi}, \tag{2.20}$$

which identifies how much a reflection is covered by the precession motion. Reflections which are further than a certain fraction of the precession amplitude are not well covered by the precession and, therefore, are not considered for the refinement. $R_{S_{\mathbf{g}}}$ forms a belt around the Ewald sphere, as can be seen in Fig. 2.4.

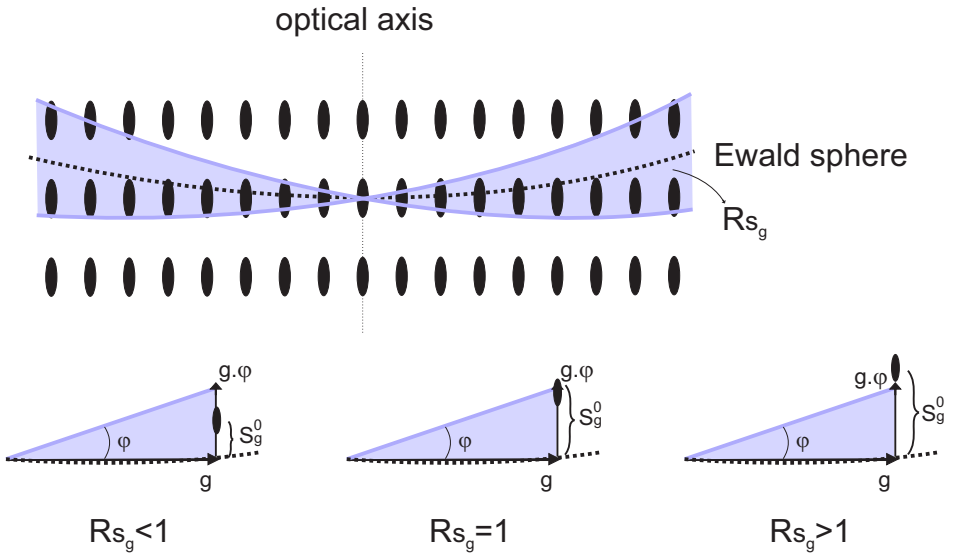

Figure 2.4: $R_{S_{\mathbf{g}}} = \frac{S^0_{\mathbf{g}}}{\mathbf{g}\phi}$ is the coverage of the reciprocal lattice because of the precession of the beam around the optical axis. Three examples of $R_{S_{\mathbf{g}}}$ are shown: $R_{S_{\mathbf{g}}} < 1$, $R_{S_{\mathbf{g}}} = 1$ and $R_{S_{\mathbf{g}}} > 1$.

For instance, $R_{S_{\mathbf{g}}}$=0.5 includes reflections which are twice under Bragg condition during the precession, while $R_{S_{\mathbf{g}}}$=1 includes reflections which satisfies the Bragg condition only once by the precession circuit. Note that $R_{S_{\mathbf{g}}}$ is specific for data collected using precession and for data collected without it the selection of reflections is performed by $S_{\mathbf{g}}$(refine).

The parameters used for selecting the structure factors which will be considered in the calculated intensities are $S_{\mathbf{g}}$(matrix) and $\mathbf{g}_{\max}$. $S_{\mathbf{g}}$(matrix) is the maximum excitation error and $\mathbf{g}_{\max}$ is the limit on the resolution of the reflections which will enter the structure matrix. Neither of them is related to the experimental data and they must be in agreement with the parameters which are used to select the experimental reflections ($S^{\max}_{\mathbf{g}}$ and $\mathbf{g}$).

Another parameter used during the dynamical refinement is N_{steps}, which is only used if the data was collected with the precession of the beam and it specifies the number of points to which the diffracted intensities should be integrated on the cycle of the precession.

These parameters of the dynamical refinement are explained in detail in [27, 28, 43].

The thickness and the orientation of the crystal play important role in the intensities and are optimized prior to the refinement of the structure. Before the refinement of the structure parameters, each frame has the weighted residue value

wR(all) calculated for thickness varying from 0 to 2000 Å, in order to estimate an initial thickness. The curve of the thickness as a function of wR(all) allows to asses the quality of the data. Some possible problems which might hamper the thickness estimation are the presence of one very strong reflection or some frames with very weak reflections, due to crystal degradation, for example. If a problematic frame is observed during the thickness evaluation, this frame should be removed from the list of frames to be used during further analysis because it contains intensities collected under different conditions than the rest of the data. Another possibility is to use an average of the thicknesses for a sample which is believed to have constant thickness. Then, one single value of thickness can be used as initial value for the refinement. Thickness variation due to crystal tilt is internally considered in Jana2006, and the reported value is the true thickness of the sample.

2.4 Tests on the parameters of the dynamical refinement

The behavior of the parameters used during the dynamical refinement was verified by performing a series of tests, where each parameter was modified individually and the results of crystal structure parameters obtained by the dynamical refinement were compared to those using SCXRD. One of the samples analyzed was Ni_2Si, presented in section 2.4.2. The results of the tests on four other samples are presented in details in [43].

The tests followed the sequence of steps:

- Initial kinematical model: The data was integrated by PETS by the kinematical approach, the structure was solved using Superflip and the kinematical approximation was used for the refinement. Unrealistic parameters, such as negative atomic displacement parameters (ADPs) were changed to a more realistic value prior to further treatment of the model by dynamical refinement.

- Inclusion of the data integrated by the dynamical approach: Keeping the initial kinematical model for the refinement, the list of intensities integrated by the dynamical approach was imported to Jana2006.

- Thickness estimation: Weighted R-value as a function of the thickness was calculated for each frame. The thickness which is closer to the real one of each frame gives the lowest wR_1. An average of the thicknesses of all frames might be calculated and used as an initial estimate of the sample thickness.

In cases where the sample has a different shape, there is the option to use a geometric approximation of ideal shapes during the dynamical refinement in Jana2006 (see section 2.2.1). This option was also used here.

- Dynamical refinement: Least-squares refinement of the structure parameters was performed using the default values of the parameters of the dynamical refinement [43]: $S_g^{\max}$(refine)= 0.1 Å^{-1}, $R_{S_g}^{\max} = 0.4$, $S_g^{\max}$(matrix)= 0.01 Å^{-1}, $g_{\max}$(matrix)= 2.0 Å^{-1} and $N_{steps} = 128$. The structure parameters refined were the atomic coordinates, isotropic atomic displacement parameters and scale factors of individual frames. All the refinement processes were conducted until convergence. After the optimization of the parameters, an orientation optimization was performed using a downhill simplex algorithm [27]. Problematic frames were identified according to the value of the optimized tilts and these misoriented frames were removed from the list of frames to be used during the refinement. Another structure refinement was performed, using the optimized parameters. If necessary, extra refinements were performed, depending on the evaluation of the results. The refinement using these default values of parameters was considered as the starting point for systematic tests.

- The tests: Optimized parameters were $S_g^{\max}$(refine), $R_{S_g}^{\max}$, $S_g^{\max}$(matrix), $g_{\max}$(matrix) and N_{steps}. One of these parameters was changed at time, keeping all the other parameters fixed, and the structure was refined until the convergence.

The model from each refinement using different parameters was evaluated based on the R-values, specifically R_1(obs) and wR_1(all), and based on the comparison with the reference structure. For the reference structure model, a high-quality model was either obtained by single-crystal X-ray or used from the literature. The refined structure models were compared with the reference structure based on the average and maximum distance between an atom and the corresponding atom in the reference structure. These two quantities are denoted here as Average Distance to Reference Atoms (ADRA) and Maximum Distance to Reference Atoms (MDRA).

Another refinement was performed using the two-beam model [46], as used already in Palatinus *et al.* [27]. In the two-beam model only the primary beam and one diffracted intensity are considered as the excited beams in one orientation. This model allows a comparison more equivalent to the full dynamical refinement than the kinematical refinement, since it uses the same data and the same number of parameters, but only two beams are considered as excited, instead of n beams, as for the full method. On the other hand, the kinematical refinement has no

equivalent to the dynamical one concerning the number of parameters and data points used.

2.4.1 Application of the dynamical refinement on nickel silicides

Nickel silicides became known for their low electrical resistivity, adequate work function, thermal stability, low Si consumption, and formation controlled by Ni diffusion. These properties attracted interest in their use as ohmic contacts to complementary metal-oxide-semiconductor (CMOS) devices in the source [47, p. 5], drain and gate [48, 49]. There are six stable phases at room temperature [50, 51]: Ni_3Si, $Ni_{31}Si_{12}$, Ni_2Si, Ni_3Si_2, NiSi and $NiSi_2$. Within these nickel silicides, Ni_2Si is widely used as interconnectors of semiconductors devices and gate of integrated circuits (IC) [49, 52]. The reaction of Ni_2Si and NiSi generates the Ni_3Si_2 phase [53, 54, 55], which has potential application in micro and nanosized electronic devices [56], such as Li-ion batteries [57] and photovoltaic devices [58, 59, 60].

2.4.2 Ni_2Si

The first crystal structure of Ni_2Si was obtained from a single crystal using a Weissenberg camera in 1952 by K. Toman [61], and later from powder X-ray diffraction [62]. Since our objective was to use the material as a test structure for the dynamical refinement, a single crystal X-ray data collection was carried out to have a more accurate reference structure model.

Sample preparation

It is important to clarify that all the samples used during the development of this thesis were received from the collaboration with other institutes and their synthesis will be explained here for the better understanding of the content of the thesis. Two kinds of samples were used:

1. Nanowires of nickel silicide, which were synthesized by chemical vapor deposition (CVD) at the Department of Analytical and Material Chemistry, Institute of Chemical Process Fundamentals of the Czech Academy of Sciences by Vladislav Dřínek.

2. Bulk samples of nickel silicides, which were synthesized by arc melting at the Institute of Physics of the Czech Academy of Sciences by Jaromír Kopeček.

Nanowires of Ni_2Si (Fig. 2.5) were grown by CVD using SiH_4 precursor on Ni substrate at a pressure of 110 Pa, at 550 °C. Bulk samples were prepared from

pure elements (purity 99.99 %) by arc melting under argon atmosphere in Edmund-Bühler MAM-1 furnace, and their compositions were verified using Tescan FERA 3 microscope with EDAX Octane 80 mm^2 detector. The melting of the sample Ni_2Si was repeated four times for homogenization, giving a sample with single-phase microstructure composed of elongated grains due to the rapid cooling process on copper plate.

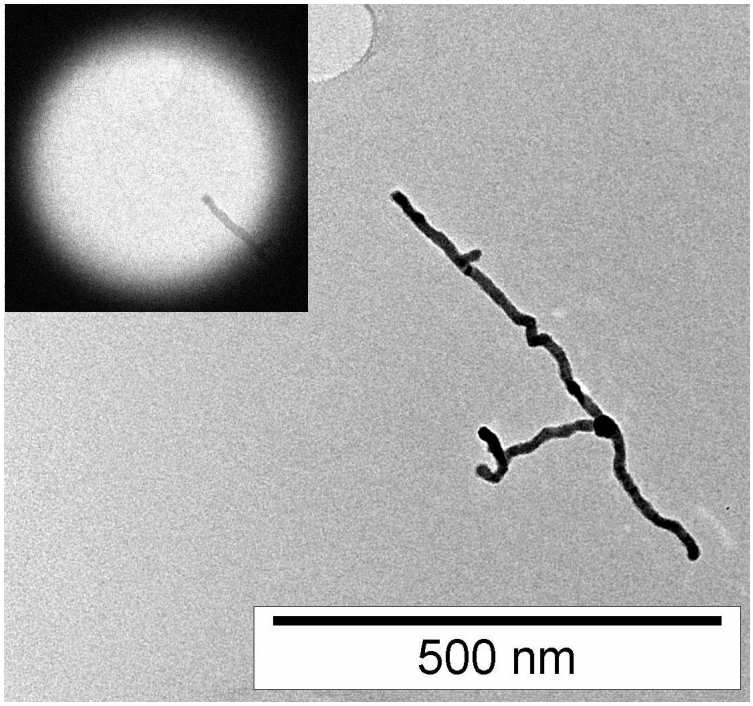

Figure 2.5: Ni_2Si nanowire used for the PEDT data collection. The diameter of the nanowire is 15 nm. The inset shows an image of the illuminated part of the nanowire recorded during the PEDT data acquisition.

Precession electron diffraction tomography

The substrate containing the nickel silicide was scratched to remove the nanowires, which were suspended in ethanol and dropped on a standard Cu grid covered with amorphous carbon foil. Precession electron diffraction tomography was performed in a Philips CM120 TEM with a LaB_6 cathode, at acceleration voltage of 120 kV, equipped with a precession device Nanomegas DigiStar, a CCD camera Olympus SIS Veleta, 2048×2048 pixels 14 bits of dynamical range, and an energy-dispersive analyzer Octane silicon drift detector (SDD) EDAX. The nanowire of Ni_2Si measured had the diameter of 15 nm and 95 nm of illuminated length (Fig. 2.5). The

tilt range was from -25° to 48° with a step of 1°, resulting in 74 frames collected within 20 minutes, and the precession angle used was 1.5°. Details of the measurement are summarized in Table 2.1.

Table 2.1: Experimental details of the PEDT data collection on Ni_2Si nanowire.

Space group	*Pnma*
a (Å)	5.0559
b (Å)	3.7567
c (Å)	7.1055
V (Å^3)	134.9583
Diameter (nm)	15
Length illuminated by the beam (nm)	95
Data collection	
λ (Å)	0.0335
Resolution (Å)	0.746
No of recorded frames	74
precession angle φ (°)	1.5

Single crystal X-ray diffraction

A Ni_2Si single crystal with the dimensions of $0.208 \times 0.178 \times 0.103$ mm^3 was measured at 25 °C in an Agilent Xcalibur Atlas Gemini Ultra diffractometer, equipped with an Atlas detector. The data set was treated by analytical absorption correction (CrysAlisPro; Agilent, 2014). Details of the SCXRD are shown in Table 2.2.

Results - tests on the dynamical refinement

The results of the dynamical refinement and SCXRD were compared based on both the residue values and ADRA (Average Distance to Reference Atoms). The most important outcome is that the dynamical refinement gives better results than that using the kinematical approximation. The second better results come from the two-beam approximation, which gives better results than the kinematical refinement, but its results are not as accurate as those from the dynamical approach. Since the two-beam uses the same number of parameters as the dynamical refinement, this triple comparison unambiguously shows that the better accuracy obtained by the dynamical refinement does not have origin in the higher number of parameters refined, but it comes from the use of the full (n beams) dynamical theory of diffraction. Another essential observation is that most of the parameters of the dynamical refinement have no substantial influence on the results. Provided that

Table 2.2: Experimental and refinement details of the single crystal X-ray data collection on Ni_2Si single crystal.

Space group	*Pnma*
a (Å)	4.9996(7)
b (Å)	3.7261(4)
c (Å)	7.0532(9)
V (Å^3)	131.39(3)
Density (g·cm^{-3})	7.3535
Data collection	
λ (Å) (Mo Kα)	0.71069
Resolution (Å)	0.714
μ (mm^{-1})	28.768
Completeness (%)	98.02
Refinement	
R_1(obs)[1] (%)	1.94
wR(all)[2] (%)	2.57
GOF(all)[3] (%)	1.31
θ_{max} (°)	29.104
Max, Min Fourier density	0.54, -0.62

[1] $R_1 = \frac{\sum ||F_o|-|F_c||}{\sum |F_o|}$

[2] $wR = [\frac{\sum w(F_o^2-F_c^2)^2}{\sum w(F_o^2)^2}]^{1/2}$

[3] $GOF = [\frac{\sum w(F_o^2-F_c^2)^2}{N_{ref}-N_{par}}]^{1/2}$

the computational and data selection parameters are kept within reasonable values, they do not significantly influence the accuracy of the model. ADRA remains mostly constant, while the residue values vary with the data selection parameters.

According to the tests, the general behavior of the parameters of the dynamical refinement can be summarized as follow [43]:

- $S_g^{\max}$(refine) gives better results when set to higher values, which is the expected result because higher $S_g^{\max}$(refine) includes more reflections to the refinement. However, since $S_g^{\max}$(refine) is strongly related to $R_{S_g}^{\max}$, the tests show that the data selection is done effectively by $R_{S_g}^{\max}$. $S_g^{\max}$(refine) can thus be set to a value larger than $R_{S_g}^{\max} \cdot g_{\max} \cdot \varphi$ (from Eq. 2.20). For instance, a data collected using a precession of $\varphi = 3°$, using $g_{\max} = 2.0$ Å^{-1} and $R_{S_g}^{\max} = 1$ would give $S_g^{\max}$(refine)=0.1 Å^{-1}. According to tests on other samples [43] $S_g^{\max}$(refine)=0.3 Å^{-1} can be considered large enough, effectively infinite. For cases where precession is not used, $R_{S_g}^{\max}$ is zero and the data selection will completely rely on $S_g^{\max}$(refine). For such cases $S_g^{\max}$(refine)

should be large enough to select all the important reflections for the refinement, but since no precession is used ($\varphi = 0°$), $S_g^{\max}$(refine)=0.01 Å^{-1} can be enough [43]. $S_g^{\max}$(refine)=0.025 Å^{-1} was used for Ni_2Si.

- $R_{S_g}^{\max}$ is the parameter whose value has the largest influence on the results of the refinement. Low $R_{S_g}^{\max}$ values (such as 0.15 [43]) select reflections which are closer to Bragg condition and limit the number of reflections in the refinement. This gives low R_1 values, but since a smaller number of reflections is included in the refinement the data-to-parameter ratio is also lower and the accuracy of the model will decrease. $R_{S_g}^{\max}$ higher than 0.8 selects reflections which are not well covered by the precession movement of the beam (Fig. 2.4) and the result is an increased R_1 and ADRA values. Provided that the ratio data-to-parameter is higher than 10, $R_{S_g}^{\max}$ 0.4 is considered a reasonable value [43]. Otherwise, $R_{S_g}^{\max}$ should be increased until the data-to-parameter ratio of at least 10 is achieved, in order to ensure the accuracy of the refinement. This was the case of Ni_2Si, which had $R_{S_g}^{\max}$=0.75 to have at least 10 reflection per parameter refined.

- $S_g^{\max}$(matrix) above 0.01 Å^{-1} resulted in increased ADRA for most of the samples tested [43]. Refinement including higher values of $S_g^{\max}$(matrix) allows a larger number of intensities used in the structure matrix and thus the expected results would be that more intensities used for the refinement would give better accuracy - lower ADRA and ideally lower R_1 values. This increase on ADRA for $S_g^{\max}$(matrix) larger than 0.01 Å^{-1} was observed in previous results [27], but it is the opposite of the expected result. I might be that beams which are further than 0.01 Å^{-1} from the Ewald sphere are more sensitive to crystal imperfections. Given that the model is constructed for an infinite perfect crystal, it might be that the diffraction of the beams with a high S_g depart so much from the real situation that it becomes less accurate to include them than to leave them out completely. Based on the tests, $S_g^{\max}$(matrix) 0.01 Å^{-1} is considered a safe value and it was the one used for Ni_2Si.

- $g_{\max}$ and N_{steps} are the parameters with the lowest influence on the model. $g_{\max}$ should be larger than the maximum experimental value to include all the data within the experimental resolution. $g_{\max}$ =1.5 Å^{-1} is enough for a data set acquired with a resolution of $g_{\max}^{\exp}$ =1.4 Å^{-1}. Slightly higher values might be used for the last steps of the refinement, as shown by the tests on other samples [43], but $g_{\max}^{\exp} > 2.0$ Å^{-1} do not result in any improvement of the refinement accuracy. The influence of N_{steps} on the refinement is surprisingly low, as observed by Palatinus *et al.* [43] during the tests on several data sets. N_{steps}=96 gives good results, but 128 is more appropriate

for the last refinement cycles in order to ensure a more accurate result. $g_{\max}$ =2.0 Å^{-1} and N_{steps}=128 was used for Ni_2Si.

In summary two parameters are dominant in the results, namely $S_g^{\max}$(refine) and $R_{S_g}^{\max}$. According to the tests the parameters are recommended to be [43]: $S_g^{\max}$(refine) effectively infinite, $R_{S_g}^{\max} = 0.4$ if the data-to-parameter ratio permits, $S_g^{\max}$(matrix)= 0.01 Å^{-1}, $g_{\max}$(matrix)= 2.0 Å^{-1} and $N_{steps} = 128$.

For Ni_2Si the optimum refinement was obtained using $S_g^{\max}$(refine)= 0.025 Å^{-1}, $R_{S_g}^{\max} = 0.75$ and the default value for the other parameters. The results of the test for Ni_2Si are shown in Table 2.3, for which the recommended values of the parameters were used and one parameter was changed per time.

The first thing to note is that the kinematical refinement already gave accurate results for this nanowire, most probably because it was a very thin sample, with the diameter of 15 nm. Refining anisotropic atomic parameters in the kinematical refinement decreased both the R_1 value and ADRA from 11.07 % to 8.88 %, and from 0.02035 Å to 0.1670 Å, respectively. The two-beam refinement gave more accurate results than the kinematical one, but still worse than the complete dynamical refinement, in agreement with the results on other samples [43].

Within the full dynamical refinement, optimization of the orientation was shown to yield better R values and lower ADRA values [43]. Usually the deviations are around 0.1 or 0.2°, and when the orientation parameters diverge over 0.5° these frames should be removed from the refinement, because they contain some problem that causes instability during the orientation optimization. These instabilities might be due to a small shift of the crystal during the data acquisition, a different piece of sample illuminated for one frame, or a small number of reflections on the frame for example. All these effects might generate a deviation of orientation, and frames containing these deviations are not suitable for the refinement process, since they were collected at different conditions than the other frames. Ni_2Si had eight frames removed. The reasons, in general, were either the small number of reflections on the frame or one reflection much stronger than the rest. Even though Ni_2Si has a small unit cell, the data was collected on a thin nanowire, and these eight frames were removed of the refinement, the optimization of orientation improved ADRA (0.01057 Å to 0.00826 Å), MDRA (0.01471 Å to 0.01351 Å) and R_1 (9.64 % to 7.14 %). Refining anisotropic atomic displacements improved the model even more. ADRA decreased from 0.00826 Å to 0.00554 Å, MDRA from 0.01351 Å to 0.00840 Å, and the residue value R_1 reduced from 7.14 % to 6.36 %.

Since the data was obtained for a nanowire, the average of the thickness of all frames was used as an initial thickness. Thickness variation due to sample tilt was corrected because the nanowire was not lying parallel to the tilting axis, and one refinement considering the cylindrical shape for the sample was also performed.

Table 2.3: Results of the test refinements of Ni_2Si with varying parameters. The first line contains the refinement with default parameters. In subsequent lines the results with one parameter different from the default is shown. Finally a few special refinement tests are summarized.

varied parameter	value	R_1(obs) (%)	wR_1(all) (%)	Nrefl(obs)	Nrefl(all)	ADRA ($Å^{-1}$)	MDRA ($Å^{-1}$)
all parameters default		7.14	7.56	849	1913	0.00826	0.01351
$R_{S_g}^{\max}$	0.30	5.16	5.61	330	722	0.01857	0.02109
$R_{S_g}^{\max}$	0.40	5.77	6.05	438	1008	0.01679	0.01849
$R_{S_g}^{\max}$	0.50	6.38	6.83	567	1290	0.00959	0.01268
$R_{S_g}^{\max}$	0.60	6.50	7.38	673	1545	0.00901	0.01419
$R_{S_g}^{\max}$	0.70	7.21	7.88	806	1815	0.01067	0.01375
$R_{S_g}^{\max}$	0.80	7.03	7.44	902	2010	0.00801	0.01373
$R_{S_g}^{\max}$	0.90	7.12	7.71	981	2150	0.00724	0.01016
$R_{S_g}^{\max}$	1.00	7.01	7.39	1033	2225	0.00795	0.01103
$R_{S_g}^{\max}$	1.25	7.43	7.95	1099	2359	0.00694	0.00829
$R_{S_g}^{\max}$	1.50	7.77	8.20	1134	2433	0.00595	0.00848
$S_g^{\max}$(refine)	0.005	3.22	3.76	211	433	0.01170	0.01507
$S_g^{\max}$(refine)	0.010	5.49	5.83	440	963	0.01200	0.01516
$S_g^{\max}$(refine)	0.015	6.33	6.72	650	1400	0.01018	0.01327
$S_g^{\max}$(refine)	0.020	6.88	7.22	779	1724	0.00858	0.01157
$S_g^{\max}$(refine)	0.030	7.24	7.82	853	1941	0.00725	0.01114
$g_{\max}$(matrix)	1.5	7.18	7.60	852	1918	0.00897	0.01391
$g_{\max}$(matrix)	3.0	7.14	7.56	852	1917	0.00890	0.01363
$S_g^{\max}$(matrix)	0.0075	7.37	7.70	844	1912	0.00894	0.01611
$S_g^{\max}$(matrix)	0.0125	7.06	7.60	848	1898	0.00803	0.01162
$S_g^{\max}$(matrix)	0.015	6.85	7.26	839	1897	0.00915	0.01242
$S_g^{\max}$(matrix)	0.020	6.81	7.18	843	1908	0.01088	0.01661
$S_g^{\max}$(matrix)	0.025	6.81	7.22	850	1894	0.01088	0.01533
$S_g^{\max}$(matrix)	0.030	6.81	7.19	845	1890	0.01206	0.01594
N_{steps}	32	7.18	7.84	850	1919	0.01040	0.01593
N_{steps}	48	7.25	7.93	851	1925	0.00844	0.01377
N_{steps}	64	7.11	7.54	857	1925	0.00803	0.01377
N_{steps}	96	7.14	7.57	853	1920	0.00870	0.01440
N_{steps}	256	7.14	7.60	854	1920	0.00808	0.01178
kinematical refinement		11.07	11.53	88	118	0.02035	0.02843
kinematical anisotropic ADP		8.88	8.59	88	118	0.01670	0.02313
two-beam		7.89	8.76	865	1937	0.01860	0.02186
no orientation optimization		9.64	10.86	857	1942	0.01057	0.01471
anisotropic ADP		6.36	7.00	851	1912	0.00554	0.00840
Dynamical cylinder		7.25	10.34	721	1660	0.00730	0.01060

The refinement using the cylindrical shape was slightly better than the standard refinement using the plate model. It indicates that using an idealized crystal shape improves the model, but the general assumption of a crystal slab is not detrimental to the accuracy of the refined model for such a thin nanowire. The results of all these tests are included in Table 2.3. Both the isotropic and anisotropic atomic displacements were positive definite since the kinematical refinement. Ni_2Si was the model with the most accurate results within the tests performed by Palatinus *et al.* [43], mostly likely because of the small number of atoms in the unit cell. The atomic coordinates and the atomic distances to the reference structure are

shown in Table 2.4, for kinematical and dynamical refinements. These results show that the dynamical refinement gives accuracy approaching that of SCXRD, with a maximum difference of the atomic position from the reference structure smaller than 0.01 Å.

Table 2.4: Fractional coordinates for the three independent atoms of Ni_2Si obtained by kinematical and dynamical refinements, and from the reference structure. Distances to the reference structure are also shown. The fractional coordinate y is symmetry-restricted to 0.25 for all atoms.

Atom	coordinate	kinematical	dynamical	reference
Ni1	x	0.175(2)	0.1699(6)	0.17026(14)
	z	0.0609(8)	0.0612(2)	0.06027(9)
Ni2	x	0.041(2)	0.0446(6)	0.04204(14)
	z	-0.2925(7)	-0.29343(19)	-0.29389(10)
Si1	x	-0.289(4)	-0.2884(9)	-0.2877(3)
	z	0.1105(11)	0.1140(3)	0.1144(2)
Distance to the position in the reference structure (Å)				
Ni1-Ni1$_{ref}$		0.022(11)	0.0065(18)	
Ni2-Ni2$_{ref}$		0.010(6)	0.014(3)	
Si1-Si1$_{ref}$		0.028(9)	0.005(4)	

2.4.3 Ni_3Si_2

Ni_3Si_2 had its structure determined by single crystal data from a Weissenberg camera and the unit cell determined by powder diffraction in 1961, space group identified as $Cmc2_1$ based on the Patterson sections [63]. However, since no further explanation was given, we can only speculate that they used Harker sections, which are sections of the Patterson maps containing a large amount of interpretable data, for the interpretation of the symmetry. Patterson maps represent the interaction between every pair of atoms and they are of difficult interpretation. During our structure analysis of Ni_3Si_2 nanowires by electron diffraction the space group was identified to be the centrosymmetric $Cmcm$. Given the wide scope of application of nanomaterials and the correlation between structure and properties, accurate structure solution of nanocrystals is of great importance and interest. Hence, we used the dynamical refinement to refine the crystal structure of Ni_3Si_2. Results demonstrate that the assignment of the noncentrosymmetric space group $Cmc2_1$ is incorrect and that the correct space group is $Cmcm$. In order to confirm the results and verify the accuracy of the model, an approach similar to that used for Ni_2Si was used.

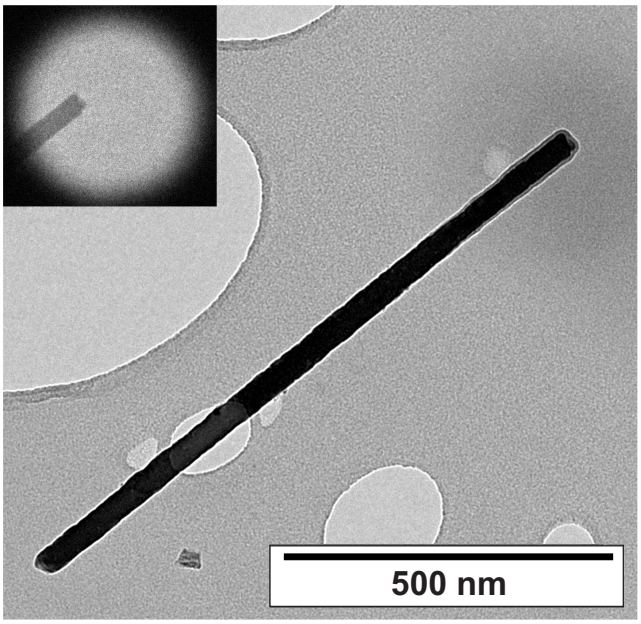

Figure 2.6: TEM image of the Ni_3Si_2 nanowire used for the PEDT data collection. The diameter of the nanowire is 35 nm. The inset shows an image of the part illuminated on the nanowire during the data acquisition.

Sample preparation

Ni_3Si_2 (Fig. 2.6) were grown by CVD using SiH_4 precursor on Ni substrate at 110 Pa, at 500 °C. Bulk samples were prepared from pure elements (purity 99.99 %) by arc melting under the argon atmosphere in Edmund-Bühler MAM-1 furnace. Bulk sample Ni_3Si_2 was homogenized by repeating the melting five times, giving a sample with rough casting microstructure with voids between the grains, and with grains elongated in the thermal gradient direction. The sample composition was verified using Tescan FERA 3 microscope with EDAX Octane 80 mm^2 detector. Border parts of the sample contained an eutectic mixture of Ni_3Si_2 with the admixture of Ni_2Si.

Precession electron diffraction tomography

Nickel substrate was scratched to remove the nanowires, which were suspended in ethanol and dropped on a Cu grid covered with carbon foil. The selected nanocrystal of Ni_3Si_2 had the diameter of 35 nm and total length of 1 μm. The length of the illuminated part of the nanowire was 150 nm, as shown in Fig. 2.6. The data collection was performed with a tilt series in the range -56° – 55°, which gave 112 frames in a total time of 30 minutes. Parameters of the PEDT

measurement are summarized in Table 2.5.

Table 2.5: Experimental details of the PEDT data collection on Ni_3Si_2.

Crystal data	
Chemical formula	Ni_3Si_2
Crystal system, space group	Orthorhombic, *Cmcm*
a, b, c (Å)	12.35, 10.92, 6.98[1]
V (Å^3)	940.998
Z	16
λ (Å)	0.0335
Diameter×length (nm^2)	35×1000
Length illuminated by the beam (nm)	150
Density (g·cm^{-3})	6.5572
Data collection	
Temperature (°C)	20
h_{min} h_{max}, k_{min} k_{max}, l_{min} l_{max}	-15 14, -15 15, -9 9
Resolution (Å)	0.7163
No of recorded frames	112
Precession angle φ (°)	2.0
Completeness (%), θ_{full} (°)	82.00, 0.95
No. of measured, independent and observed reflections [I> 3σ(I)]	25248, 8250, 4681
Dynamical Refinement (anisotropic atomic displacement parameters)	
R_1(obs), wR(all), GOF (obs/all)(%)	8.23/13.48, 8.04/9.70, 2.37/2.16
No. of refined parameters	170

[1]Unit cell parameters from EDT are known to have distortions and lower accuracy [21, 11].

Single crystal X-ray diffraction (SCXRD)

Single crystal X-ray data was acquired in an Agilent Xcalibur Atlas Gemini Ultra diffractometer, equiped with an Atlas detector, for which the data sets were treated by analytical absorption correction (CrysAlisPro; Agilent, 2014). The measured Ni_3Si_2 single crystal had the dimensions of 0.101 × 0.065 × 0.044 mm^3 at 25 °C. Information about the SCXRD measurement are presented in Table 2.6.

Results

Both datasets from PEDT and SCXRD were solved using Superflip [45] without prior information on the symmetry [65]. The structure solution readily indicated the space group *Cmcm*. The final SCRXD model gave low residue values and small residual electron density, and thus it was considered as a suitable reference

Table 2.6: Experimental details of the single crystal X-ray data collection on Ni_3Si_2.

Crystal data	
Chemical formula	Ni_3Si_2
Crystal system, space group	Orthorhombic, *Cmcm*
a, b, c (Å)	12.2174(9), 10.8014(7), 6.9222(4)
V (Å^3)	913.49(10)
Z	16
λ (Å) (Mo Kα)	0.71073
Specimen size (mm^3)	$0.101 \times 0.065 \times 0.044$
Density (g·cm^{-3})	6.7547
μ (mm^{-1})	25.099
Data collection	
Temperature (°C)	25.00(10)
h_{max} k_{max} l_{max}	15 14 9
Resolution (Å)	0.7280
Absorption correction	Analytical [CrysAlis Pro [64], based on crystal shape].
T_{max}, T_{min}	0.489 0.212
Rint(obs/all) (%)	3.81/3.87
Completeness (%), θ_{full} (°)	98.00, 28.88
No. of measured, independent and observed reflections [I> 3σ(I)]	7705, 676, 609
Refinement	
R_1(obs), wR(all), GOF (obs/all)(%)	1.65/2.21, 1.98/2.14, 1.19/1.21
$\Delta\rho_{max}$, $\Delta\rho_{min}$ (e Å^{-3})	0.52 -0.58
No. of refined parameters	59

model. Following the same procedure as for Ni_2Si, the comparison between the models obtained by PEDT and SCXRD was performed using ADRA and MDRA. The parameters used during the dynamical refinement were set to their standard values, according to the tests performed previously for Ni_2Si and other samples [43]. However, since $R_{S_g}^{\max}$ is the parameter with the largest influence on the results of the refinement, we decided to test $R_{S_g}^{\max}$ in the interval between 0.2 and 2.0 for Ni_3Si_2 as well. Fig. 2.7 shows that the behavior of $R_{S_g}^{\max}$ agrees with the previous results [43], as it gives the minimum ADRA for $R_{S_g}^{\max} = 0.4$. Hence, the recommended values were used for all the parameters: $S_g^{\max}$(refine)=∞, $R_{S_g}^{\max}$=0.4, $S_g^{\max}$(matrix)=0.01 Å^{-1}, N_{steps}=128 and $g = 2$ Å^{-1}. Since the nanowire was lying almost along the tilt axis, no correction of crystal tilt was used and the thickness was refined as being the same for all frames.

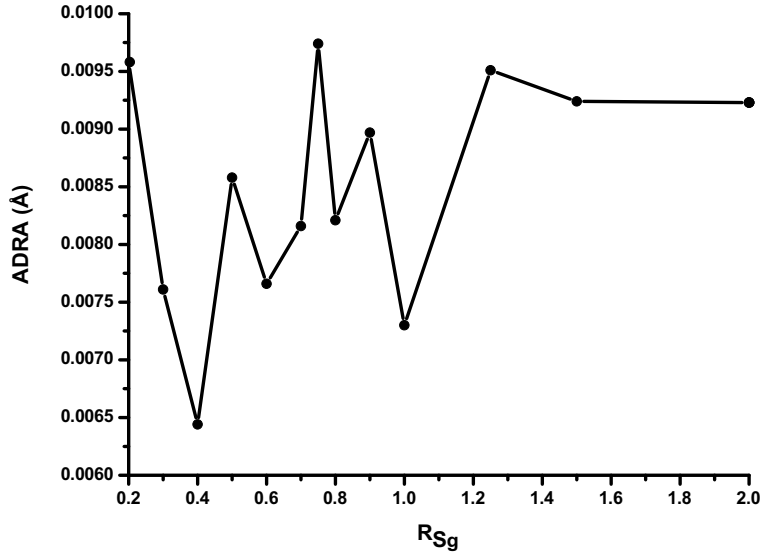

Figure 2.7: Average distance to reference atomic position (ADRA) with varying R_{S_g}, where $R_{S_g} = \frac{|S^0_{\mathbf{g}}|}{|\mathbf{g}|\varphi}$. Test performed to check the optimal R_{S_g} to be used during the dynamical refinement. The lowest ADRA, for $R_{S_g} = 0.4$, is in agreement with the results from [43].

Results - crystal structure redetermination

The PEDT data integrated with the kinematical approach had 549 observed reflections from the total of 571. The refinement with isotropic atomic displacement parameters resulted in 28 parameters to be refined. This number of parameters increased to 59 when the ADPs were refined as anisotropic. The data-to-parameter ratio was thus 20 and 10 for the models with isotropic and anisotropic ADPs, respectively. The model obtained on this thin nanowire gave good results already for the kinematical refinement. Nevertheless, an improvement of the model was observed with the dynamical refinement.

For instance, the kinematical refinement gave R_1=17.95 %, which reduced to 8.45 % when the dynamical approach was taken. The distances from the reference atoms also decreased. $ADRA_{kin}$=0.01634 Å decreased to $ADRA_{dyn}$=0.00647 Å (Table 2.7). Moreover, one atom had negative definite isotropic ADP for the kinematical refinement. This number increased to six when the ADPs were refined as anisotropic. On the other hand, the dynamical refinement resulted in both isotropic and anisotropic positive definite ADPs (Table 2.8). As for the atomic positions, the largest difference from the SCXRD model for the kinematical refinement was 0.0044 in fractional coordinates. The standard deviations of the kinematical refinement were higher than 3σ for three of the 17 pairs of atomic

coordinates compared, with a maximum of 4.0σ (Table 2.9).

Table 2.7: Residue values, atomic distances and ADRA compared to the X-ray model, for kinematical and full dynamical PEDT refinements (isotropic and anisotropic atomic displacements) on Ni_3Si_2.

Parameter	Kinematical	Kinematical(aniso)	Dynamical	Dynamical(aniso)
R_1(obs) (%)	17.95	17.12	8.45	8.23
wR(all) (%)	21.34	20.03	9.98	9.70
GOF(all) (%)	12.82	12.39	2.22	2.16
Nrefl(obs)	549	549	4681	4681
Nrefl(all)	571	571	8250	8250
Nparameters	28	59	139	170
Distance to the atomic position from the X-ray model (Å)				
Ni2-Ni2	0.01088	0.00735	0.00353	0.00310
Ni3-Ni3	0.00933	0.00452	0.00612	0.00598
Ni4-Ni4	0.01324	0.00947	0.01402	0.01538
Ni5-Ni5	0	0	0	0
Ni6-Ni6	0.02121	0.01817	0.01298	0.01321
Ni8-Ni8	0.00106	0.00185	0.00559	0.00639
Si1-Si1	0.03367	0.02742	0.00288	0.00410
Si2-Si2	0.01058	0.01481	0.01386	0.01225
Si4-Si4	0.04820	0.04901	0.00222	0.00294
Si5-Si5	0.01523	0.01493	0.00352	0.00328
ADRA	0.01634	0.01475	0.00647	0.00666

The data from PEDT integrated using the dynamical approach had 8250 reflections from which 4681 were observed. The model refined with isotropic ADPs had 139 structure parameters refined, while the model with anisotropic ADPs had 170 parameters. This gave a data to parameter ratio larger than 25 in both cases. Only one frame presented a deviation higher than 0.5° during the optimization of the orientation, most likely because of the presence of one reflection with stronger intensity than the rest. This considerable difference in intensities is known to cause irregularities during the optimization of the orientation, and this frame was removed from the data analysis. This procedure was also done for Ni_2Si and for other samples during the tests performed by Palatinus *et al.* [43].

The recommended values of $S_g^{\max}$(refine), $R_{S_g}^{\max}$, $S_g^{\max}$(matrix), N_{steps} and g resulted in a model with standard deviations within 2 to 5 times that of the SCXRD. σ_{PEDT}=3σ_{SCXRD} in average. Five of the 17 pairs of atomic coordinates compared presented differences larger than 3σ, with the maximum difference of 7.5σ (Table 2.10). Note that for the kinematical refinement three pairs of atomic coordinates had differences larger than 3σ and the maximum difference was 4.0σ, but the kinematical refinement resulted in uncertainties around five times larger

Table 2.8: Atomic displacement parameters of single crystal X-ray diffraction, dynamical and kinematical refinements against PEDT data on Ni_3Si_2.

Atom	Parameter	X-ray	PEDT(dynamical)	PEDT(kinematical)
Ni2	U_{11}	0.0063(2)	0.0112(10)	0.016(4)
	U_{22}	0.0070(2)	0.0069(5)	0.0048(19)
	U_{33}	0.0070(2)	0.0065(4)	0.004(2)
	U_{12}	-0.00114(13)	-0.0007(5)	-0.0004(15)
	U_{13}	0.00113(13)	0.0014(5)	-0.0002(19)
	U_{23}	-0.00070(14)	-0.0009(3)	-0.0008(12)
Ni3	U_{11}	0.0105(3)	0.0176(17)	0.016(5)
	U_{22}	0.0089(3)	0.0079(8)	-0.001(2)
	U_{33}	0.0065(3)	0.0077(6)	0.004(3)
	U_{12}	-0.0040(2)	-0.0056(7)	0.000(2)
	U_{13}	0	0	0
	U_{23}	0	0	0
Ni4	U_{11}	0.0076(3)	0.0159(18)	0.014(6)
	U_{22}	0.0095(3)	0.0095(7)	0.010(3)
	U_{33}	0.0128(3)	0.0142(6)	0.012(3)
	U_{12}	0.0037(2)	0.0040(7)	0.003(2)
	U_{13}	0	0	0
	U_{23}	0	0	0
Ni5	U_{11}	0.0047(3)	0.010(2)	0.013(7)
	U_{22}	0.0054(3)	0.0032(10)	0.002(3)
	U_{33}	0.0096(4)	0.0122(8)	0.006(4)
	U_{12}	0	0	0
	U_{13}	0	0	0
	U_{23}	0.0002(3)	0.0000(7)	-0.001(2)
Ni6	U_{11}	0.0062(3)	0.0100(16)	0.018(5)
	U_{22}	0.0060(3)	0.0061(7)	0.000(2)
	U_{33}	0.0067(3)	0.0081(5)	0.004(3)
	U_{12}	0	0	0
	U_{13}	0	0	0
	U_{23}	-0.0010(2)	0.0000(5)	0.0041(16)
Ni8	U_{11}	0.0055(4)	0.014(2)	0.015(8)
	U_{22}	0.0056(4)	0.0064(11)	0.003(4)
	U_{33}	0.0109(4)	0.0129(9)	0.006(4)
	U_{12}	0	0	0
	U_{13}	0	0	0
	U_{23}	0	0	0
Si1	U_{11}	0.0073(5)	0.016(3)	0.014(10)
	U_{22}	0.0062(5)	0.0048(13)	-0.001(4)
	U_{33}	0.0066(5)	0.0033(10)	0.004(5)
	U_{12}	-0.0014(4)	-0.0013(12)	-0.007(4)
	U_{13}	0	0	0
	U_{23}	0	0	0
Si2	U_{11}	0.0077(4)	0.012(2)	0.020(8)
	U_{22}	0.0114(4)	0.0086(10)	0.009(4)
	U_{33}	0.0109(5)	0.0151(9)	0.010(4)
	U_{12}	0.0024(3)	0.0011(9)	0.001(3)
	U_{13}	0.0021(3)	0.0018(10)	0.007(4)
	U_{23}	0.0042(3)	0.0055(6)	0.009(3)
Si4	U_{11}	0.0099(8)	0.013(4)	0.020(13)
	U_{22}	0.0059(7)	0.007(2)	-0.007(5)
	U_{33}	0.0065(8)	0.0024(14)	-0.005(5)
	U_{12}	0	0	0
	U_{13}	0	0	0
	U_{23}	0	0	0
Si5	U_{11}	0.0135(8)	0.031(5)	0.026(15)
	U_{22}	0.0047(7)	0.000(2)	-0.012(5)
	U_{33}	0.0132(9)	0.0154(18)	0.020(8)
	U_{12}	0	0	0
	U_{13}	0	0	0
	U_{23}	0	0	0

Table 2.9: Coordinates and difference between atomic coordinates from kinematical refinement (isotropic ADPs) against PEDT data and from single crystal X-ray diffraction on Ni_3Si_2.

Atom	Coordinate	$PEDT_{kin}$	X-ray	Difference	Difference/σ
Ni2	x	0.1734(5)	0.17272(3)	-0.0007(5)	1.5
	y	0.1187(4)	0.11837(3)	-0.0003(4)	0.8
	z	-0.0594(6)	-0.06020(6)	-0.0008(7)	1.2
Ni3	x	0.1954(7)	0.19610(4)	0.0007(7)	1.0
	y	0.2476(5)	0.24800(5)	0.0004(5)	0.8
	z	0.25	0.25	0	0
Ni4	x	0.3174(7)	0.31809(4)	0.0007(7)	0.9
	y	0.0019(6)	0.00287(5)	0.0009(6)	1.7
	z	-0.25	-0.25	0	0
Ni5	x	0	0	0	0
	y	0	0	0	0
	z	0	0	0	0
Ni6	x	0	0	0	0
	y	0.2344(5)	0.23414(5)	-0.0003(5)	0.5
	z	0.0647(8)	0.06170(8)	-0.0030(8)	3.6
Ni8	x	0.5	0.5	0	0
	y	-0.1170(7)	-0.11691(6)	0.0001(7)	0.1
	z	-0.25	-0.25	0	0
Si1	x	0.1190(12)	0.11881(9)	-0.0002(12)	0.2
	y	0.0609(9)	0.05784(10)	-0.0031(9)	3.6
	z	0.25	0.25	0	0
Si2	x	0.3495(10)	0.34863(7)	-0.0009(10)	0.9
	y	-0.1581(7)	-0.15804(8)	-0.0001(7)	0.1
	z	-0.0413(12)	-0.04141(12)	-0.0001(12)	0.1
Si4	x	0	0	0	0
	y	0.1608(11)	0.15635(14)	-0.0044(11)	4.0
	z	-0.25	-0.25	0	0
Si5	x	0	0	0	0
	y	0.4063(12)	0.40773(15)	0.0014(12)	1.2
	z	0.25	0.25	0	0

than those obtained by the dynamical refinement. In fractional coordinates, the dynamical refinement resulted in the largest difference of 0.0010 from the SCXRD model, while that of the kinematical counterpart was 0.0044.

Neither ADRA nor R_1 had significant variation when the ADPs were refined as anisotropic. ADRA changed from $ADRA_{iso}$=0.00647 Å to $ADRA_{aniso}$=0.00666 Å, and R_1 decreased from ${R_1}^{iso}$=8.45 % to ${R_1}^{aniso}$=8.23 % (Table 2.7). The ADPs

from the dynamical refinement had closer values to those obtained by the SCXRD than the kinematical refinement (Table 2.8). The agreement between the PEDT and the SCXRD models can clearly be seen through the overlapping of the models shown in Fig. 2.8. Hence, the dynamical refinement resulted in a model with accuracy comparable to that obtained from the SCXRD data.

In order to verify the difference between the actual model using the dynamical refinement and that of Pilström [63] we decreased the symmetry of the model from the dynamical refinement with isotropic ADPs to $Cmc2_1$ and overlapped it with the model by Pilström (Fig. 2.9). As a result of the decrease of symmetry, three out of ten atoms lost the equivalence coming from the center of symmetry. This lost equivalence generated nine atomic parameters with a correlation larger than 0.7 during the refinement. The residue values changed only negligibly. R_1 changed from R_{1Cmcm}^{iso}(obs)=8.45 % to $R_{1Cmc2_1}^{iso}$(obs)=8.44 %, while wR went from wR_{Cmcm}^{iso}(all)=9.98 % to $wR_{Cmc2_1}^{iso}$(all)=9.97 %. In fact, no improvement on the model was achieved with the decrease of symmetry. Hence, the centrosymmetric space group $Cmcm$ is more appropriate for the description of the model.

An analogous test was performed on the SCXRD model. The SCXRD model had the symmetry decreased to $Cmc2_1$ and it was overlapped with that of the model by Pilström, in the same way as for the previous case with the dynamical counterpart. However, the decrease of symmetry gave origin to over 20 parameters with correlation higher than 0.9. Moreover, R_1 of this noncentrosymmetric model increased from R_{1Cmcm}(obs)=1.65 % to R_{1Cmc2_1}(obs)=1.77 %. This is not a significant difference, but it clearly indicates that the centrosymmetric model is the correct one to describe the structure.

Table 2.10: Coordinates and difference between atomic coordinates from dynamical refinement (isotropic ADPs) against PEDT data and from single crystal X-ray diffraction on Ni_3Si_2.

Atom	Coordinate	$PEDT_{dyn}$	X-ray	Difference	Difference/σ
Ni2	x	0.17271(12)	0.17272(3)	0.00001(13)	0.1
	y	0.11854(9)	0.11837(3)	-0.000168(96)	1.8
	z	-0.06063(13)	-0.06020(6)	0.00043(14)	3.0
Ni3	x	0.19657(19)	0.19610(4)	-0.00048(19)	2.5
	y	0.24815(13)	0.24800(5)	-0.00015(14)	1.1
	z	0.25	0.25	0	0
Ni4	x	0.31701(20)	0.31809(4)	0.00107(21)	5.2
	y	0.00245(15)	0.00287(5)	0.00042(15)	2.7
	z	-0.25	-0.25	0	0
Ni5	x	0	0	0	0
	y	0	0	0	0
	z	0	0	0	0
Ni6	x	0	0	0	0
	y	0.23312(13)	0.23414(5)	0.00102(14)	7.5
	z	0.06265(20)	0.06170(8)	-0.00095(22)	4.4
Ni8	x	0.5	0.5	0	0
	y	-0.11742(20)	-0.11691(6)	0.00051(21)	2.4
	z	-0.25	-0.25	0	0
Si1	x	0.11893(31)	0.11881(9)	-0.00013(32)	0.4
	y	0.05806(21)	0.05784(10)	-0.00022(23)	1.0
	z	0.25	0.25	0	0
Si2	x	0.34971(24)	0.34863(7)	-0.00107(25)	4.4
	y	-0.15769(16)	-0.15804(8)	-0.00036(17)	2.0
	z	-0.04126(25)	-0.04141(12)	-0.00016(28)	0.6
Si4	x	0	0	0	0
	y	0.15655(31)	0.15635(14)	-0.00020(35)	0.6
	z	-0.25	-0.25	0	0
Si5	x	0	0	0	0
	y	0.40741(33)	0.40773(15)	0.00032(36)	0.9
	z	0.25	0.25	0	0

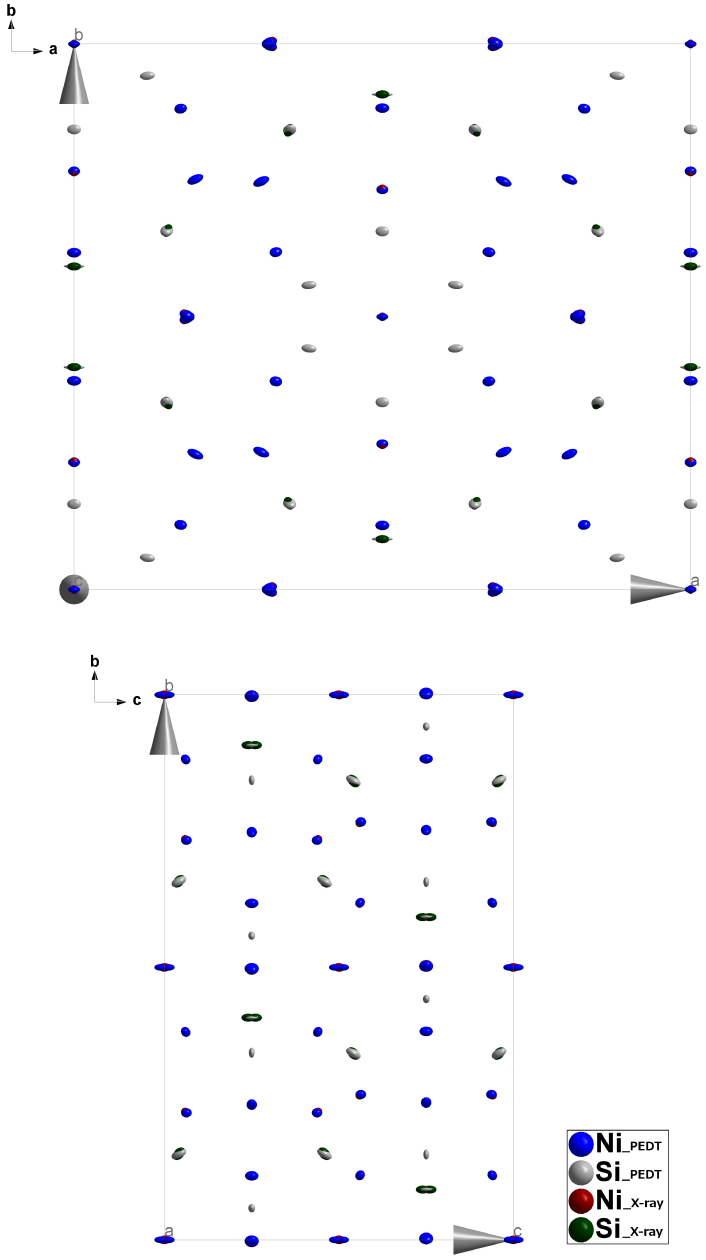

Figure 2.8: Models from the PEDT (dynamical refinement) and SCXRD superposed. Atoms in blue and gray are from PEDT model, and atoms in red and green are from the SCRXD model. The image was generated with the software for crystal structure visualization Diamond [66] and only pairs of atoms with difference in atomic positions higher than 0.01 Å are visible as displaced from each other (two collors). For difference lower than 0.01 Å, atoms from the model obtained by PEDT are shown. The ellipsoid model has 30 % of probability.

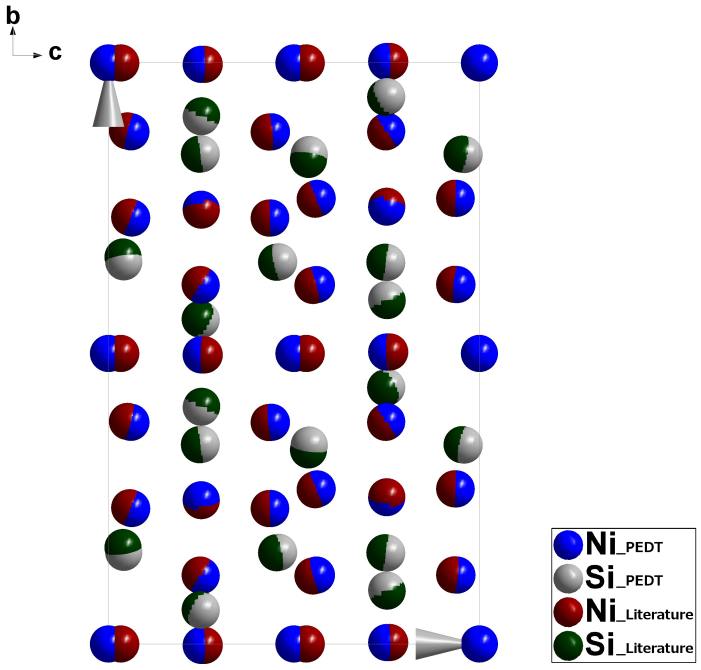

Figure 2.9: Superposition of the models from PEDT $Cmc2_1$ (blue and gray), obtained by the transformation of the model $Cmcm$ with dynamical refinement (without refinement after the transformation), and $Cmc2_1$ by Pilström [63] (red and green). The model by Pilström was shifted by -0.03323 along **c** (the average shift between the two models), in order to have the best overlap between the models.

3. Incommensurately modulated structures of $Cu_{3+x}Si$

Following the development of the dynamical refinement, we aimed to apply it for an unknown structure. Several single crystals of $Cu_{3+x}Si$ were measured by precession electron diffraction tomography. A complex incommensurately modulation was observed, containing a large number of independent atoms. However, the dynamical refinement is not completely developed for aperiodic structures and the supercell approximation with a high number of independent atoms would take a very long time to perform the dynamical refinement, according to the tests performed with the dynamical refinement [43]. Hence, the dynamical refinement was not an available option to refine the model using neither the superspace formalism nor the supercell approximation. Therefore, single crystal X-ray diffraction was measured as a function of temperature (see section 3.4.1). In order to identify which phases were present at which temperature ranges, a temperature dependent PXRD was also measured (see section 3.4.6). In this chapter we will present two of the incommensurately modulated structures of $Cu_{3+x}Si$ and the powder indexing of the phases observed at higher temperatures.

3.1 Modulated structures

According to T. Jansen, aperiodic crystals have been observed since 1960 [67, p. 2]. One group of aperiodic crystals are the so called modulated structures [68, p. 5].

Periodic crystals are described by the translation of the basic unit cell in space, in which the atoms occupy positions that are uniquely described in terms of relative coordinates in relation to the unit cell. A modulation might be interpreted as a perturbation of one or more of the atomic parameters (position, thermal displacement, site occupancy) in relation to the periodic crystal. The difference between a periodic and an aperiodic crystal is observed on their diffraction patterns.

The diffraction pattern of a periodic crystal can be completely indexed using a linear combination of three independent vectors $(\mathbf{a}_1^*, \mathbf{a}_2^*, \mathbf{a}_3^*)$

$$\mathbf{H} = \sum_{i=1}^{3} h_i \mathbf{a}_i^*, \tag{3.1}$$

where h_i are integer reflection indices. Here, the reciprocal lattice vectors $\mathbf{a}_i^*$ are related to the direct lattice vectors $\mathbf{a}_i$ by

$$\mathbf{a}_i^* . \mathbf{a}_j = \delta_{ij}(i,j) \quad i,j = 1,2,3. \tag{3.2}$$

An aperiodic crystal exhibits a more complex diffraction pattern, presenting main reflections on the nodes of the reciprocal lattice (Fig. 3.1 (a)) and satellite reflections orbiting the main ones (Fig. 3.1 (b)).

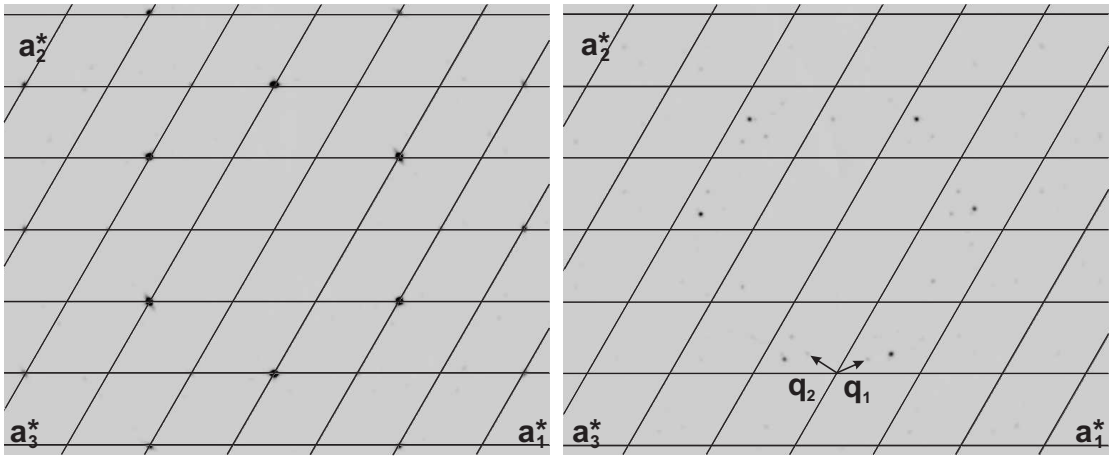

Figure 3.1: Diffraction pattern of a (3+2)-dimensional incommensurately modulated structure. (a) The main reflections indexed by the three vectors $(\mathbf{a}_1^*, \mathbf{a}_2^*, \mathbf{a}_3^*)$ of the basic unit cell, $\mathbf{a}_3^*$ pointing out of the plane , and (b) the satellite reflections, which cannot be indexed by the vectors defining the basic unit cell, are indexed by the modulation vectors $m_1\mathbf{q}_1$ and $m_2\mathbf{q}_2$. Here, the maximum value of m_1 and m_2 is 1, which means that only first order satellites are observed.

The complete diffraction pattern of an aperiodic crystal needs more than three vectors to be described (Fig. 3.1 (b)) and the superspace formalism is used, which elegantly restores the translational symmetry of modulated structures [69, 70, 71, 72] (Fig. 3.3)

$$\mathbf{H} = \sum_{i=1}^{3} h_i \mathbf{a}_i^* + \sum_{j=1}^{d} m_j \mathbf{q}_j = \sum_{i=1}^{n} h_i \mathbf{a}_i^*;\ n > 3;\ \mathbf{h}_i \text{ integers [36, p. 908]}. \tag{3.3}$$

Here, $\mathbf{q}_j = \sum_{i=1}^{3} \alpha_{ji} \mathbf{a}_i^*$ is the modulation vector used for indexing the satellites (Fig. 3.1 (c)) and m_j is the order of the satellites. If all α_{ji} are rational numbers, the modulation vector has the components as a rational multiple of the reciprocal basic unit cell and the structure is commensurately modulated. If at least one of the α_{ji} is an irrational number, the structure is called incommensurately modulated [73]. The order of the satellites for the trigonal system is defined by the concept

of concentric stars from applied group theory. One star, or one order of satellites, is defined by satellites within the same distance to the main reflection and which are related by symmetry. Satellites belonging to one order form one star around the main reflection (Fig. 3.2). The higher the order of the satellites, the weaker intensities they have. If $m = 0$, only the main reflections are present, which is the non-modulated case.

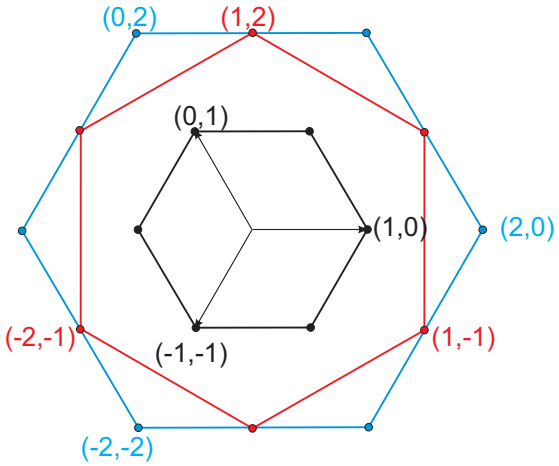

Figure 3.2: The concept of "star" to describe the order of satellites in trigonal system for (3+2)D modulated structures. Satellites related by symmetry and withing the same distance from the main reflection form one star and are grouped in the same order of satellite.

The reciprocal lattice in the periodic (3+d) dimensional superspace is defined as a function of the reciprocal lattice in the three-dimensional space and the vectors $\mathbf{b}_j^*$ of the superspace, which are perpendicular to the real three-dimensional space ($\mathbf{R}^*$) as [68, p. 28]

$$\begin{cases} \mathbf{A}_i^* = \mathbf{a}_i^* & i = 1, 2, 3 \\ \\ \mathbf{A}_{3+j}^* = \mathbf{b}_j^* + \mathbf{q}_j & j = 1, \ldots, d. \end{cases} \tag{3.4}$$

Since the higher dimensions have no physical meaning, $\mathbf{b}_j^*$ can be defined as an unitary vector. The angle between the vectors $\mathbf{b}_j^*$ depends on the modulation vectors and thus $\mathbf{b}_j^*$s are not necessarily orthogonal between them (for $d \geq 2$). The angle between the axes $\mathbf{A}_i^*$s can be obtained by replacing the components $\mathbf{A}_i^*$s in function of the three-dimensional space and the vectors $\mathbf{b}_j^*$ of the superspace in the metric tensor $\mathbf{G}$ in the superspace. The reciprocal metric tensor is shown below for a (3+2) dimensions:

$$\mathbf{G}^*_{5,5} = \begin{pmatrix} \mathbf{A}^*_1.\mathbf{A}^*_1 & \mathbf{A}^*_1.\mathbf{A}^*_2 & \mathbf{A}^*_1.\mathbf{A}^*_3 & \mathbf{A}^*_1.\mathbf{A}^*_4 & \mathbf{A}^*_1.\mathbf{A}^*_5 \\ \mathbf{A}^*_2.\mathbf{A}^*_1 & \mathbf{A}^*_2.\mathbf{A}^*_2 & \mathbf{A}^*_2.\mathbf{A}^*_3 & \mathbf{A}^*_2.\mathbf{A}^*_4 & \mathbf{A}^*_2.\mathbf{A}^*_5 \\ \mathbf{A}^*_3.\mathbf{A}^*_1 & \mathbf{A}^*_3.\mathbf{A}^*_2 & \mathbf{A}^*_3.\mathbf{A}^*_3 & \mathbf{A}^*_3.\mathbf{A}^*_4 & \mathbf{A}^*_3.\mathbf{A}^*_5 \\ \mathbf{A}^*_4.\mathbf{A}^*_1 & \mathbf{A}^*_4.\mathbf{A}^*_2 & \mathbf{A}^*_4.\mathbf{A}^*_3 & \mathbf{A}^*_4.\mathbf{A}^*_4 & \mathbf{A}^*_4.\mathbf{A}^*_5 \\ \mathbf{A}^*_5.\mathbf{A}^*_1 & \mathbf{A}^*_5.\mathbf{A}^*_2 & \mathbf{A}^*_5.\mathbf{A}^*_3 & \mathbf{A}^*_5.\mathbf{A}^*_4 & \mathbf{A}^*_5.\mathbf{A}^*_5 \end{pmatrix}. \tag{3.5}$$

Analogously to the three-dimensional case, the relation between the reciprocal and the direct lattice vectors is given by

$$\mathbf{A}^*_i.\mathbf{A}_j = \delta_{ij}(i,j) \quad i,j = 1,\ldots,d. \tag{3.6}$$

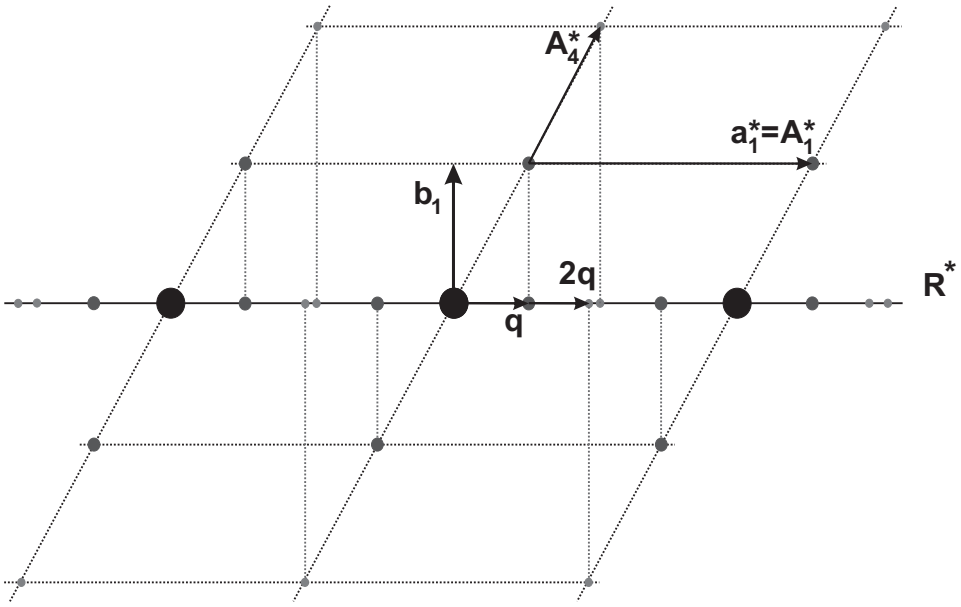

Figure 3.3: Indexed diffraction pattern (along the black line) of a hypothetical (3+1)D modulated structure. The recovery of the translational periodicity is obtained by using the superspace (shown in dotted lines). The satellite reflections in the reciprocal three-dimensional space ($\mathbf{R}^*$) are the projections of the reflections along $\mathbf{b}^*_1$. $\mathbf{A}^*_1$ is given by the sum of $\mathbf{b}_1$ and the modulation vector $\mathbf{q}$ (Eq. 3.4). The sattelites are shown up to second order ($m = 2$).

Since the use of the superspace formalism recovers the translational symmetry of the structure, symmetry operations can be used in a generalized form in the superspace, allowing one to define the superspace groups and use all the crystallographic procedures available for the three-dimensional crystal structure determination.

An alternative to the superspace is the supercell approximation, when α_{ji} is approximated by a rational value $\alpha_{ji} = \frac{p_{ji}}{s_i}$, where p_{ji} and s_i are integers, and an unit cell is chosen with dimensions so that the components of the rational $\mathbf{q}$ are integers. The (3+d)-dimensional indexing of the diffraction pattern is thus transformed to

$$\mathbf{H} = \sum_{i=1}^{3} \mathbf{a}_i^* \sum_{j=1}^{d} (s_i h_i + p_{ji} m_j), \tag{3.7}$$

and the supercell in the real space is given by

$$\mathbf{a}_i^{sc} = \sum_{i=1}^{3} \mathbf{a}_i s_i. \tag{3.8}$$

Since the supercell is a three-dimensional standard unit cell, the methodology used for periodic crystals is used normally.

3.2 The system $Cu_{3+x}Si$

Copper silicides are used as contact between copper conductors and silicon and as interconnect in electronic devices [74, 75]. The use of copper enhances the electrical properties of semiconductors and enables the decreased dimensions of circuitry [47, p. 35]. However, the diffusion of copper in silicon develops higher resistivity and it was found to be a dominant problem, requiring the use of diffusion barriers [76]. Aiming to better understand and improve the reactions and properties of copper silicides, a large number of studies on physical and chemical properties and on the growth behavior has been reported [77, 78, 79].

The binary phase diagram Cu-Si (Fig. 3.4 (a)) has been investigated for some decades [80, 81, 82] and it is accepted as well established. The low temperature region of the phase diagram has three stable phases, according to Olesinski [80]: η'', ϵ and γ. η'' is the phase present within 75.5 – 76.5 at % Cu, and its composition can be written as $Cu_{3+x}Si$. η'' transforms to η' and η with increasing temperature. The transitions between these $Cu_{3+x}Si$ phases depend on the composition, following from η'' to η' at 467 °C and 570 °C, and from η' to η at 558 °C and 620 °C, for the silicon- and copper-richest sides, respectively. The congruent melt occurs at 859 °C. These phase compositions were assigned as being 1 at. % Si richer by Sufryd *et al.* [81], while the computed model of the phase diagrams by W. Gierlotka and M. A. Haque [83] and by Hallstedt *et al.* [84] present the three phases as line field compounds with a different composition of 0.5 at % Cu (Fig. 3.4 (b)). These computed phase diagrams contain a coexistence of two phases for a range of

temperature: η'' with η' from around 476 °C to 549 °C, and η' with η from around 558 °C to 615 °C.

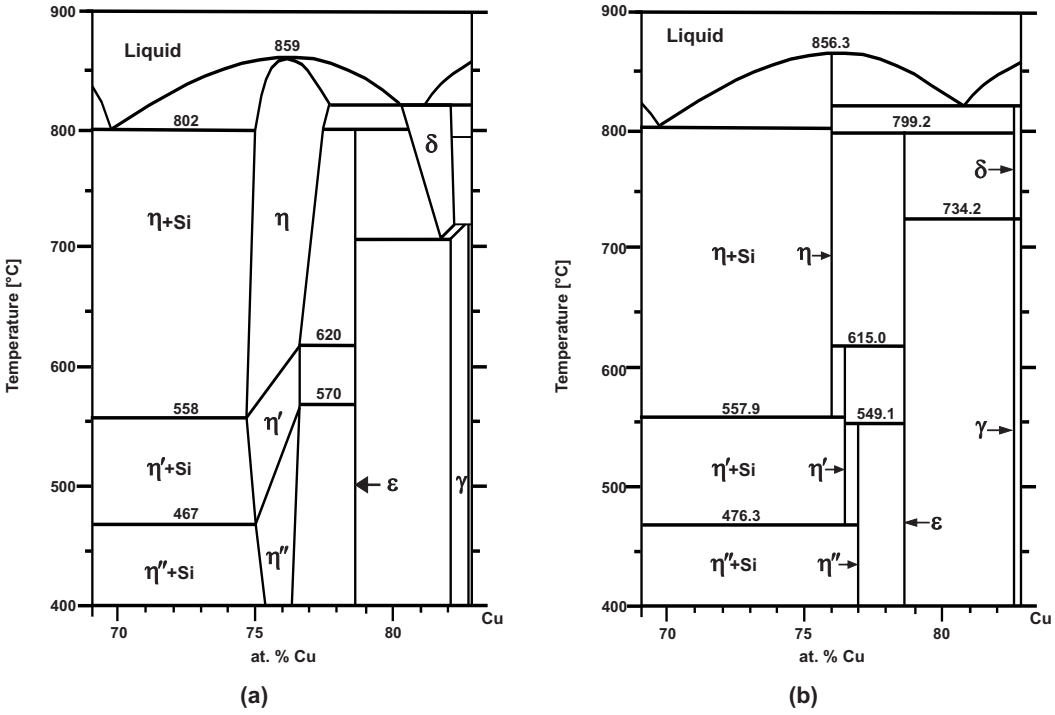

Figure 3.4: Cu-Si phase diagram in the vicinity of $Cu_{3+x}Si$ according to (a) R. W. Olesinski and G. J. Abbaschian [80]. (b) Computed model of the Cu-Si phase diagram, by according to W. Gierlotka and M. A. Haque [83] and by Hallstedt *et al.* [84].

There were several attempts to obtain the crystal structure of the three polymorphs of $Cu_{3+x}Si$ [85, 86, 26], but there are still considerable uncertainties concerning these structures.

The first attempt was done by J. K. Solberg [85], who performed electron diffraction analysis of oriented patterns on a Czochralski-grown crystal of $Cu_{3+x}Si$ precipitates in a Si matrix. Solberg [85] interpreted η as a disordered b.c.c model, space group $R\bar{3}m$ with $a = 2.47$ Å, α=109.74°, with composition Cu_3Si. η' was interpreted as an ordered superstructure of η, space group $R3$ with $a = 4.72$ Å, α=95.7°. η'' was interpreted as a long-period superlattice of η', unit cell parameters $a = 76.76$ Å, $b = 7.00$ Å, $c = 21.94$ Å, $\alpha = \beta = \gamma = 90°$. The observed diffraction pattern of η'' was complex and it could only be indexed with three twins related by rotation of 120° around $[001]^*_{\eta''}$.

This model was refuted in 2007, when Mattern *et al.* [87] and C. Wen and F. Spaepen [86] independently proposed a new model for the structure of the η

phase. The new η model has trigonal unit cell, lattice parameters $a \approx 4.1$ Å and $c \approx 7.3$ Å, and space group symmetry $P\bar{3}m1$. Mattern *et al.* [87] performed powder diffraction on quenched samples, while Wen and Spaepen [86] investigated a thin film consisting of precipitated nanocrystals smaller than 50 nm in silicon crystals by high-temperature electron diffraction. Their trigonal model indicates the composition Cu_7Si_2, which differs from the true composition ($Cu_{76}Si_{24}$). The composition mismatch was assumed to originate from the presence of vacancies or mixed occupancy of some sites in the structure. The electron diffraction patterns presented satellite reflections, which were interpreted as the result of chemical ordering between the vacancies and the Cu and Si atoms. The observed phases were identified as η' and η, and the low temperature η'' was not observed.

Comparing the models from Solberg [85] represented in the hexagonal settings ($a = 4.04$ Å, $c = 2.44$ Å) with the one by Mattern *et al.* [87] and Wen and Spaepen [86] ($a \approx 4.1$ Å $c \approx 7.3$ Å) the difference between these η models is that η by Solberg [85] has shorter c axis than that by Mattern *et al.* [87] and Wen and Spaepen [86]. The atomic positions and composition are also different.

The only structure determined so far is that of η' phase, which was elucidated by Palatinus *et al.* [26] using electron diffraction tomography data of a Cu_{3+x}(Si,Ge) nanoplatelets. It was shown that the unit cell found by Mattern *et al.* [87] and C. Wen and F. Spaepen [86] is in fact the basic unit cell of an incommensurately modulated structure. The model by Palatinus *et al.* [26] described in the trigonal unit cell $a = 4.1084$ Å, $c = 7.05$ Å has basic space group $P\bar{3}1m$ with two modulation vectors: $q_1 = (\alpha, \alpha, 1/3)$ and $q_2 = (-2\alpha, \alpha, 1/3)$, $\alpha \approx 0.25$, instead of the space group $P\bar{3}m1$ suggested by Mattern *et al.* [87] and C. Wen and F. Spaepen [86]. This model of η' by Palatinus *et al.* has equivalent **c** axis to that from Solberg [85], but different atomic positions and composition when compared to the models by Mattern *et al.* [87] and Wen and Spaepen [86]. The structure by Palatinus *et al.* contains six layers from which four are symmetry independent. It is similar to η'' presented here (see section 3.4.3), with the same distribution of clusters on the modulated layer, but with half the length of the **c** axis of η'' due to the disordered D layer [88]. The modulation of η' by Palatinus *et al.* [26] was found to be a complicated positional modulation of one Cu layer, and not the chemical ordering of Cu and Si atoms, as indicated previously by Mattern *et al.* [87] and C. Wen and F. Spaepen [86]. So far, η and η'' remain essentially unknown.

3.3 Experimental

3.3.1 Sample preparation

Ingots of $Cu_{3+x}Si$ of nominal composition $Cu_{74}Si_{26}$, $Cu_{76}Si_{24}$ and $Cu_{78}Si_{22}$ (hereafter called sample Cu74, Cu76 and Cu78, respectively) were prepared from pure elements (purity 99.99 %) by arc melting under argon atmosphere in Edmund-Bühler MAM-1 furnace. Samples were annealed during 24 hours in a tube furnace at 650 °C and slowly cooled to room temperature within 6 hours under argon atmosphere to ensure homogenization.

3.3.2 Energy dispersive X-ray spectroscopy

Energy dispersive X-ray spectroscopy (EDS) was used to verify the chemical composition of the samples. EDS is performed in a scanning electron microscope, where the voltage is used so that the incident electron beam provides enough energy to excite an electron sitting in an inner shell of the atom, which was initially in the ground state. The excited electron is ejected, leaving an electron hole on the inner shell. An electron from a higher energy shell might thus transition to the lower-energy shell, filling the electron hole and emitting the difference of energy as radiation. Since the difference of energy between the shells depends on the element, the emitted radiation will be characteristic for the element. The released characteristic X-ray can be measured by an energy-dispersive spectrometer, allowing to identify the chemical composition of the sample [89, p.185].

A microscope Tescan FERA 3 with EDAX Octane 80 mm^2 detector was used to verify the composition of the bulk samples.

3.3.3 Temperature-dependent single crystal X-ray diffraction

Sample Cu76 was the one selected for the temperature-dependent single crystal X-ray diffraction (TD-SCXRD), because it is in the center of the stability field of $Cu_{3+x}Si$. A single crystal was selected from the crushed bulk sample. The SCXRD was performed in a KappaCCD (Bruker-Nonius) four-circle diffractometer equipped with an Apex2 CCD detector, using Mo Kα radiation produced with a microfocus Incoatec IμS sealed X-ray tube. The Cyberstar gas blower system was used for the high-temperature data collections. The measurement was performed as a function of the temperature. For that, the crystal was mounted inside a quartz capillary, with a quartz needle fixing the crystal position to prevent movements during the heating. The sample-detector distance used was 60 mm to decrease the obstruction near the sample due to the gas blower apparatus. To avoid collisions

or a direct contact of the gas flow with the detector, the position of the detector was fixed to 2θ=-30°, away from the path of the gas flow. This fixed position leads to the observation of reflections up to $2\theta_{\max}$=60.5°. Each data collection comprised 3 large ϕ scans of 360° for 3 different χ values (-30°, 0°, 60°) and ω=-60°. The frame angle and the exposure time have been set to 0.5° and 10 s/°. The measurement was performed starting from room temperature, then heating to the desired temperature with heat rate of 5 °C/min, the sample temperature was homogenized during 30 minutes, and finally the data collection was performed at temperatures which were expected to belong to each phase within the phase-field $Cu_{3+x}Si$. A finer sampling was performed in the high-temperature field. The temperatures were: 120 °C, 320 °C, 470 °C, 520 °C, 570 °C, 620 °C, and 720 °C.

3.3.4 Temperature-dependent powder X-ray diffraction

Differently from the single crystal measurements, the composition of the samples for the temperature-dependent powder X-ray diffraction (TD-PXRD) measurement were selected to lie outside the stability region of $Cu_{3+x}Si$. The reason is that $Cu_{3+x}Si$ should be in equilibrium with the neighboring phases in the phase diagram, which could be used as reference to observe the unit cell expansion with increasing temperature. The neighboring phases are Si for the sample Cu74 and ϵ for the Cu78. Bulk samples were crashed, ground and sieved with a 50 μm net. TD-PXRD was performed in collaboration with Morgane Poupon on a Rigaku Smartlab in Bragg-Brentano geometry using Cu $K\alpha$ radiation (λ = 1.54051 Å), germanium Johansson monochromator, and detector D/teX Ultra 250. A high temperature chamber Anton-Paar HTK 1200N was used to heat the sample. The scan range was from 2θ = 15° to 2θ = 110° with speed of 1°/min. The heating rate was 5 °C/min under vacuum. Scans were performed at every 30 °C, from 30 °C to 700 °C, with a more detailed analysis within 480 °C and 525 °C on sample Cu74, where steps of 5 °C were used, instead. Two cycles of heating and cooling were performed to verify the reversibility of the transitions.

Powder patterns were indexed and fitted using a combination of manual background and 15 terms of Legendre polynomials. The fitting was performed using le Bail algorithm with pseudo-Voigt profile. Two steps were used for the profile fitting. In the first step, the main reflections were indexed using the cyclic refinement available in Jana2006. In the approach, the refined parameters of the first pattern are used as the initial values for the refinement of the next pattern. This procedure continues until the last pattern. In the second step of the refinement, each of these patterns resulting from the cyclic refinement was analyzed individually, when the modulation vectors were included in the refinement.

For the refinement of the sample Cu74, the Si peaks were initially refined separately in order to verify the expansion of the unit cell and the calibration of

the equipment. The Si peaks present in the sample Cu74 were much weaker than those of the $Cu_{3+x}Si$ phase and did not change intensity within the whole data collection. Hence, they were not included in the le Bail fit of the $Cu_{3+x}Si$ phases. Instead, these Si peaks were excluded from the diffractogram, being neglected during the indexing and refinement processes.

On the other hand, the sample Cu78 contains an expressive amount of the ϵ phase. Hence, it was refined together with the $Cu_{3+x}Si$ phases for all the temperature-dependent patterns. The ϵ phase was indexed using the model by F. R. Morral and A. Westgren [90], available on the Inorganic Crystal Structure Database (ICSD) [91].

3.4 Results and discussion

3.4.1 Crystal structures

Two structures were solved with the data from TD-SCXRD. Both are incommensurately modulated, with two modulation vectors and almost identical average structures. The first one is the phase stable at room temperature and it was observed for the first time during the development of this thesis. It was named η''' phase, following the naming of the phase diagram. η''' was observed in the data sets measured at 120 °C and 320 °C. The second structure solved is η'', which was observed in all the data sets measured above 470 °C. Surprisingly, no phase transformation to η' phase was observed up to the highest measured temperature (720 °C). The structure analysis of the η''' and η'' phases revealed a close relationship to the phase η' [26].

3.4.2 Average structure

η''' and η'' have similar average crystal structures and only that of η''' will be described here. The data was measured at 120 °C, and only the main reflections were imported to Jana2006 for the solution of the average structure, which was performed by Superflip [45]. The crystal structure was refined in Jana2006. Details concerning the refinement of the average structure are summarized in Table 3.1. The main reflections could be indexed in a hexagonal unit cell with parameters $a = 4.0700(3)$ Å, $c = 14.6848(7)$ Å and it can be described in the space group $P6_3/mmc$. The complete diffraction pattern, including the satellites, presents point group $\overline{3}$. Neglected information from the satellites during the solution is known to create uncertainties in the whole model [92]. Indeed, a strong modulation is exhibited in the average structure by large anisotropic displacement parameters. Nevertheless, the refinement of the average structure yielded a relatively

low residue value, R_1(obs)=5.13 %.

The average structure has twelve stacked layers along [001], from which four are symmetrically independent (Fig. 3.5): one hexagonal layer with one Si atom per unit cell (layer A), one layer with two Cu atoms per unit cell disposed in honeycomb geometry, which is the most strongly modulated one (layer B), one hexagonal layer with one Cu atom per unit cell (layer C) and one honeycomb layer with regularly alternating Cu and Si atoms (layer D). The atomic alternation of Cu and Si on the honeycomb layer D is clearly observed on the Fourier map (Fig. 3.6(a)), while the Fourier maps from layers A and C show densities indicating either only Si or Cu (Fig. 3.6(b)). The strong modulation of the layer B is demonstrated in the average structure by very anisotropic distribution of electron density around the average position of the Cu atoms in the layer (Fig. 3.7). This density arising from the modulation was modeled by splitting of the two Cu atoms (Fig. 3.7) with freely refined occupancies. The refinement yielded the total composition of $Cu_{76.74}Si_{23.26}$, which is close to the nominal composition during the sample preparation $Cu_{76}Si_{24}$.

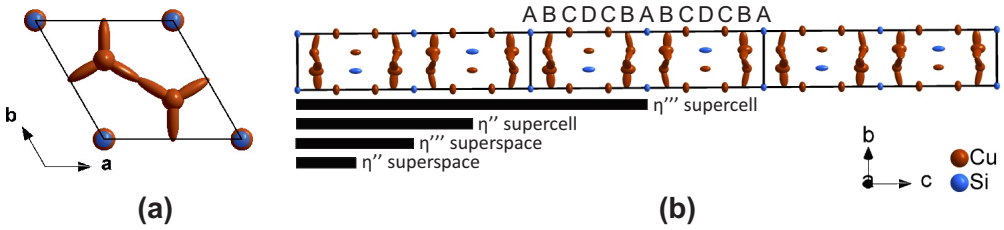

Figure 3.5: The average structure of η'' and η'''. (a) The average structure of η''' viewed along **c** and (b) three unit cells of the average structure viewed along **a**, corresponding to one unit cell of the supercell approximation. Letters A to D label different layer types. Bars with labels η''-superspace, η'''-superspace, η''-supercell, and η'''-supercell outline the symmetry independent parts of the structure for each model.

3.4.3 Modulated structure of η''-$Cu_{3+x}Si$

The structure of η'' proved to be less complex than that of η'''. Hence, η'' will be described first and will be used as a reference to verify the correctness of η'''.

η'' was identified in all the data collections above 470 °C. This measurement collected at 470 °C was used for the structure solution of this phase. The complete diffraction pattern could be indexed in a trigonal unit cell a=4.0612(4) Å and c=14.672(2) Å with two modulation vectors $q_1 = (\alpha, \alpha, 1/3)$ and $q_2 = (-2\alpha, \alpha, 1/3)$, $\alpha = 0.2509(10)$ in a (3+2)-dimensional indexing. Since α is equal to 1/4 within its experimental accuracy, one might consider to round its value

Table 3.1: Crystallographic data on the refinement of average structure of η'''-$Cu_{3+x}Si$.

Chemical formula	$Cu_{3.30}Si$
Crystal system, space group	Hexagonal, $P6_3/mmc$ No. 194
a, c (Å)	4.0700(3), 14.6848(7)
V (Å^3)	210.66(2)
Z	4
Density (g·cm^{-3})	7.4934
Data collection	
Diffractometer	KappaCCD (Bruker-Nonius), Incoatec IμS
λ (Å) (Mo Kα)	0.71073
Data collection method	ϕ scans
θ_{min}, θ_{max}	4.16, 29.12
Rint(obs/all) (%)	1.35/1.73
Completeness (%), θ_{full} (°)	99.5, 29.12
h_{min} h_{max} k_{min} k_{max} l_{min} l_{max}	-5 5 -5 5 -20 19
Temperature (°C)	120
Specimen size (mm^3)	$0.088 \times 0.126 \times 0.157$
Crystal form, colour	irregular, metallic grey
μ (mm^{-1})	33.035
T_{min}, T_{max}	0.420, 0.746
No. of measured main reflections	1956
No. of independent reflections	393
No. of observed main reflections	273
Condition for observed reflections	$I > 3\sigma(I)$
Refinement	F
Weighting	$w = (\sigma^2(F) + 0.0001F^2)^{-1}$
R_1, wR, GOF (obs/all) (%)	5.13/7.37, 5.52/5.74, 3.10/2.64
No. of parameters refined	30
$\Delta\rho_{max}$, $\Delta\rho_{min}$ (e·Å^{-3})	0.72 -1.08

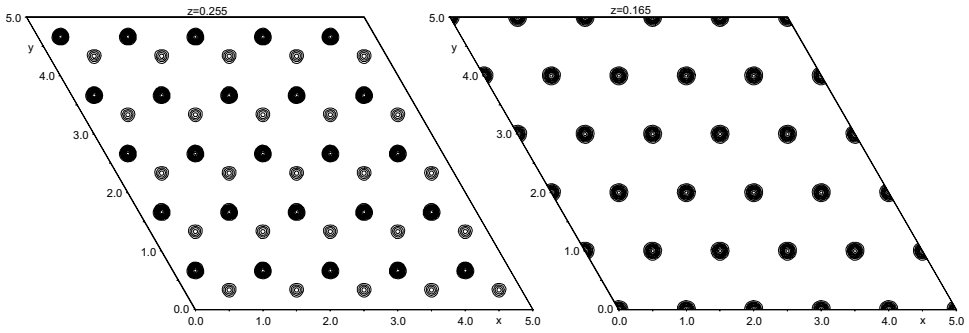

Figure 3.6: (a) Fourier map of the honeycomb layer D showing alternating Cu and Si densities, while (b) shows the layer C, containing Cu densities, only.

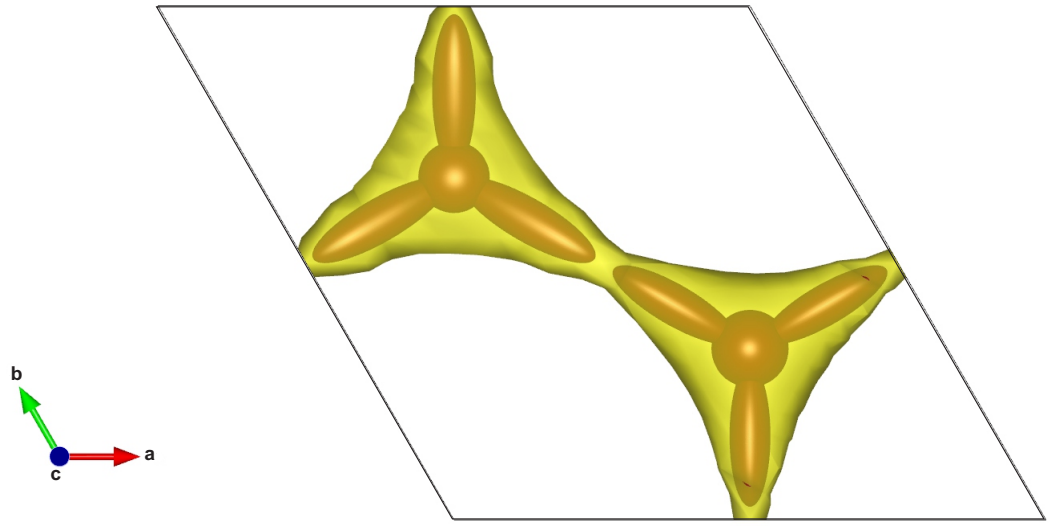

Figure 3.7: View along **c** of the electron density in layer B of the average structure of η'''-$Cu_{3+x}Si$ (yellow isosurface, level 7 e/Å^3). The spheres are the average positions of Cu atoms, the red elongated ellipsoids are additional copper atoms refined to model the distribution of the copper atoms in the unit cell due to the strong modulation of this layer. Atoms have partial occupancies, ellipsoids shown at 50 % probability level.

and the modulation would be commensurate. However, our results on powder diffraction investigation (see section 3.4.7) unquestionably showed that α value varies as a function of temperature and, in fact, it does not converge to a commensurate value. Therefore, the structure should be considered incommensurately modulated.

Using the concept of stars for the order of satellites (Section 3.1), only first order satellites of the type $hkl10$ and satellites with mixed indices $hkl\bar{1}1$ (and the symmetry equivalent ones) were considered as observed, with sufficiently strong intensities ($I > 3\sigma$) to be used in the structure solution and refinement procedures. Less than 4 % of the second order satellites of the type $hkl20$ had $I > 3\sigma$. The symmetry of the pattern and the systematic absences indicated the space group $P\bar{3}1c(\alpha, \alpha, 1/3)(-2\alpha, \alpha, 1/3)$ or its non-centrosymmetric subgroup. The structure was solved using the superspace formalism by Superflip in (3+2)-dimensions, which confirmed the space group $\mathrm{P}\bar{3}1c(\alpha, \alpha, 1/3)(-2\alpha, \alpha, 1/3)$.

The solution in the superspace had the electron density map with most atoms well defined. An investigation of the layers shows that the strongest modulated layers (layers B) have the modulation with an amplitude comparable to the size of the unit cell. In one of the B-type layers there is a ring of electron density around positions (0,0,z) (Fig. 3.8). These rings correspond to a discontinuity in the modulation function and a small shift of the phases t and u of the modulation leads to the transformation of the ring of density into a pentagon. All the six orientations of the pentagon are simultaneously present in the point $t = 0$, $u = 0$, in agreement with the 6-fold symmetry of the superspace axis $\mathbf{A}_3^*$ with the axes $\mathbf{A}_4^*$ and $\mathbf{A}_5^*$.

Fig. 3.9 shows the density of the modulated layer B (at x_3 from 0.13 to 0.15) constructed by projecting the coordinate x_1 between 0 and 0.98 and plotting the coordinate x_2 as a function of the coordinates x_4 and x_5 of the superspace. This construction of the layer B shows that the amplitude of the modulation sweeps the whole unit cell, and that the modulation contains not only discontinuities, but also windows.

The only crystallographic software dealing with modulated structures in (3+2)-dimensions is Jana2006 [93], which offers harmonic and discontinuous functions (Crenel, saw-tooth and zig-zag) for the description of the electron density of modulated structures. In our case, the complexity of this modulation and the small number of observed reflections make this density impossible to be parametrized with a combination of the available functions, so that it could be refined using the superspace formalism. Consequently, the only viable way to describe the structure is to use a supercell approximation.

Given that α is roughly 1/4, a supercell approximation can be used with a $4 \times 4 \times 3$ supercell. The supercell approximation was performed in an alternative way: The solution was performed using the superspace formalism and the components of the modulation vectors were rounded to the smallest possible commensurate value, giving a commensurate modulated model. The solution in the superspace was saved and used in two ways. In the first one, the Fourier map of this commensurate modulated model was calculated with the intended supercell dimensions (x_1 and

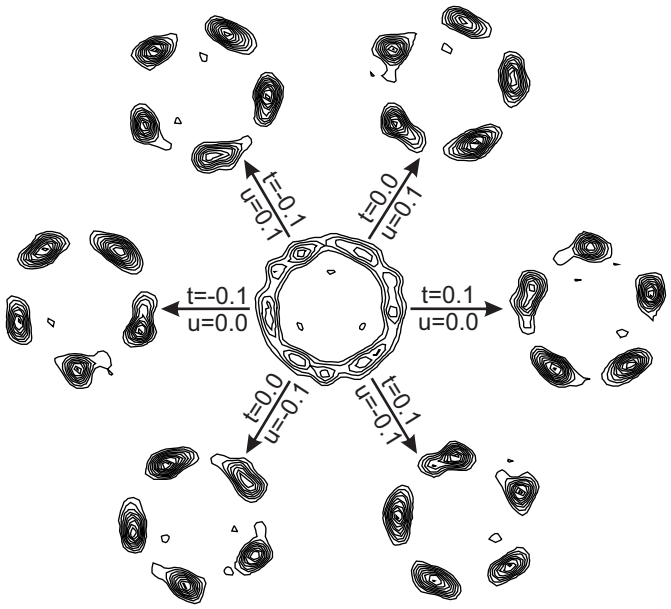

Figure 3.8: (a) Electron density in the vicinity of the point (0,0,0.14) in the superspace electron density of η''. The continuous ring of density at $t = 0$, $u = 0$ (central panel) is a superposition of six pentagons at various orientations. The pentagons are resolved at t,u-sections slightly shifted from 0 (six panels surrounding the central panel).

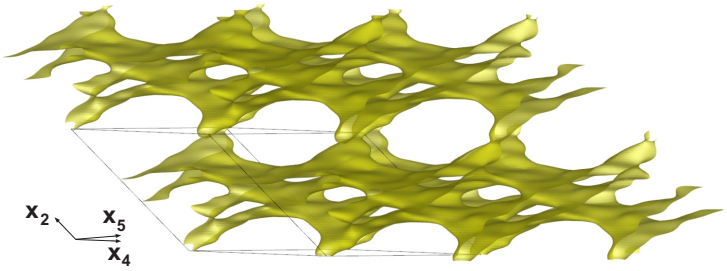

Figure 3.9: View of the density of the modulated layer B of η''. The surface shows the density along the coordinate x_2 as a function of the coordinates x_4 and x_5. The 5D superspace density was projected along x_1 in the interval from 0 to 0.98 and along x_3 from 0.13 to 0.15 to obtain a three-dimensional representation of the extremely complex modulation function of atoms in layer B.

x_2 from 0 to 3.98 in steps of 0.02), and this Fourier map was interpreted by the program Electron Density Map Analysis (EDMA) [94] to find the positions of these atomic densities of the Fourier map. EDMA uses a discrete electron density map as input and extracts topological properties of the electron density as a function of the

space coordinates. In the second version, the commensurate approximated model was transformed to a supercell in the standard way. The supercell approximation is performed by transforming the (3+2)D reflection indices to the 3D supercell description using the relationships $h_{sc} = 4h + m - 2n$,$k_{sc} = 4k + m + n$,$l_{sc} = 3l + m + n$. The space group of the supercell becomes $P\bar{3}1c$. The model with the atomic positions from the Fourier map in the superspace formalism interpreted by EDMA was imported to Jana2006.

The commensurate approach is only an approximation and there is a misfit between the positions of the satellites and the grid of the supercell lattice. This misfit generates a deformation of the reciprocal space, from which one of the consequences is the splitting of atoms. Split atoms from the interpretation of EDMA could be identified by the occurrence of very short distances between them (typically distances smaller than 0.1 Å) and their positions were adjusted accordingly, in case of splitting around a special position.

The density of the six orientations of the pentagon which are simultaneously present in the point $t = 0$, $u = 0$ was modeled by a supersposition of six Cu_5 pentagons rotated by 30° with respect to each other (Fig. 3.8). Note, however, that this is an artifact of the supercell approximation and that in the real, incommensurately modulated structure model, this situation occurs only along one line in the whole crystal, not once per unit cell. This initial model with the atomic positions from EDMA was used for the refinement.

The model contains 81 independent atoms, giving a total of 280 refinable parameters if each atom would be refined independently. The data set contains only 624 observed reflections, which results in a very low data to refined parameter ratio. The way around it was to create two models which could be refined and compared. For both models all atoms of the same chemical species and belonging to the same layer type were restricted to have the same displacement parameter. The first model, denominated the fixed model, had all coordinates fixed to the values obtained from the solution. This fixed model had six refinable parameters, namely five isotropic displacement parameters and one overall scale factor. In the second model, the free model, the coordinates of all atoms were freely refined. The free model contains 202 refinable parameters. The free model contains 24.7 reflections per parameter when all the reflections are considered, but this ration decreases to 3.1 if only the observed reflections are counted. Details from the refinement of both models are summarized in Table 3.2.

Comparing the fixed and the free models, the average distance between equivalent atoms of both models is 0.197 Å and the maximum distance is 0.388 Å. The fixed model has higher R-value, R_1(obs)=15.03 % against 6.75 % for the free model, but the fixed model appears to be better than the free counterpart. This is clearly seen in the geometry of the honeycomb layers (Fig. 3.10), which are

Table 3.2: Refinement details for the fixed and free model of the η'' phase and of the fixed model of η'''.

phase	η''		η'''
structure model	fixed	free	fixed
Chemical formula	$Cu_{3.31}Si$		$Cu_{3.31}Si$
Superspace description			
a, c (Å)	4.0612(4), 14.6723(28)		4.0700(3), 14.6848(7)
V (Å^3)	209.57(4)		210.66(2)
modulation vector	(0.2509(10), 0.2509(10), 1/3)		(0.2783(10), 0.2068(10),1/3)
superspace group	$P\bar{3}1c(\alpha,\alpha,1/3)(-2\alpha,\alpha,1/3)$		$P\bar{3}(\alpha,\beta,1/3)(-\alpha-\beta,\alpha,1/3)$
Supercell description			
a, c (Å)	16.2448(4), 44.017(8)		56.9800(3), 44.055(2)
V (Å^3)	10060(2)		123870(6)
Z	192		2352
Calculated density (g·cm^{-3})	7.563		7.519
space group	$P\bar{3}1c$ No. 163		$P\bar{3}$ No. 147
Data collection			
Diffractometer	KappaCCD (Bruker-Nonius) with Incoatec IμS		
λ (Å)	(Mo Kα) 0.71073		
Data collection method	ϕ scans		
θ_{min}, θ_{max}	2.67, 30.39		2.03, 29.25
Resolution (Å)	0.708		0.733
Rint(obs/all) (%)	9.68/24.02		7.92/13.88
Temperature (°C)	470		120
Specimen size (mm^3)	$0.088 \times 0.126 \times 0.157$		
Crystal form, colour	irregular, grey		
μ (mm^{-1})	33.35		33.35
T_{min}, T_{max}	0.420, 0.746		0.420,0.746
No. of measured reflections	25292		25518
No. of independent reflections	4996		4920
Condition for observed reflections	$I > 3\sigma(I)$		
No. of observed reflections	624		1471
Refinement	F		
Weighting	$w = (\sigma^2(F) + 0.0001F^2)^{-1}$		
R_1 (obs/all) (%)	15.03/54.48	6.75/65.62	11.92/26.13
wR (obs/all) (%)	14.68/15.93	5.48/7.76	13.08/13.66
GOF (obs/all) (%)	6.12/2.35	2.75/1.16	5.11/2.93
No. of parameters refined	6	202	6
$\Delta\rho_{max}$, $\Delta\rho_{min}$ (e·Å^{-3})	13.76, -14.71	10.18, -10.91	12.91, -17.54

more distorted in the free model, and in the values of the interatomic distances and atomic displacement parameters. A search in the ICSD (Inorganic Crystal Structure Database) [91] for intermetallic compounds containing Cu and Si shows that hardly ever the Cu-Cu distances and the Cu-Si distances are shorter than

2.30 Å. While the fixed model has the shortest Cu-Cu and Cu-Si distances of 2.34 Å and 2.29 Å, respectively, in the free model 31 distances are shorted than 2.3 Å, the shortest ones being 2.19 Å for Cu-Cu and 2.05 Å for Cu-si.

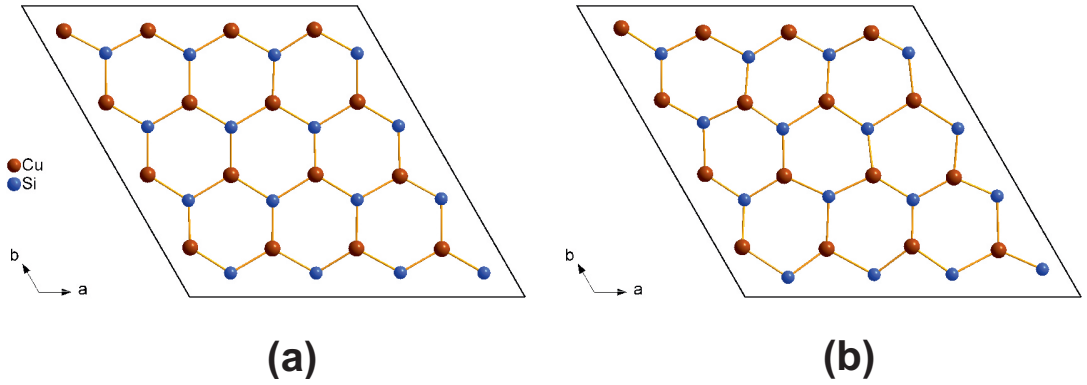

Figure 3.10: Layer D in η'' obtained from (a) the structure solution (i.e. the fixed model) and (b) refined free model. Note the regular honeycomb geometry in (a) and the apparent distortion in (b).

As for the ADPs, while the fixed model had all positive definite APDs, one of the five refined ADPs of the free model became negative.

It is reasonable to assume that the correct structure model stands in between the free and fixed models. However, the most representative model of the true structure is the fixed model, *i.e.* the model with atomic coordinates obtained directly from the structure solution. The reasons why are the more realistic interatomic bonds and atomic displacement parameters, and the less distorted honeycomb layers of the fixed model.

3.4.4 Modulated structure of η'''-$Cu_{3+x}Si$

The structure of η''' was elucidated from the data set collected at 120 °C. Like for η'', the diffraction pattern of η''' could be indexed with (3+2)-dimensional indexing in a trigonal unit cell $a = 4.0700(3)$ Å and $c = 14.685(2)$ Å. Interestingly, the unit cell of η''', which was measured at lower temperature, has larger volume than that of η'', measured at higher temperatures (η'', obtained at 470°, has a=4.0612(4) Å and c=14.672(2) Å). Note that the contraction of the unit cell volume was observed in the TD-PXRD measurements (Section 3.4.7), but not during the transition from η''' to η''. Further investigation is necessary to verify if the unit cell volume contracts during this transition. The modulation vectors for η''' were $q_1 = (\alpha, \beta, 1/3)$ and $q_2 = (-\alpha - \beta, \alpha, 1/3)$, $\alpha = 0.2783(10)$, $\beta = 0.2068(10)$. Since $\beta \neq \alpha$, the modulation vector does not run along the diagonal of the reciprocal unit cell, but

it is slightly off-diagonal (Fig. 3.11), while in η'' it was along the diagonal. Thus, the point group of the diffraction pattern decreases in symmetry to $\overline{3}$ and the only possible space group is $P\overline{3}(\alpha, \beta, 1/3)(-\alpha - \beta, \alpha, 1/3)$ or its subgroups. 37 % of first order satellites of the type $hkl10$, and 16 % of the type $hkl\overline{1}1$ (and the symmetrically equivalent ones) were observed with enough intensities to be used in the analysis. Second order satellites of the type $hkl20$ were also observed, but since only 11 % of these satellites had intensity over 3σ, these satellites were not used in the refinement.

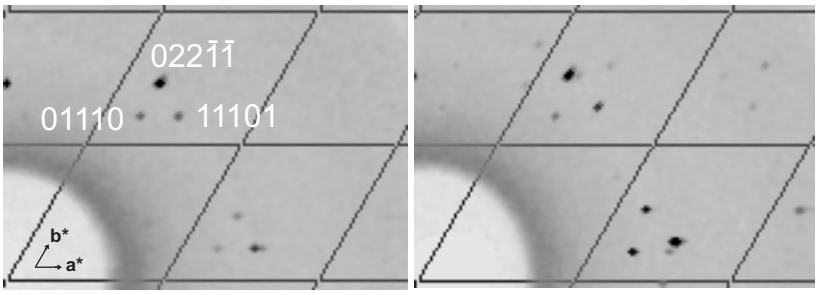

(a) (b)

Figure 3.11: Section (hk1.333) of the diffraction pattern of (a) η'' and (b) η'''. Point 0 0 1.33 in lower left corner of each panel. Lines outline the basic reciprocal lattice. Indices of three satellites are shown in (a). Note the rotation of the triangles of satellites in (b) compared to (a), which is the consequence of the rotation of the modulation vector away from the diagonal direction.

The structure of η''' was also solved in the (3+2)D superspace. Fig. 3.12 shows the density of the modulated layer B (at x_3 from 0.13 to 0.15) constructed as for η'', with the coordinate x_2 as a function of the coordinates x_4 and x_5 of the superspace, and the coordinate x_1 projected between 0 and 0.98.

As for η'', a supercell approximation was used for describing the structure of η'''. The components of the modulation vectors of η''' were approximated to $\alpha \approx 4/14 = 0.2857$ and $\beta \approx 3/14 = 0.2143$, which resulted in the supercell approximation of $14 \times 14 \times 3$. This was the smallest possible supercell for η''', which maintains the differences between η'' and η'''. The next best approximation would be the same as for η'' ($\alpha = \beta = \frac{1}{4}$). The model in the (3+2)D superspace was transformed to the 3D supercell using the relationships $h_{sc} = 14h + 4m - 7n$,$k_{sc} = 14k + 3m + 4n$,$l_{sc} = 3l + m + n$ for the reflection indices. The space group in the supercell description becomes $P\bar{3}$. Following the same procedure as for η'', an initial was obtained by EDMA through the interpretation of the Fourier map with the supercell dimensions. EDMA interpretation gave a

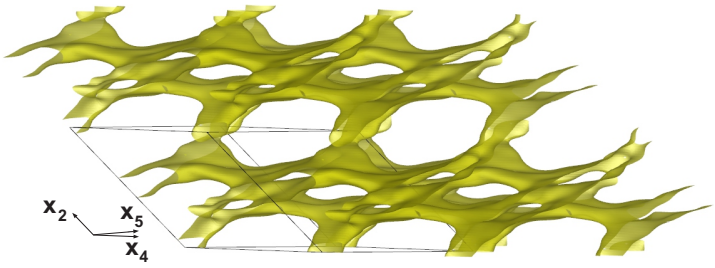

Figure 3.12: View of the density of the modulated layer B of η'''. The surface shows the density along the coordinate x_2 as a function of the coordinates x_4 and x_5. The 5D superspace density was projected along x_1 in the interval from 0 to 0.98 and along x_3 from 0.13 to 0.15 to obtain a three-dimensional representation of the extremely complex modulation function of atoms in layer B.

complete model containing 1706 independent atoms. Analogously to η'', the rings of electron density generated by the discontinuity in the modulation function were described through the superposition of six pentagons of Cu atoms rotated by 30° with respect to each other. These pentagons have spread density (Fig. 3.13) in several positions of layers B of the η''' model, which yielded discrepancies in the atomic positions found by EDMA. As a consequence, distorted geometries with very short interatomic distances were observed. These atomic positions were corrected after a visual inspection of the electron density map, where 17 atoms had their positions adjusted, resulting in one Cu-Si distance of 2.26 Å, and all other interatomic distances larger than 2.289 Å.

The data set contains only 1471 observed reflections, which excludes the possibility to refine the free model, since the number of independent atoms is larger the that of observed reflections. Thus, the option left is the fixed model, with all the atomic coordinates fixed to those values obtained by the structure solution, and with the displacement parameters restrained according to atomic species belonging to similar type of layer. These restrictions resulted in a model with six refinable parameters. R_1(obs) of this refinement converged to 11.92 %, what indicates a better agreement with the data than that of the fixed model of η''. Considering that the correct structure would be a model between the fixed and the free models for η'', and that the fixed one is the closest to the true structure, the fixed model of η''' can be safely assumed to be correct, despite the supercell approximation and the low number of observed reflections. Details of the refinement are summarized in Table 3.2.

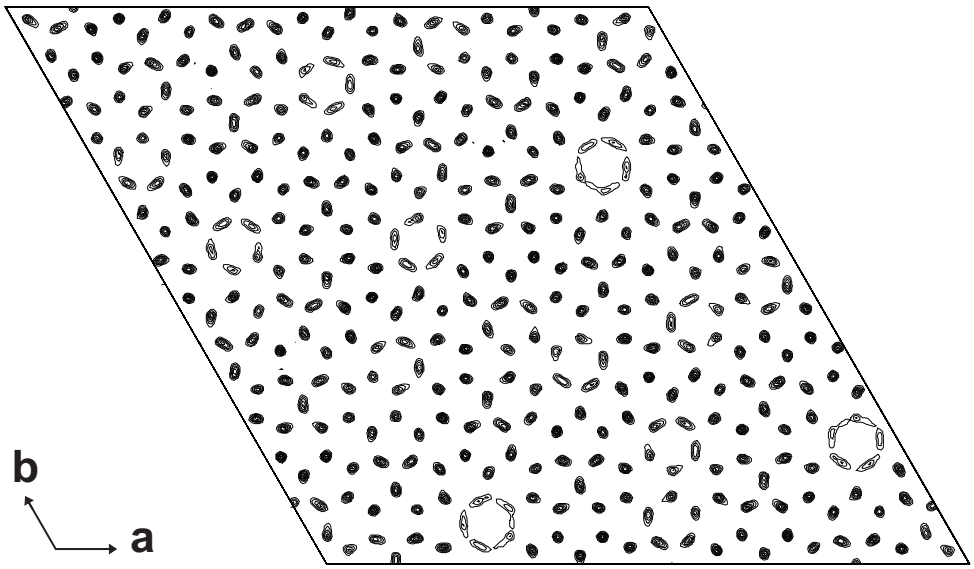

Figure 3.13: Electron density of layer B obtained from the structure solution of η'''. A tendency to smearing of pentagonal motifs is visible in several places due to the proximity of these regions to the point of discontinuity of the modulation function at $t = 0$, $u = 0$.

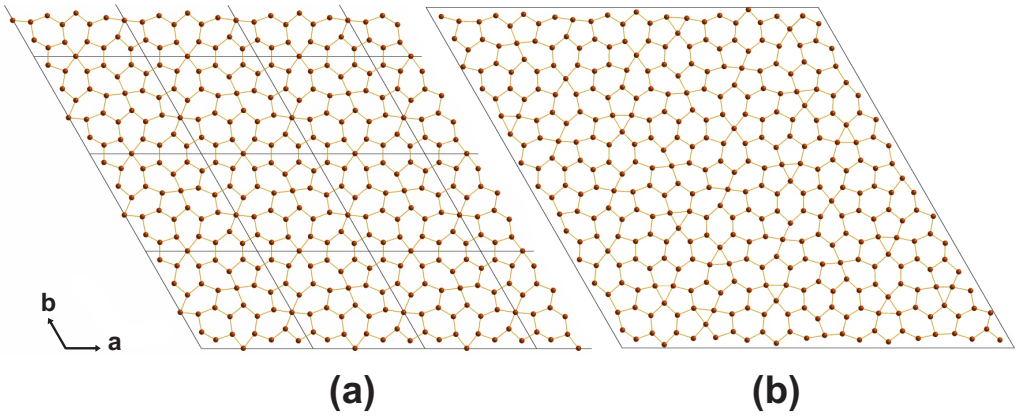

Figure 3.14: Comparison of layer B in (a) η'' and (b) η'''. In both cases 14×14 basic unit cells are shown, which correspond to 3.5×3.5 unit cells of η'' supercell, and a single unit cell of η''' supercell.

3.4.5 Chemical and crystal structure discussion

Sample Cu76 was prepared with nominal chemical composition $Cu_{76}Si_{24}$. From the results of the refinement, the average structure has chemical composition $Cu_{76.74}Si_{23.26}$, and the supercell approximation of η'' and η''' have the composi-

tion $Cu_{76.8}Si_{23.2}$. In the supercell approximation η'' contains 424 Cu atoms and 128 Si atoms per unit cell, while η''' contains 7788 Cu and 2352 Si atoms per unit cell. The composition resulting from the refinement of the structure models is in good agreement with the nominal composition of the sample. Nevertheless, the structure analysis gives higher copper contents, closer to the copper-richer limit of the stability field of $Cu_{3+x}Si$, which lies in between $Cu_{75}Si_{25}$ and $Cu_{77}Si_{23}$ [80, 81, 82]. This flexibility in the composition of $Cu_{3+x}Si$ might stem from a low number of silicon atoms placed at some copper positions. Since this replacement of Cu by Si atoms probably occurs in a few positions, it cannot be observed by diffraction and a spectroscopic analysis would be required.

The average structure and the structures of η'' and η''' can be described in terms of stacked layers along **c**, which were described in section 3.4.2 (Fig. 3.5). The average structure has twelve layers per unit cell length, from which four layers are symmetrically independent: layer A, with hexagonal geometry of Si atoms; layer B, the strongly modulated layer in honeycomb geometry composed of Cu atoms; layer C, in hexagonal geometry with Cu atoms; and layer D, which has honeycomb geometry with alternating Si and Cu atoms. η'' contains these same four symmetry independent layers. For η''' the decrease of symmetry leads to the splitting of layers A, B and C into symmetrically independent pairs (Fig. 3.5). Since in the supercell approximation the unit cell is tripled along **c**, the number of symmetry independent layers increases to 10 and 19 for η'' and η''', respectively (Fig. 3.5).

Layer B is the most strongly modulated one. In the average structure, the modulation is evidenced through the smeared electron density in a honeycomb shape (Fig. 3.7). In the supercell of both η'' and η''' the Cu atoms of the layers B form an arrangement of alternating deformed pentagons and elongated hexagons, instead of a honeycomb shape (Fig. 3.14). The supercell approximation of η'' contains three independent layers B, but they are all symmetry equivalent in the modulated structure. Since each of these layers split in pairs of symmetrically independent layers in η''', six independent layers B are present in η''', which correspond to two independent layers B in the modulated structure. The only difference between the layers B of η'' and η''' is the arrangement of the pentagons and elongated hexagons (Fig. 3.14). Even though these B layers of η'' and η''' have different disposition of motifs, they have the same number of atoms in the modulated structure and their overall appearance is very similar. Although η'' appears to have a mirror plane in the layer B, while in η''' the absence of the mirror plane is clear, there is no mirror plane imposed by symmetry in the B layer of η'' neither. These B layers have two-dimensional plane group $p3$ and the planar symmetry can very well be approximated to $p31m$ in both phases.

The three-dimensional structures of η'' and η''' can be described using five types

of Si-centered polyhedra (Fig. 3.15), which are either face- or edge-shared. In four of them the Si atom of the hexagonal Si layers coordinates 12-14 Cu atoms: a dual hexagonal/pentagonal capped antiprism with the Cu-Si distances between ≈ 2.43 Å and ≈ 2.72 Å; a polyhedron denominated 12+2, with the central Si atom coordinated by twelve Cu atoms at distances from 2.35 Å to 2.74 Å and two Cu atoms further, at ≈ 3.1 Å and 3.3 Å; a twisted hexagonal capped prism with the Cu atoms coordinating the central Si at distances between 2.35 Å and 2.8 Å; and an icosahedron, with the Cu atoms coordinating the central Si within a distance of 2.4 Å and 3.01 Å. The fifth polyhedron is a distorted pentagonal capped antiprism (Fig. 3.15(e)), which is formed around the Si atom of the honeycomb layer, with Cu atoms coordinating the central Si within 2.36 Å and 2.75 Å of distance.

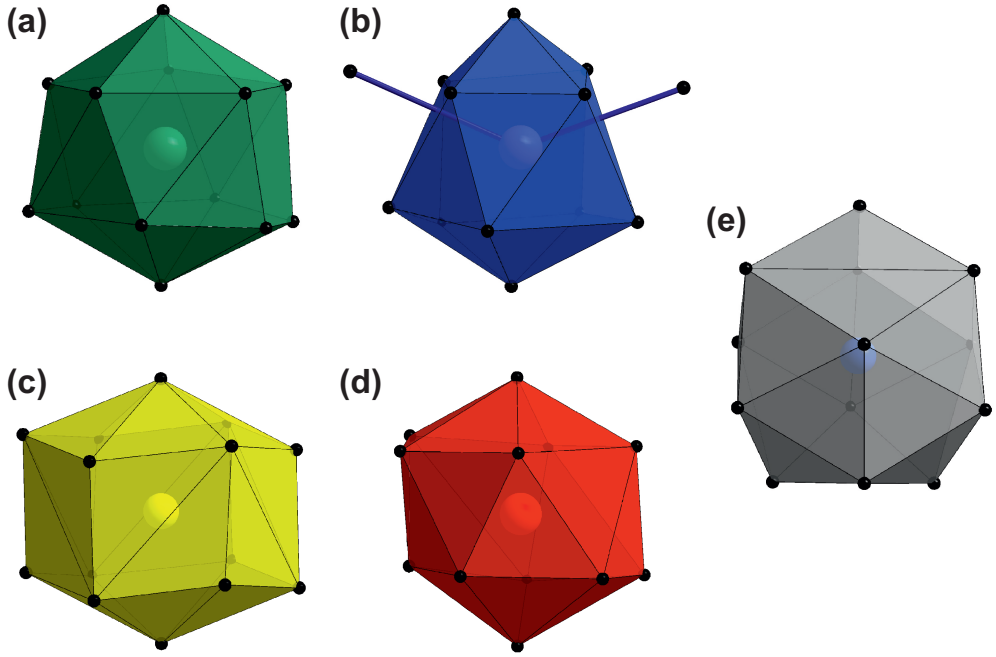

Figure 3.15: Clusters forming the structure 3-dimensional framework: (a) dual hexagonal/pentagonal capped antiprism; (b) the 12+2 cluster; (c) the twisted hexagonal capped prism; (d) icosahedron; (e) distorted pentagonal capped antiprism.

The most frequent polyhedron is the icosahedron for both models η'' and η''' (Fig. 3.16), and the 12+2 polyhedron is the second most observed one. Each unit cell of η'' has nine icosahedra per layer B, six 12+2 polyhedra, and one dual hexagonal/pentagonal capped antriprism. Each layer B of η''' has 99 icosahedra, 84 polyhedra of the type 12+2, and 13 dual hexagonal/pentagonal capped antiprisms per unit cell.

It is worth to mention the similarity between the layers B of η'' and the η' model [26]. The disposition of the polyhedra is exactly the same for both models η'' and η' (Fig. 3.16), while in η''' these polyhedra are more deformed. This similarity comes from the close relation between η'' and η', which is characterized by an order-disorder transition. The honeycomb layer with intercalated Cu and Si atoms in η'' becomes disordered in η', with Cu and Si atoms sharing sites [26, 95].

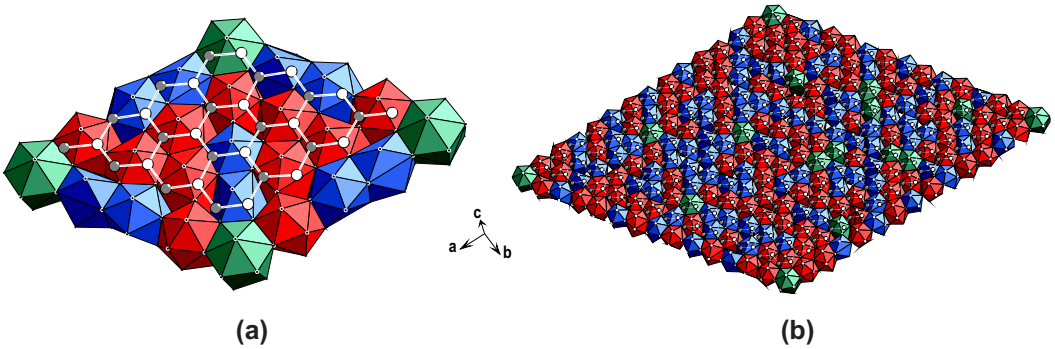

Figure 3.16: Cluster distribution on layer B of (a) η'' and (b) η'''. The most present polyhedron is the icosahedron, followed by the 12+2 polyhedron. η'' has the same cluster distribution as η' [26].

The deformed pentagons and elongated hexagons provide enough flexibility for the polyhedra to rearrange during the phase transition from η'' to η''' as a function of temperature, decreasing the symmetry and generating the volumetric expansion of the unit cell observed at lower temperature [95].

3.4.6 Phases observed by temperature-dependent powder X-ray diffraction

TD-PXRD patterns of the sample Cu74 contain six phases and weak Si peaks, which was expected to be in equilibrium with the $Cu_{3+x}Si$ phase according to the phase diagram. Si crystals can be seen as dark particles in the scanning microscope images of Cu74 (Fig. 3.17 (a)). Diffraction patterns of the sample Cu78 is very similar to that of Cu74. Cu78 presented ϵ in equilibrium with $Cu_{3+x}Si$ (Fig. 3.17 (b)), and the PXRD patterns contain the expected ϵ peaks.

One pattern of each phase observed in Cu74 was indexed (Fig. 3.18), in order to characterize the phases. The observed phases are similar in both samples and thus the indexing of the phases in Cu78 is not presented. The observed new phases were named in analogy to the nomenclature from the phase diagram, from the lowest temperature to the highest: η''', η'', η', η_3, η_2 and η_1. The phases transitions observed in Cu78 are equivalent to that of Cu74, but only the phases

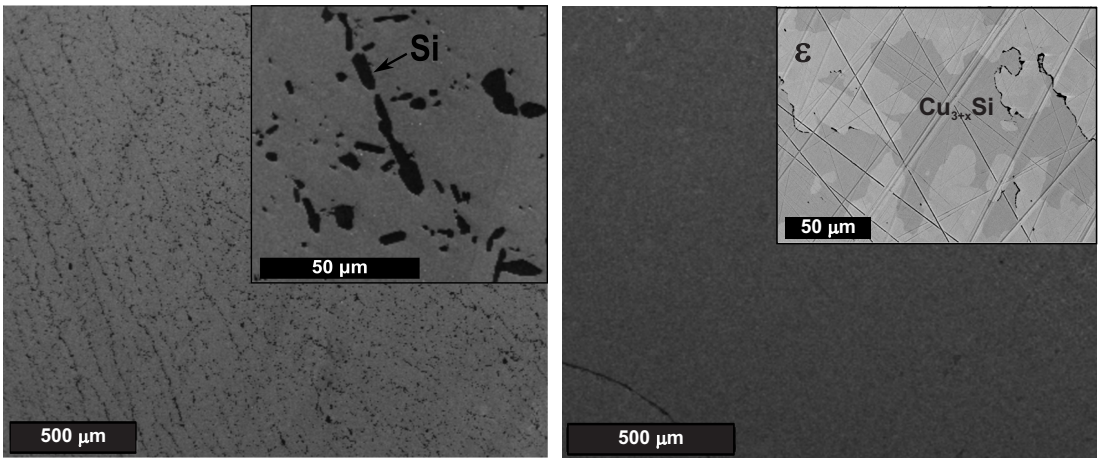

Figure 3.17: Scanning electron microscope image of the samples (a) Cu74 in secondary electrons, showing the $Cu_{3+x}Si$ phase (grey) and silicon crystals (dark particles); and (b) Cu78 in secondary electrons (main image). The inset is the back scattered electrons of ϵ (light grey) and $Cu_{3+x}Si$ (dark grey) phases.

η''', η'', η', and η_2 are present. The phases η_3 and η_1 are absent. η''' was indexed in the pattern collected at 150 °C, using the unit cell parameters and the values of the modulation vectors obtained by TD-SCXRD presented in sections 3.4.4. The extreme modulation of the structure is evident in the strong intensity of the satellites present in the pattern (Fig. 3.18 (a)). The pattern collected at 330 °C was used for the indexing of η'' (Fig. 3.18 (b)), for which the unit cell parameters and the values of the modulation vectors were obtained by TD-SCXRD, according to section 3.4.3. The phase η' ((Fig. 3.18) (c)) was indexed using the model by Palatinus *et al.* [26] in the pattern collected at 420 °C. η_3 was the only pattern which could not be completely indexed ((Fig. 3.18) (d)) . According to our indexation, η_3 has a trigonal unit cell with parameters a≈ 4.08 Å and c≈ 7.38 Å (Table 3.3), similarly to η'. However, we could not index the satellites of η_3, in spite of several attempts based on the other phases. The position of the satellites of η_3 indicates also a modulated structure, either (3+2)D or (3+1)D. Similarly to the previous indexed phases, η_2 ((Fig. 3.18) (e)) is an incommensurately modulated structure, but with a (3+1)-dimensional one, with a single modulation vector $\mathbf{q} = \gamma\mathbf{c}^*$. $\gamma \approx 0.11$ in Cu74 and $\gamma \approx 0.087$ in Cu78. η_2 was already observed by Wen and Spaepen [86], when it was interpreted as the formation of a long-period anti-phase domain. The last phase observed was η_1, which is characterized by the disappearance of the satellites ((Fig. 3.18) (f)) . This phase can be indexed with the trigonal unit cell very similar to the basic unit cells of the phases η_3 and

η_2. The lattice parameters and modulation vectors components of the six phases follow in Table 3.3.

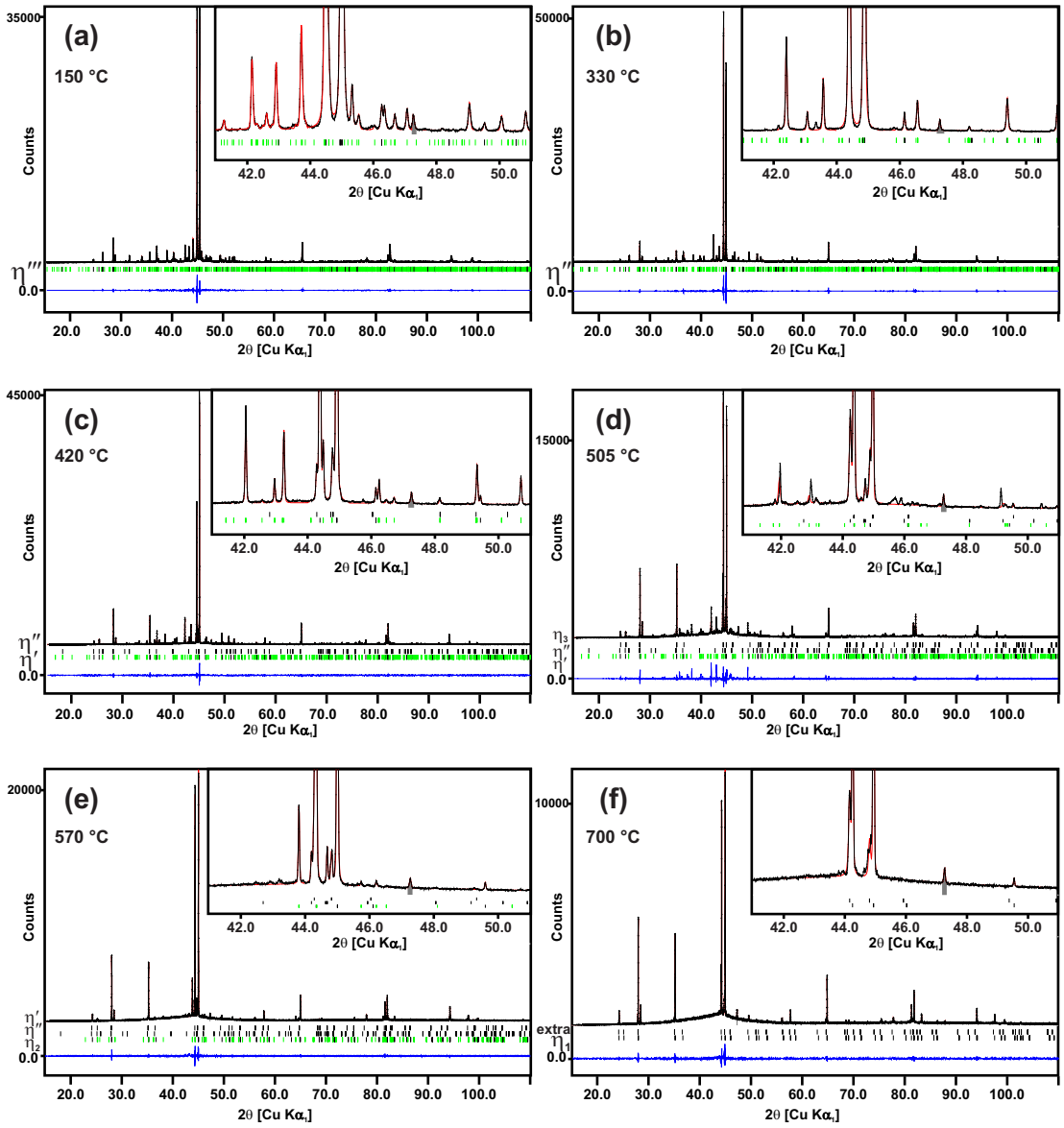

Figure 3.18: Indexed PXRD patterns of the six phases in Cu74. The temperatures correspond to the center of the main stability range of each phase. In some patterns more than one phase coexist. Main phases: (a) η''', (b) η'', (c) η', (d) η_3 (e) η_2, (f) η_1.

Table 3.3: Basic crystallographic information of the phases η''', η'', η', η_3, η_2, η_1 as determined in the sample Cu74 at selected temperatures. The temperatures were selected close to the middle of the stability range of each phase in the sample Cu74. Unit cell parameters and modulation vectors presented are the values refined from the TD-PXRD at each temperature in this work, superspace groups are from [26] (η') and [88] (η'' and η''').

	T(°C)	a Å	c Å	$\mathbf{q_1}$	$\mathbf{q_2}$	Space group
η'''	150	4.06603(7)	14.7035(2)	(0.23458(7),0.28171(7),$\frac{1}{3}$)	(-0.5163(1),0.23458(7)$\frac{1}{3}$)	$P\bar{3}(\alpha,\beta,\frac{1}{3})(-\alpha-\beta,\alpha,\frac{1}{3})$
η''	330	4.07899(6)	14.7532(3)	(0.25913(6),0.25913(6),$\frac{1}{3}$)	(-0.51826(8),0.25913(6),$\frac{1}{3}$)	$P\bar{3}1c(\alpha,\alpha,\frac{1}{3})(-2\alpha,\alpha,\frac{1}{3})$
η'	420	4.08082(3)	7.37221(7)	(0.26860(2),0.26860(2),$\frac{1}{3}$)	(-0.53721(4),0.26860(2),$\frac{1}{3}$)	$P\bar{3}1m(\alpha,\alpha,\frac{1}{3})(-2\alpha,\alpha,\frac{1}{3})$
η_3	505	4.0857(2)	7.3798(5)			
η_2	570	4.08785(4)	7.35384(8)	(0,0,0.11279(4))		
η_1	700	4.09738(4)	7.36530(9)			

3.4.7 Phase transitions

TD-PXRD of samples Cu74 and Cu78 had both heating-cooling cycles presenting the same sequence of transitions at the same temperatures. The difference between the cycles was a weak hysteresis in the phase transitions, and thus only the first heating of the first cycle is shown in Figs. 3.19 and 3.20, for samples Cu74 and Cu78, respectively.

The temperature dependence of the unit cell parameters of Cu74 is shown in Fig. 3.21, while the temperature evolution of the components of the modulation vectors α and β is presented in Fig. 3.22. The evolution of the unit cell parameters and components of the modulation vectors with increasing temperature in Cu78 are shown in Figs. 3.23 and 3.24, respectively. For both Cu74 and Cu78 the evolution of the parameters as a function of the temperature is presented for heating (full red symbols) and cooling (full blue symbols). Empty symbols represent the permanence of a specific phase outside its principal stability range.

Cu74 and Cu78 patterns measured from room temperature until 120 °C have broad peaks with shifted positions (Figs. 3.19 and 3.20). This behavior generates changes on the slope of the curve of the thermal expansion of the unit cell parameters (Figs. 3.21, 3.23). The change in the slope of the curve is also observed for the components of the modulation vectors (Figs. 3.22, 3.24) with increasing temperature. This effect disappears above 150 °C, when the peaks become sharper and only the thermal expansion is observed. This feature might be explained by the sample preparation process. Since the bulk samples are crashed and ground in the mortar, the strain generated disappears with increasing temperature. For this reason annealing of alloys after the grinding process is a common practice [96]. Hence, the patterns acquired until 120 °C are not used for the analysis of the thermal evolution of the phases.

Since the measurements were performed in steps of either 30 °C or 5 °C, the

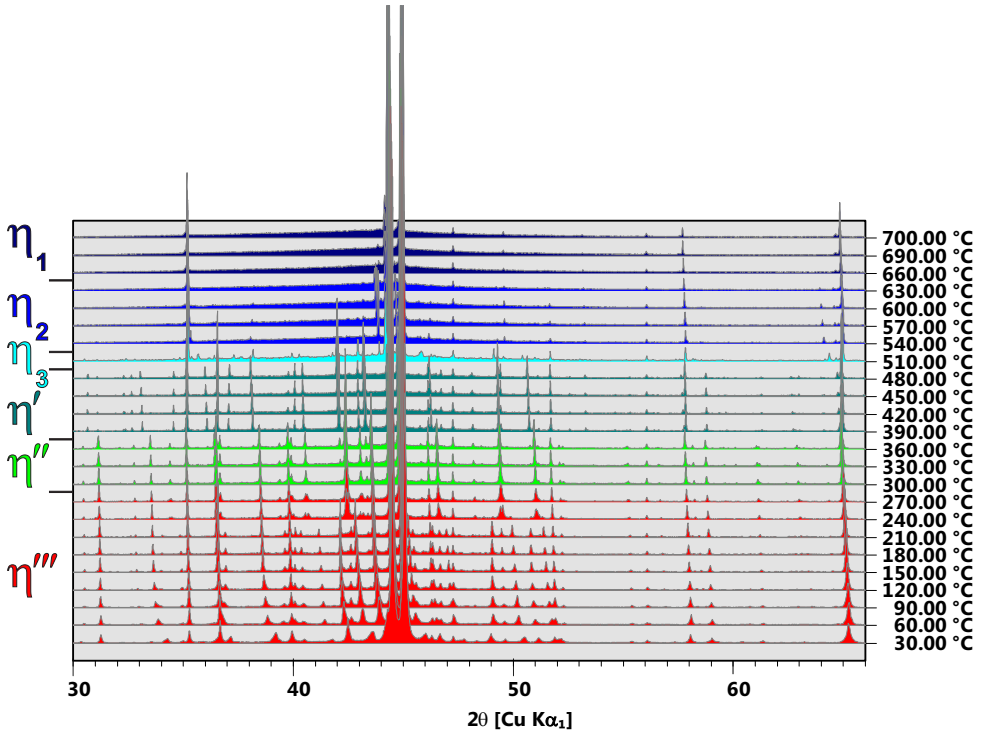

Figure 3.19: Powder diffraction patterns of the sample Cu74 as a function of temperature from 30 °C to 700 °C. The patterns are colored according to the main phase present in the pattern.

range of temperature stability is presented as being in between the appearance of two phases. For instance, in sample Cu74 the last pattern of η''' is observed at 270 °C and the first pattern of η'' is observed at 300 °C. Hence, η''' is defined as being stable between the room temperature and 285±15 °C.

η''' is observed at room temperature and it is stable until 315±15 °C in Cu78. The transition from η''' to η'' is characterized by the change of $\beta \neq \alpha$ to $\beta = \alpha$. In the sample Cu74, there are smooth changes on the components α and β from room temperature up to 210 °C. An abrupt change occurs between 210 °C and 240 °C, but α and β remain different ($\alpha = 0.26193(3)$, $\beta = 0.25538(3)$). The temperature evolution continues smoothly between 240 °C and 270 °C, when β converges to $\alpha = \beta = 0.25884(2)$ at 300 °C. However, this transition occurs at once during the cooling, from $\alpha = \beta = 0.25888(1)$ (η'') to $\alpha = 0.27641(2)$, $\beta = 0.24132(2)$ (η'''). In order to verify if this smooth change is in fact due to the release of strain caused by the sample preparation, a short TD-PXRD measurement was performed on sample Cu74 under heating from 30 °C to 150 °C, and cooling to room temperature. Broad peaks become sharp during the heating, what we interpret as the disappearance

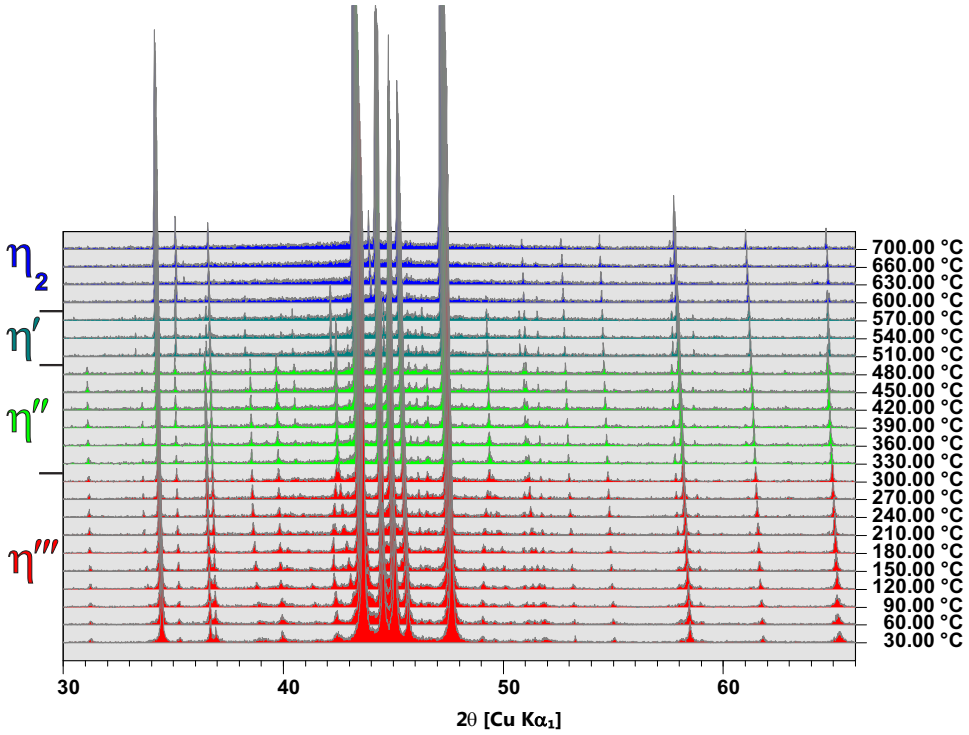

Figure 3.20: Powder diffraction patterns of the sample Cu78 as a function of temperature from 30 °C to 700 °C. The patterns are colored according to the main phase present in the pattern.

of the strain.

Similarly to Cu74, this first transition occurs smoothly during heating of the sample Cu78, and abruptly during the cooling. The abrupt change before the transition during the heating does not occur for Cu78, though. With increasing temperature, $\alpha = 0.26066(6)$, $\beta = 0.25302(6)$ (at 300 °C) changes to $\alpha = \beta = 0.25660(3)$ (at 330 °C), while on cooling $\alpha = \beta = 0.25858(3)$ modifies to $\alpha = 0.27834(5)$, $\beta = 0.23702(5)$.

The transition from η''' to η'' is a first-order transition, which occurs slowly during the first heating due to the strain caused by the sample preparation and with behavior depending on the history of the sample.

η'' is observed in the range 285±15 °C – 375±15 °C in Cu74 and 315±15 °C – 475±15 °C in Cu78. This phase is characterized by the components of the modulation vectors $\beta = \alpha$. Hence, $q_1 = (\alpha, \alpha, 1/3)$ and $q_2 = (-2\alpha, \alpha, 1/3)$. η'' has $\alpha \approx 0.25$ and thus one could expect it to converge to a commensurate value for higher temperatures. In spite of using the supercell approximation with $\alpha = 0.25$ for the SCXRD model, the thermal evolution of the components of the modulation

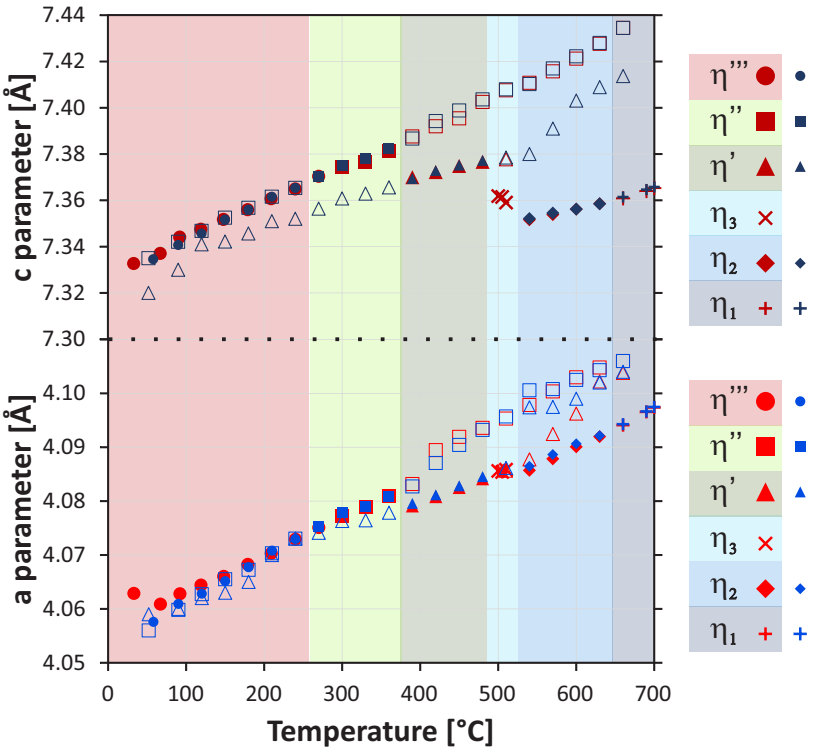

Figure 3.21: Evolution of the unit cell parameters with temperature for the samples Cu74. Larger red symbols for heating, smaller blue symbols for cooling. Empty symbols represent phases outside of their main stability range. Colored background fields delimit the stability ranges of individual phases.

vectors clearly shows that there is no convergence to a commensurate value (Table 3.3, Figs. 3.22, 3.24). Peaks of the main reflections are observed up to 660±15 °C in sample Cu74, as observed in Figs. 3.18 and 3.21, while in Cu78 the transition to η' occurs completely at 475±15 °C.

The phase η' is observed from 375±15 °C – 497.5±15 °C in Cu74 and from 480±15 °C to 585±15 °C in Cu78. As for η'', η' is also incommensurately modulated and the components of the modulation vector do not converge to a commensurate value (Figs. 3.22, 3.24). The transition to η' occurs when D layer becomes disordered and the c axis of η'' almost halves its length (Table 3.3) [26, 88] and the modulation vector increases from $\alpha = 0.25935(1)$ to $\alpha = 0.26810(1)$ in Cu74 and from $\alpha = 0.25615(2)$ to $\alpha = 0.26322(3)$ in Cu78 (Figs. 3.22, 3.24). During the transition the unit cell volume contracts by 0.17 % (Fig. 3.21) for Cu74. Since Si has shorter atomic radius than copper and Si crystals are observed in the matrix of $Cu_{3+x}Si$ (Fig. 3.17), this contraction could be interpreted as the result of the increase of silicon content in the η' phase coming from the dissolving Si crystals.

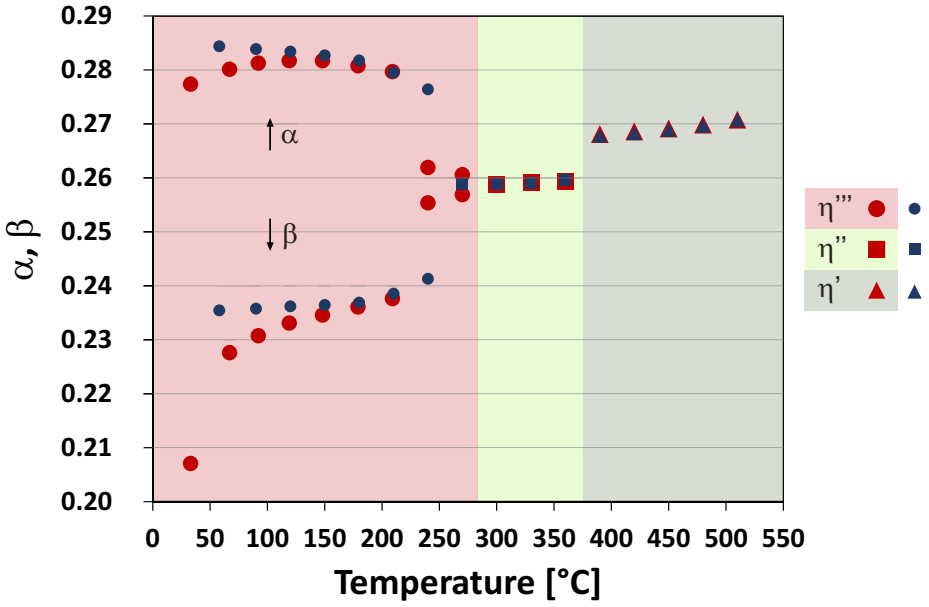

Figure 3.22: Evolution of the components α and β of the modulation vector as a function of temperature in the sample Cu74. The transition from η''' to η'' is marked by the value of β becoming equal to α. Larger red symbols for heating, smaller blue symbols for cooling. Colored background fields delimit the stability ranges of individual phases.

However, the composition of both phases η'' and η' is the same [88] and peaks of Si do not change intensity in the powder diffraction patterns. Hence, the contraction of the unit cell has origin in rotation and rearrangement of the clusters of the modulated layer B, shrinking the unit cell with increasing temperature (see section 3.4.5). This effect is observed for other materials as well [97].

The phase diagrams [80, 81, 82, 83, 84] contains a single field called η above η', but a narrow two-phase field is present between η' and η in the phase diagram of Olesinski and Abbaschian [80]. Our TD-PXRD exhibits a complex sequence of patterns above η', where at least two extra phases can be identified. Moreover, a double peak in the DSC results of [98, 86] indicates the existence of an extra phase and sample Cu74 exhibited one pattern with distinct peaks at 510 °C. We decided thus to perform a more detailed measurement in the range 480 °C – 525 °C using steps of 5 °C. η_3 was observed in Cu74 between 500 °C – 515 °C (Fig. 3.25), being the main phase present at 510 °C. It appears at 500 °C as weak peaks, and disappears at 515 °C, when η_2 starts. It was not observed in Cu78.

η_2 appears after η_3, between 515±15 °C and 645±15 °C in Cu74, and after η' for Cu78, from 585±15 °C to at least 700 °C, which was the highest measured temperature. However, since the phases in Cu78 are stable until higher temperatures,

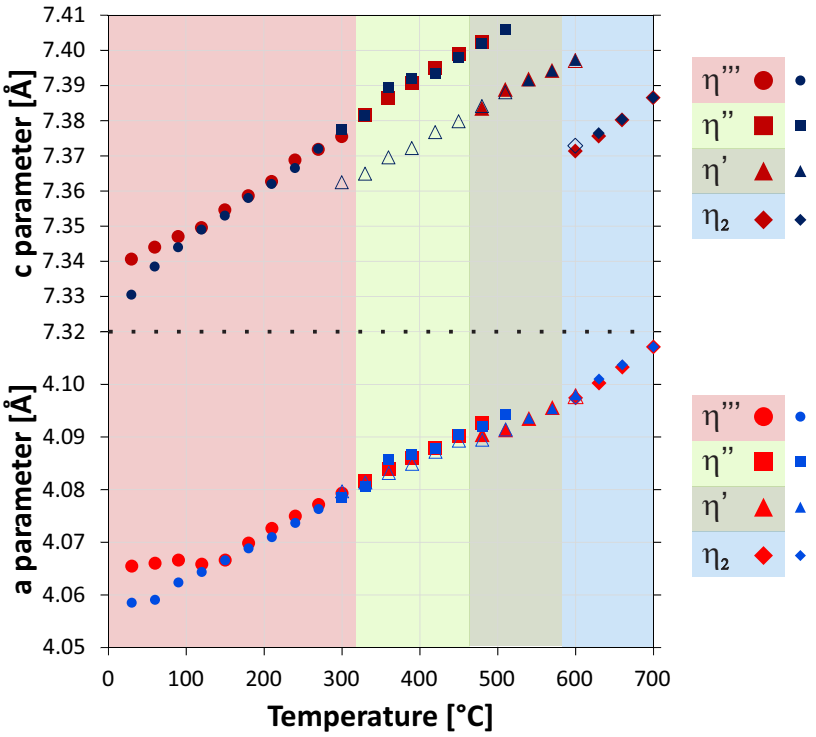

Figure 3.23: Evolution of the unit cell parameters with temperature for the samples Cu78. Larger red symbols for heating, smaller blue symbols for cooling. Empty symbols represent phases outside of their main stability range. Colored background fields delimit the stability ranges of individual phases.

it is reasonable to assume that η_2 is still stable above 700 °C. Similarly to the previous indexed phases, η_2 is an incommensurately modulated structure, but a (3+1)-dimensional one with a single modulation vector $\mathbf{q} = \gamma\mathbf{c}^*$. $\gamma = 0.1075(1)$ in Cu74 and $\gamma = 0.0870(2)$ in Cu78. The evolution of γ with increasing temperature can be seen in Fig. 3.26.

Together with η_2, weak main reflections belonging to η'' and η' can be observed until the transition to the next phase η_1 in the sample Cu74, when these peaks from η'' and η' disappear. This coexistence of η'', η' and η_2 is not allowed in a two-components equilibrium system, according to the Gibb's rule. This result suggests an inhomogeneous sample. However, a line EDS mapping (Fig. 3.27) shows that the sample is homogeneous, within the experimental errors. Nevertheless, according to the calculated phase diagram by Gierlotka [83] and Hallstedt [84], $Cu_{3+x}Si$ phases are described as line compounds with a difference of compositions of 0.5 % Cu, which would not be observed in EDS results if the sample would have small local differences in the silicon-$Cu_{3+x}Si$ ratio.

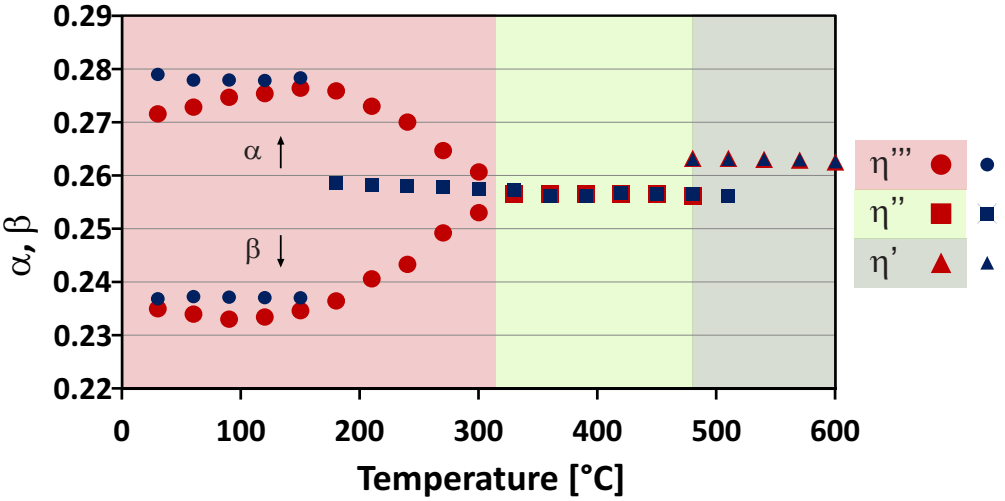

Figure 3.24: Evolution of the components α and β of the modulation vector as a function of temperature in the sample Cu78. The transition from η''' to η'' is marked by the value of β becoming equal to α. Larger red symbols for heating, smaller blue symbols for cooling. Colored background fields delimit the stability ranges of individual phases.

The last phase observed is η_1, which was present above 645±15 °C in Cu74, and it is most likely to be present at temperatures higher than 700 °C in Cu78, above η_2. A few extra peaks appear at lower 2θ values in relation to the strongest main peaks of η_1 (Fig. 3.28), which are easily observed around (2θ) 44.3° and 45.0°, reflections 110 and 103, respectively. These extra peaks can be indexed with a slightly larger unit cell, what we used for the indexation of the patterns to avoid a biased indexing of η_1. Another possibility would be the origin of another superstructure. An attempt to index these extra peaks as satellites with a single modulation vector along $\mathbf{c}^*$ did not index all the observed peaks. A component along $\mathbf{a}^*$ would also be necessary. However, it was not possible to find a conclusive interpretation about them, since these extra peaks are weak and there are only a few of them.

Despite of having observed at least two new phases in the Cu-Si system, further investigation is necessary to include these findings to the phase diagram. Two of the phases observed had the crystal structure elucidated by SCXRD: η''' and η''. Five from the six phases observed by TD-PXRD in the sample Cu74 were indexed using either our models from SCXRD or information based on the known models. Four phases were observed in the PXRD in the sample Cu78 and all of them were indexed.

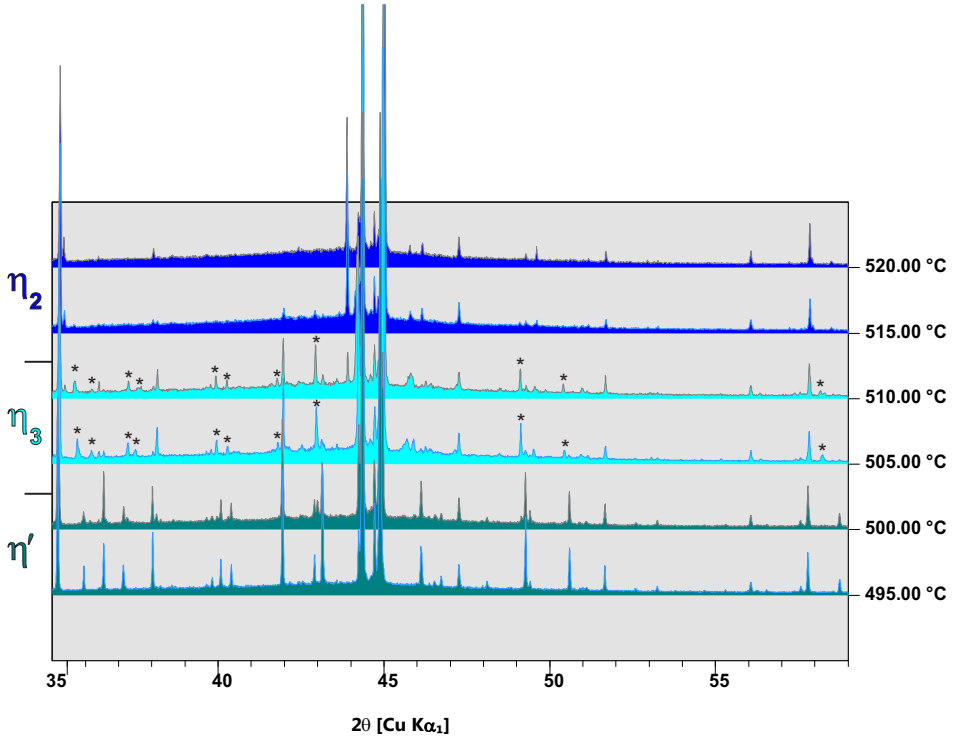

Figure 3.25: Powder diffraction patterns of the sample Cu74 from 490 °C to 510 °C in steps of 5 °C. The most prominent peaks specific for η_3 are marked with asterisks.

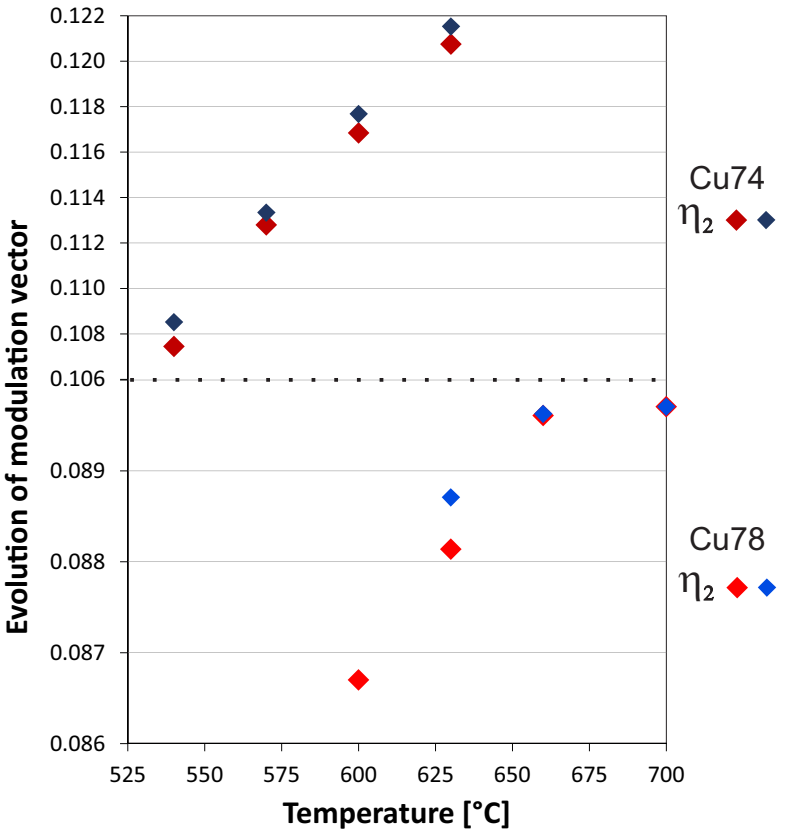

Figure 3.26: The evolution of the component γ of the modulation vector of the phase η_2 in Cu74 and Cu78.

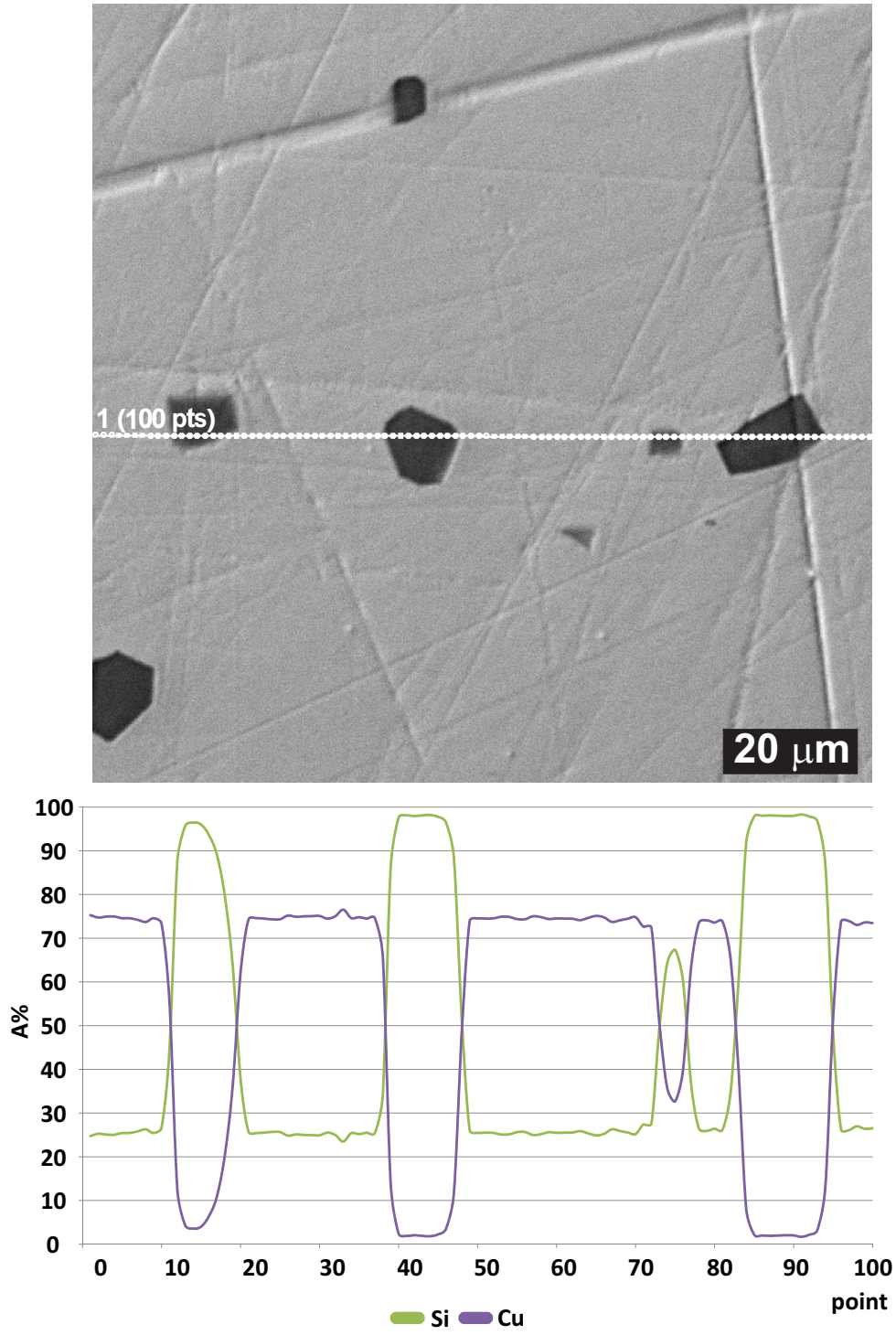

Figure 3.27: STEM image and the corresponding EDS line scan along the sample Cu74.

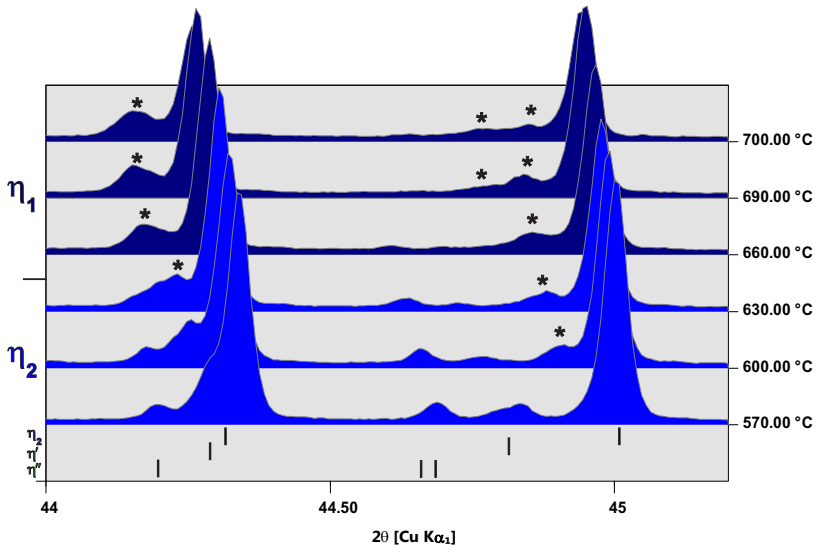

Figure 3.28: The disappearance of the peaks of η'' and η' and evolution of additional peaks (marked with asterisks) in the temperature range between 570 °C and 700 °C.

4. Conclusions and future work

In this thesis we presented tests on the newly developed dynamical refinement (Chapter 2) [28], a method that allows one to obtain accurate crystal structures on nanocrystals by electron diffraction tomography (EDT) data. The parameters used during the dynamical refinement were tested comparing the refinement of precession electron diffraction tomography (PEDT) data, acquired on a nanowire of Ni_2Si with the diameter of $\approx$ 15 nm, with a high-quality single crystal X-ray diffraction (SCXRD) model.

According to the results from the tests we could identify the optimum values for the parameters of the method. These optimum values are valid for standard refinement. It was shown that the accuracy obtained by the dynamical refinement for PEDT approaches that of SCXRD [43], which is the standard technique used for obtaining crystal structure on microscopic single crystals.

Knowing the optimized values of the parameters of the dynamical refinement, their behavior and their limitations, the crystal structure of the transition metal silicide Ni_3Si_2 was redetermined on a single nanowire with the diameter of 35 nm [99]. The structure had a good agreement with the model obtained by single crystal X-ray diffraction, giving an average distance to the atomic position of the SCRXD model of less than 0.01 Å. The structure of the Ni_3Si_2 was shown to be centrosymmetric $Cmcm$, in disagreement with the published structure determined in 1961 as $Cmc2_1$.

This work shows that the dynamical refinement used for PEDT data removes the barrier of lack of knowledge of crystal structure of nanomaterials that cannot be grown as large single crystals, allowing the understanding of the properties of a higher number of materials.

The next objective was to apply the dynamical refinement to an unknown crystal structure. For that we used samples of the copper silicide $Cu_{3+x}Si$. Since this alloy undergoes phase transitions with increasing temperature, we measured temperature dependent PEDT data. Two incommensurately modulated structures were observed. Their modulation was so complex that it was not possible to refine the structure model using standard approach, and a hybrid approach was used for obtaining the dependence of the crystal structures on the temperature. For that, temperature-dependent powder X-ray diffraction was measured on samples with nominal composition $Cu_{74}Si_{26}$ and $Cu_{78}Si_{22}$. Six distinct phases were observed in the $Cu_{3+x}Si$ system. In order of increasing temperature, the phases observed were: η''', η'', η', η_3, η_2 and η_1. The phases η''' and η'' were elucidated by SCRXD and they were shown to be extremely modulated, while the phases η_2 and η_1 were indexed by PXRD. According to our results, the binary Cu-Si phase diagram might be more complex than the one presented by Olesinski and Abbaschian [80].

It was shown that at least four incommensurately modulated phases are present in the system $Cu_{3+x}Si$. Despite of the phase transitions being reversible and having indexed five of the six phases, we could not include these newly observed phases to the Cu-Si phase diagram. The reason is the coexistence of three phases in the TD-PXRD results of the sample $Cu_{74}Si_{26}$, which is not allowed for a two-components system in equilibrium by the Gibb's rule. More investigation is needed to better understand the system $Cu_{3+x}Si$.

As future work on the system $Cu_{3+x}Si$, we plan to analyze samples with smaller compositional variation, in order to verify the influence on the phase transitions observed. The thermostability, by differential scanning calorimetry, and high resolution microscopy images are two of the possible approaches to be added to X-ray diffraction analysis. Another approach would be to find the driving force of the modulation within the phases of the system $Cu_{3+x}Si$. For that, the elongation of the atomic displacement parameters might be used, and the distribution of the pentagons and distorted hexagons in the honeycomb layers as well, in a approach similar to that followed by W. Hornfeck [100] to identify defects in the iridium-zinc system. The identification of the position of defects would be connected to the modulation vectors, allowing one to predict general aspects of the crystal structure based on the modulation vectors observed.

Bibliography

[1] C. Davisson and L. H. Germer. Diffraction of electrons by a crystal of nickel. *Physical Review*, 30:705–740, 1927.

[2] G. P. Thomson and A. Reid. Diffraction of cathode rays by a thin film. *Nature*, 119:890, 1927.

[3] E. Ruska. The development of the electron microscope and of electron microscopy. In Tore Frängsmyr, editor, *Nobel Lecture*, pages 1397–1467, Berlin, 1986.

[4] B. K. Vainshtein. Structure Analysis by Electron Diffraction, 1956.

[5] B. K. Vainshtein. *Structure Analysis by Electron Diffraction*, volume 4. Pergamon Press, Great Britain, 1956. Edited by E. Feigl and J. A. Spink.

[6] J. M. Cowley. Structure analysis of single crystals by electron diffraction. I. Techniques. *Acta Crystallographica*, 6:516–521, 1953.

[7] J. M. Cowley. Structure analysis of single crystals by electron diffraction. II. Disordered boric acid structure. *Acta Crystallographica*, 6:522–529, 1953.

[8] A. Authier. *Dynamical Theory of X-Ray Diffraction*. Oxford Science Publications, Great Clarendon Street, Oxford OX2 6DP, 2001.

[9] P. H. Dederichs. Dynamical Diffraction Theory. Technical report, Berichte der Kernforschungsanlage Jülich, Institut fur Festkörperforschung, 1971.

[10] J. C. H. Spence and J. M. Zuo. *Electron Microdiffraction*. Plenum Press, New York, 1992.

[11] U. Kolb, E. Mugnaioli, and T.E. Gorelik. Automated electron diffraction tomography - a new tool for nano crystal structure analysis. *Cryst. Res. Technol.*, 46:542–554, 2011.

[12] R. Vincent and P. A. Midgley. Double conical beam-rocking system for measurement of integrated electron diffraction intensities. *Ultramicroscopy*, 53:271–282, 1994.

[13] K. Gjønnes. On the integration of electron diffraction intensities in the Vicent-Midgley precession technique. *Ultramicroscopy*, 69:1–11, 1997.

[14] K. Tsuda and M. Tanaka. Refinement of crystal structure parameters using Convergent-Beam Electron Diffraction: the low-temperature phase of $SrTiO_3$. *Acta Crystallographica*, A51(1):7–19, 1995.

[15] J. Jansen, D. Tang, H. W. Zandbergen, and H. Schenk. MSLS, a least-squares procedure for accurate crystal structure refinement from dynamical electron diffraction patterns. *Acta Crystallographica*, A54:91–101, 1998.

[16] K. Tsuda and M. Tanaka. Refinement of crystal structural parameters using two-dimensional energy-filtered CBED patterns. *Acta Crystallographica*, A55:939–954, 1999.

[17] A. P. Dudka, A. S. Avilov, and G. G. Lepeshov. Crystal structure refinement from electron diffraction data. *Crystallography Reports*, 53:530–536, 2008.

[18] P. Oleynikov. eMap and eSlice: a software package for crystallographic computing. *Crystal Res. Technol.*, 46:569–579, 2011.

[19] C. J. Rossouw, M. A. Gibson, and C. T. Forwood. Dynamical electron diffraction analysis of lattice parameters, Debye—Waller factors and order in Ti-Al and Ti-Ga alloys. *Ultramicroscopy*, 66(3):193–209, 1996.

[20] U. Kolb, T. Gorelik, C. Kübel, M. T. Otten, and D. Hubert. Towards automated diffraction tomography: Part I - Data acquisition. *Ultramicroscopy*, 107:507–513, 2007.

[21] U. Kolb, T. Gorelik, and M. T. Otten. Towards automated diffraction tomography. Part II - Cell parameter determination. *Ultramicroscopy*, 108:763–772, 2008.

[22] D. Zhang, P. Oleynikov, S. Hovmöller, and X. Zou. Collecting 3D electron diffraction data by the rotation method. *Zeitschrift für Kristallographie*, 225:94–102, 2010.

[23] W. Wan, S. Junliang, J. Su, S. Hovmöller, and X. Zou. Three-dimensional rotation electron diffraction: software RED for automated data collection and data processing. *Journal of Applied Crystallography*, 46:1863–1873, 2013.

[24] M. Gemmi, A. Galanis, F. Karavassili, P. P. Das, M. Calamiotou, A. Gantis, M. Kollia, I. Margiolaki, and S. Nicolopoulos. Structure determination of nano-crystals with precession 3D electron diffraction tomography in the transmission electron microscope. *Microscopy and Analysis*, 27(2):24, 2013.

[25] M. Gemmi and S. Nicolopoulos. Structure solution with three-dimensional sets of precessed electron diffraction intensities. *Ultramicroscopy*, 107:483–494, 2007.

[26] L. Palatinus, M. Klementová, V. Dřínek, M. Jarošová, and V. Petříček. An incommensurately modulated structure of $\eta'-$phase of $Cu_{3+x}Si$ determined by quantitative electron diffraction tomography. *Inorganic Chemistry*, 50:3743–3751, 2011.

[27] L. Palatinus, D. Jacob, P. Cuvillier, M. Klementová, W. Sinkler, and L. D. Marks. Structure refinement from precession electron diffraction data. *Acta Crystallographica*, A69:171–188, 2013.

[28] L. Palatinus, V. Petříček, and C. A. Corrêa. Structure refinement using precession electron diffraction tomography and dynamical diffraction: theory and implementation. *Acta Crystallographica*, A71:235–244, 2015.

[29] V. Petříček, M. Dušek, and L. Palatinus. The crystallographic computing system Jana2006, 2006.

[30] V. Petříček, M. Dušek, and L. Palatinus. The crystallographic computing system JANA2006: General features. *Z. Kristallogr.*, 229(5):345–352, 2014.

[31] H. Bethe. Theorie der Beugung von Elektronen an Kristallen. *Annallen der Physik*, IV:55–129, 1928.

[32] J. M. Cowley and A. F. Moodie. The scattering of electrons by atoms and crystals. I. A new theoretical approach. *Acta Crystallographica*, 10:609–619, 1957.

[33] A. J. F. Metherell. Diffraction of Electrons by Perfect Crystals. In U Valdré and E. Ruedl, editors, *Electron Microscopy in Materials Science II*, pages 401–552. Commission of the European Communities, 1975.

[34] U. Pietsch, V. Holý, and T. Baumbach. *High-Resolution X-Ray Scattering from Thin Films and Lateral Nanostructures*. Springer, 175 Fifth Avenue, New York, NY 10010, USA, second edition, 2004.

[35] J. M. Cowley. *Diffraction Physics*. North-Holland, second edition, 1981.

[36] E. Prince, editor. *International Tables for Crystallography*, volume C. Kluwer Academic Publishers, P.O. Box 17, 3300 AA Dordrecht,The Netherlands, third edition, 2004.

[37] K. Fujiwara. Relativistic Dynamical Theory of Electron Diffraction. *Journal of the Physical Society of Japan*, 16:2226–2238, 1961.

[38] H. A. Ferwerda, B. J. Hoenders, and C. H. Slum. Fully relativistic treatment of electron-optical image formation based on the Dirac equation. *Optica Acta: International Journal of Optics*, 33:145–157, 1986.

[39] P. B. Hirsch, A. Howie, R. B. Nicholson, D. W. Pashley, and M. J. Whelan. *Electron Microscopy of Thin Crystals*. Butterworths, 88 Kingsway, London, W. C.2, 1965.

[40] Marc De Graef. *Introduction to Conventional Transmission Electron Microscopy*. Cambridge University Press, 1 edition, 2003.

[41] J. C. H. Spence. On the accurate measurement of structure-factor amplitudes and phases by electron diffraction. *Acta Crystallographica*, A49:231–260, 1993.

[42] Y. Ogata, K. Tsuda, and M. Tanaka. Determination of the electrostatic potential and electron density of silicon using convergent-beam electron diffraction. *Acta Crystallographica*, A64:587–597, 2008.

[43] L. Palatinus, , C. A. Corrêa, G. Steciuk, D. Jacob, P. Roussel, P. Boullay, M. Klementová, M. Gemmi, J. Kopeček, M. C. Domeneghetti, F. Camara, and V. Petříček. Structure refinement using precession electron diffraction tomography and dynamical diffraction: tests on experimental data. *Acta Crystallographica*, B71(6):740–751, 2015.

[44] L. Palatinus. PETS - program for analysis of electron diffraction data, 2011.

[45] L. Palatinus and G. Chapuis. SUPERFLIP - a computer program for the solution of crystal structures by charge flipping in arbitrary dimensions. *Journal of Applied Crystallography*, 40:786–790, 2007.

[46] W. Sinkler, C. S. Own, and L. D. Marks. Application of a 2-beam model for improving the structure factors from precession electron diffraction intensities. *Ultramicroscopy*, 107:543–550, 2007. Proceedings of the Electron Crystallography School 2005, {ELCRYST} 2005: New Frontiers in Electron Crystallography.

[47] L. J. Chen, editor. *Silicide Technology for Integrated Circuits*. The Institute of Engineering and Technology, Michael Faraday House, Six Hills Way, Stevenage, Herts, SG1 2AY, United Kingdom, 2004.

[48] C. A. Decker, R. Solanki, J. L. Freeouf, J. R. Carruthers, and D. R. Evans. Directed growth of nickel silicide nanowires. *Applied Physics Letters*, 84:1389–1391, 2004.

[49] Y. Song, A. L. Schmit, and S. Jin. Ultralong single-crystal metallic Ni_2Si nanowires with low resistivity. *Nano Letters*, 7:965–969, 2007.

[50] O. Osawa and M. Okamoto. An X-Ray analysis of the alloys of the nickel-silicon system. *Scientific Reports Tôhoku Imperial University*, 27:326, 1939.

[51] X. Fan, H. Zhang, N. Du, and D. Yang. Phase-controlled synthesis of nickel silicide nanostructures. *Materials Research Bulletin*, 47:3797–3803, 2012.

[52] Z. Zhang, P.-E. Hellström, M. Östling, and S.-L. Zhang. Electrically robust ultralong nanowires of NiSi, Ni_2Si, and $Ni_{31}Si_{12}$. *Applied Physics Letters*, 88:043104, 2006.

[53] G. Majni, M. Costato, and F. Panini. The growth processes of thin film silicides in Si/Ni planar systems. *Thin Solid Films*, 125(1–2):71–78, 1985.

[54] P. Gas, F. M. d'Heurle, F. K. LeGoues, and S. J. La Placa. Formation of intermediate phases, Ni_3Si_2 and Pt_6Si_5: Nucleation, identification, and resistivity. *Journal of Applied Physics*, 59:3458–3466, 1986.

[55] J. Kim, D. H. Shin, E.-S. Lee, and C.-S. Han. Electrical characteristics of single and doubly connected Ni silicide nanowire grown by plasma-enhanced chemical vapor deposition. *Applied Physics Letters*, 90:253103, 2007.

[56] A. H. Reader, A. H. van Ommen, P. J. W. Weijs, R. A. M. Wolters, and D. J. Oostra. Transition metal silicides in silicon technology. *Reports on Progress in Physics*, 56(11):1397–1467, 1992.

[57] N. Du, X. Fan, J. Yu, H. Zhang, and D. Yang. Ni_3Si_2-Si nanowires on Ni foam as high-performance anode of Li-ion batteries. *Electrochemistry Communications*, 13:1443–1446, 2011.

[58] N. P. Dasgupta, S. Xu, H. J. Jung, A. Iancu, R. Fasching, R. Sinclair, and F. B. Prinz. Nickel silicide nanowire arrays for anti-reflective electrodes in photovoltaics. *Advanced Functional Materials*, 22:3650–3657, 2012.

[59] K. T. Butler and J. H. Harding. A computational investigation of nickel (silicides) as potential contact layers for silicon photovoltaic cells. *Journal of Physics: Condensed Matter*, 25(39):395003, 2013.

[60] N. P. Klochko, G. S. Khrypunov, V. R. Kopach, I. I. Tyukhov, K. S. Klepikova, M. V. Kirichenko, and V. M. Lyubov. Ultrasound assisted nickel plating and silicide contact formation for vertical multi-junction solar cells. *Solar Energy*, 98:384–391, 2013.

[61] K. Toman. The structure of Ni_2Si. *Acta Crystallographica*, 5:329, 1952.

[62] G. A. Landrum, R. Hoffmann, J. Evers, and H. Boysen. The TiNiSi family of compounds: structure and bonding. *Inorganic Chemistry*, 37:5754–5763, 1998.

[63] G. Pilström. The crystal structure of Ni_3Si_2 with some notes on Ni_5Si_2. *Acta Chemica Scandinavica*, 15(4):893–902, 1961.

[64] Agilent. CrysAlis PRO, 2014. Version 1.171.37.35g.

[65] L. Palatinus and A. Van Der Lee. Symmetry determination following structure solution in $P1$. *Journal of Applied Crystallography*, 41:975–984, 2008.

[66] H. Putz and K. Brandenburg. Diamond - Crystal and Molecular Structure Visualization, 2015.

[67] T. Jansen. A brief history of aperiodic crystals: 1962-2012. In S. Schmid, R. L. Withers, and R. Lifshitz, editors, *Aperiodic Crystals*, pages 1–9, Australia, 2013. Springer.

[68] S. van Smaalen. *Incommensurate Crystallography*. Oxford University Press, Great Clarendon Street, Oxford OX2 6DP, New York, 1st edition, 2007.

[69] P. M. de Wolff. The Pseudo-Symmetry of Modulated Crystal Structures. *Acta Crystallographica Section A*, 30(6):777–785, 1974.

[70] P. M. de Wolff, T. Janssen, and A. Janner. The superspace groups for incommensurate crystal structures with a one-dimensional modulation. *Acta Crystallographica Section A*, 37(5):625–636, Sep 1981.

[71] Online IUCr Dictionary of Crystallography. Definition of superspace. http://reference.iucr.org/dictionary/Superspace. Page last modified on 13.05.2017, accessed on 24.05.2017.

[72] Online IUCr Dictionary of Crystallography. Definition of aperiodic crystal. http://reference.iucr.org/dictionary/Crystal. Page last modified on 22.05.2017, accessed on 24.05.2017.

[73] Online IUCr Dictionary of Crystallography. Definition of incommensurate modulated structure. http://reference.iucr.org/dictionary/Incommensurate_modulated_structure. Page last modified on 15.05.2017, accessed on 24.05.2017.

[74] D. Gupta. Diffusion in several materials relevant to Cu interconnection technology. *Materials Chemistry and Physics*, 41:199–205, 1995.

[75] T. Gupta. *Copper interconnect technology*. Springer, 233 Spring street, New York, NY 10013, USA, 2009.

[76] S. X. Zhang, S.-W. R. Lee, L. T. Weng, and S. Sod. Characterization of copper-to-silicon diffusion for the application of 3D packaging with through silicon vias. In *2005 6th International Conference on Electronic Packaging Technology*, pages 51–56. IEEE, 2005.

[77] M. O. Aboelfotoh and L. Krusin-Elbaum. Electrical transport in thin films of copper silicide. *Journal of Applied Physics*, 70:3382–3384, 1991.

[78] L. Stolt, F. M. D'Heurle, and J. M. E. Harper. On the formation of copper-rich copper silicides. *Thin Solid Films*, 200:147–156, 1991.

[79] R. R. Chromik, W. K. Neils, and E. J. Cotts. Thermodynamic and kinetic study of solid state reactions in the Cu-Si system. *Journal of Applied Physics*, 86:4273–4281, 1999.

[80] R. W. Olesinski and G. J. Abbaschian. The Cu-Si (Copper-Silicon) system. *Bulletin of Alloy Phase Diagrams*, 7:170–178, 1986.

[81] K. Sufryd, N. Ponweiser, P. Riani, Klaus W. Richter, and G. Cacciamani. Experimental investigation of the Cu-Si phase diagram at x(Cu)>0.72. *Intermetallics*, 19:1479–1488, 2011.

[82] H. Okamoto. Cu-Si (Copper-Silicon). *Journal of Phase Equilibria and Diffusion*, 33:415–416, 2012.

[83] W. Gierlotka and M. A. Haque. On the binary (Cu + Si) system: Thermodynamic modelling of the phase diagram and atomic mobility in face centred cubic phase. *J. Chem. Thermodynamics*, 57:32–38, 2013.

[84] B. Hallstedt, J. Gröbner, M. Hampl, and R. Schmid-Fetzer. Calorimetric measurements and assessment of the binary Cu-Si and ternary Al-Cu-Si phase diagrams. *CALPHAD: Computer Coupling of Phase Diagrams and Thermochemistry*, 53:25–38, 2016.

[85] J. K. Solberg. The crystal structure of η-Cu_3Si precipitates in Silicon. *Acta Crystallographica*, A34:684–698, 1978.

[86] C.-Y. Wen and F. Spaepen. *In situ* electron microscopy of the phases of Cu_3Si. *Phylosophical Magazine*, 87:5581–5599, 2007.

[87] N. Mattern, R. Seyrich, L. Wilde, C. Baehtz, M. Knapp, and J. Acker. Phase formation of rapidly quenched Cu-Si alloys. *Journal of Alloys and Compounds*, 429:211–215, 2007.

[88] C. A. Corrêa, O. Perez, J. Kopeček, P. Brázda, M. Klementová, and L. Palatinus. Crystal structures of η'''-$Cu_{3+x}Si$ and η''-$Cu_{3+x}Si$. *Acta Crystallographica*, In press, 2017.

[89] J. Thomas and T. Gemming. *Analytical Transmittion Electron Microscope*. Springer, 2014.

[90] F. R. Morral and A. Westgren. The crystal structure of a complex copper-silicon compound. *Arkiv foer Kemi, Mineralogi och Geologi*, B11:1–6, 1934.

[91] A. Belsky, M. Hellenbrandt, V. L. Karen, and P. Luksch. New developments in the Inorganic Crystal Structure Database (ICSD): accessibility in support of materials research and design. *Acta Crystallographica*, B58:364–369, 2002.

[92] T. Wagner and A. Schönleber. A non-mathematical introduction to the superspace description of modulated structures. *Acta Crystallographica*, B65:249–268, 2009.

[93] V. Petříček, V. Eigner, M. Dušek, and A. Čejchan. Discontinuous modulation functions and their application for analysis of modulated structures with the computing system JANA2006. *Z. Kristallogr.*, 231(5):301–312, 2016.

[94] L. Palatinus, S. J. Prathapa, and S. van Smaalen. EDMA: A computer program for topological analysis of discrete electron densities. *Journal of Applied Crystallography*, 45:575–580, 2012.

[95] C. A. Corrêa, M. Poupon, J. Kopeček, R. Král, P. Zemenová, J. Lecourt, N. Barrier, P. Brázda, M. Klementová, and L. Palatinus. Phase transitions of $Cu_{3+x}Si$ observed by temperature-dependent x-ray powder diffraction. *In press*, 2017.

[96] A. Çakir, L. Righi, F. Albertini, M. Acet, M. Farle, and S. Aktürk. Extended investigation of intermartensitic transitions in Ni-Mn-Ga magnetic shape memory alloys: A detailed phase diagram determination. *Journal of Applied Physics*, 114(18):183912, 2013.

[97] W. Miller, C. W. Smith, D. S. Mackenzie, and K. E. Evans. Negative thermal expansion: a review. *Journal of Materials Science*, 44:5441–5451, 2009.

[98] Ge. Mima and M. Hasegawa. Study of the Diagram of Cu-Si-Zn Alloy, on the Range near η Phase. *Journal of the Japan Institute of Metals and Materials*, 23:585–589, 1959.

[99] C. A. Corrêa, L. Palatinus, M. Klementová, V. Dřínek, and J. Kopeček. Crystal structure redetermination of ϵ-Ni_3Si_2 from a single nanowire by dynamical refinement of precession electron diffraction data. *Journal of Alloys and Compounds*, 672:505–509, 2016.

[100] W. Hornfeck. *Strukturchemie und Phasenbeziehungen der intermetallischen Phasen des Zweistoffsystems Iridium–Zink und ternärer Substitutionsvarianten mit Magnesium*. PhD thesis, Philipps University of Marburg, 2010.

List of Figures

List of Tables

List of Abbreviations

Abbreviation	Meaning
ADP	Atomic Displacement Parameter
ADRA	Average Distance to Reference Atom
aniso	Anisotropic
ASTRA	Program package for accurate structure analysis by the intermeasurement minimization method
calc	Calculated
CBED	Convergent-Beam Electron Diffraction
CCD	Charge-Coupled Device
CDF	Cumulative Distribution Function
CMOS	Complementary Metal-Oxide-Semiconductor
CVD	Chemical Vapor Deposition
dyn	Dynamical
ED	Electron Diffraction
EDAX	Energy dispersive Analyzer
EDMA	Electron Density Map Analysis
EDS	Energy Dispersive X-ray Spectroscopy
EDT	Electron Diffraction Tomography
exp	Experimental
HEED	High Energy Electron Diffraction
IC	Integrated Circuits
ICSD	Inorganic Crystal Structure Database
iso	Isotropic
kin	Kinematical
MDRA	Maximum Distance to Reference Atom
max	Maximum
MBFIT	Many-Beam Dynamical Calculations and Least-squares Fitting
min	Minimum
MSLS	Multislice Least-Squares
NW	Nanowire
obs	Observed

Abbreviation	Meaning
PED	Precession Electron Diffraction
PEDT	Precession Electron Diffraction Tomography
PETS	Process Electron Tilt Series
PXRD	Powder X-ray Diffraction
RATS	Record Automated Tilt Series
RED	Rotation Electron Diffraction
SCXRD	Single Crystal X-ray Diffraction
SDD	Silicon Drift Detector
STEM	Scanning Transmission Electron Microscope
TD-PEDT	Temperature-Dependent Precession Electron Diffraction Tomography
TD-PXRD	Temperature-Dependent Powder X-ray Diffraction
TD-SCXRD	Temperature-Dependent Single Crystal X-ray Diffraction
TEM	Transmission Electron Microscope